IMPROVEMENT OF FINITE ELEMENT MODEL BY USING SINE VIBRATION TEST RESULTS OF A COMMUNICATION SATELLITE

A THESIS SUBMITTED TO
THE GRADUATE SCHOOL OF NATURAL AND APPLIED SCIENCES
OF
MIDDLE EAST TECHNICAL UNIVERSITY

BY

ABDULKADİR ÇEKİÇ

IN PARTIAL FULFILLMENT OF THE REQUIREMENTS
FOR
THE DEGREE OF MASTER OF SCIENCE
IN
AEROSPACE ENGINEERING

FEBRUARY 2021

Approval of the thesis:

IMPROVEMENT OF FINITE ELEMENT MODEL BY USING SINE VIBRATION TEST RESULTS OF A COMMUNICATION SATELLITE

submitted by **ABDULKADİR ÇEKİÇ** in partial fulfillment of the requirements for the degree of **Master of Science** i**n Aerospace Engineering, Middle East Technical University** by,

Prof. Dr. Halil Kalıpçılar
Dean, Graduate School of **Natural and Applied Sciences** _____

Prof. Dr. İsmail H. Tuncer
Head of the Department, **Aerospace Engineering** _____

Prof. Dr. Yavuz Yaman
Supervisor, **Aerospace Engineering Dept., METU** _____

Examining Committee Members:

Prof. Dr. Serkan Özgen
Aerospace Engineering Dept., METU _____

Prof. Dr. Yavuz Yaman
Aerospace Engineering Dept., METU _____

Prof. Dr. Altan Kayran
Aerospace Engineering Dept., METU _____

Assoc. Prof. Dr. Ercan Gürses
Aerospace Engineering Dept., METU _____

Prof. Dr. Metin Uymaz Salamcı
Mechanical Engineering Dept., Gazi Uni. _____

Date: 15.02.2021

I hereby declare that all information in this document has been obtained and presented in accordance with academic rules and ethical conduct. I also declare that, as required by these rules and conduct, I have fully cited and referenced all material and results that are not original to this work.

Name, Last name : Abdulkadir Çekiç

Signature :

ABSTRACT

IMPROVEMENT OF FINITE ELEMENT MODEL BY USING SINE VIBRATION TEST RESULTS OF A COMMUNICATION SATELLITE

Çekiç, Abdulkadir
Master of Science, Aerospace Engineering
Supervisor : Prof. Dr. Yavuz Yaman

February 2021, 129 pages

In this thesis, the vibration analysis of a communication satellite is performed, and the improvement of the finite element model by using vibration test results is presented. First, the satellite finite element model is generated using MSC/PATRAN and MSC/NASTRAN commercial software. With the natural frequency and frequency response analysis, the expected frequency values and response amplitudes in accelerometers are calculated in vibration tests. The results obtained in the vibration test are compared with the analysis results using the HYPERGRAPH commercial software and their similarity with the modal assurance criteria calculation, which is developed using the FORTRAN programming language. The frequency values converged to the measured values as a result of the finite element model improvement, which is performed using error sensitivity assessment at the relevant frequencies.

Keywords: Communication Satellites, Finite Element Method, Vibration Analysis, Finite Element Model Improvement, Vibration Test

ÖZ

BİR İLETİŞİM UYDUSUNDA TİTREŞİM TEST SONUÇLARI KULLANILARAK SONLU ELEMANLAR MODELİNİN İYİLEŞTİRİLMESİ

Çekiç, Abdulkadir
Yüksek Lisans, Havacılık ve Uzay Mühendisliği
Tez Yöneticisi: Prof. Dr. Yavuz Yaman

Şubat 2021, 129 sayfa

Bu tezde bir iletişim uydusunun titreşim analizleri gerçekleştirilip, titreşim test sonuçları kullanılarak sonlu elemanlar modelinin iyileştirilmesi sunulmaktadır. İlk olarak uydunun sonlu elemanlar modeli MSC/PATRAN ve MSC/NASTRAN ticari yazılımları kullanılarak modellenmiştir. Yapılan doğal frekans ve frekans tepke analizleri ile titreşim testinde ivmeölçerlerde beklenen frekans değerleri ve tepke genlikleri hesaplanmıştır. Titreşim testinde elde edilen sonuçlar analiz sonuçlarıyla HYPERGRAPH ticari yazılımı kullanılarak karşılaştırılmış ve FORTRAN programlama dili kullanılarak geliştirilen şekil güvence kriteri hesabı ile benzeşimlerine bakılmıştır. İlgili frekanslarda hata duyarlılık değerlendirmesi kullanılarak gerçekleştirilen sonlu elemanlar iyileştirilmesi sonucu frekans değerleri ölçülen değerlere yakınsamıştır.

Anahtar Kelimeler: İletişim Uyduları, Sonlu Elemanlar Metodu, Titreşim Analizi, Sonlu Elemanlar Modeli İyileştirilmesi, Titreşim Testi

To my son Çınar Kuzey

ACKNOWLEDGMENTS

I would like to express my gratitude to my supervisor Prof. Dr. Yavuz Yaman, for his guidance and support.

I also would like to thank my parents for their loving supports.

I would like to express my appreciation to my supervisors in the Space System Department of Turkish Aerospace for providing the necessary data and support.

I am very grateful to my colleagues Bilal Burak Doğan, Özgun Çokgezen, Duygu Ceylan, and Halil Güç for giving me encouragement and strength to complete this study. Many thanks to my dear friend Onur Çakmakçı for his technical and morale supports.

The last but not the least, I would like to thank my wife, Özgül Filik Çekiç, for her endless support, encouragement and love.

TABLE OF CONTENTS

LIST OF TABLES

TABLES

LIST OF FIGURES

FIGURES

LIST OF SYMBOLS

SYMBOLS

D_R	Rigid Body Vector
K	Stiffness Matrix
M	Mass Matrix
P	Participation Factor
$\boldsymbol{u}$	Displacement
$\ddot{\boldsymbol{u}}$	Acceleration
u_e	Element Displacement
Π^e	Elastic Energy
Π^k	Kinetic Energy
$\boldsymbol{\Phi}$	Eigenvector
$\boldsymbol{\psi}$	Modal Vector
ω	Natural Frequency
a	Analysis
c	Modal Coefficient for Reference
t,m	Test
r,h	Mode Number
q	Degree of Freedom

Dummy variables confined to certain chapters are clearly defined wherever applicable.

CHAPTER 1

INTRODUCTION

1.1 Objective of the Study

Satellites are exposed to severe mechanical environments during launch and orbit maneuvers in their service time. Consideration of these loads in satellite structure design and analysis is one of the main requirements of satellite development. The most crucial mechanical load which is considered in design is the sine vibration load caused by launch. Before the launch campaign, satellite structure verification is necessary by performing sine vibration tests.

Communication satellites are classified as large and heavy spacecraft. One of the challenging tasks in satellite structure design is to obtain an optimized and lighter structure that can withstand mechanical loads in its service life like any other air vehicle. This will cause an economically advanced and effective launch, considering the orbit transfer of the satellite. This can be achieved by increasing confidence in finite element analysis by using sine vibration test data.

In this thesis, the indigenous Finite Element Model of the communication satellite is constructed and verified. Then the sine vibration tests of the actual satellite structure are conducted. The numerical (FEM) and the experimental frequency responses of the satellite are compared, and the mode pairings are also completed by using the modal assurance criteria. In order to obtain the similarity between the sine vibration test results and the numerical analysis results, the possible regions of the errors in which the numerical and the experimental values differ are identified. This study aims to improve the Finite Element Model of the satellite by assuming that the sine vibration experiments are properly conducted and the results of the experiments are correct. While doing this, it is also assumed that the material characteristics and

especially the actual stiffness values of some parts of the satellite may contain some variations from the theoretically assigned values in the Finite Element Model. Hence, the dimensions of the components are not changed, but their stiffness values are varied for comparison with the Finite Element Model results. As a result, the design parameters are defined, and sensitivity analyses are performed in order to evaluate each modification's effect. The comparisons are presented.

1.2 Methodology

In the thesis, the general methodology of the study is given in this section.

After completing the general literature review, the thesis study starts with a general design description of the communication satellite and the finite element model description. In order to obtain accurate FEM, the structure subsystem of the satellite should be interpreted well. With the element size convergence study's help, the correct element size of the FEM is chosen for dynamic analysis, and the model is generated. Prior to conduct further analysis by using the FEM, model checks are completed.

The sine vibration analysis is performed, and only x-direction results are investigated in this study. Accelerometer locations, the accelerometers' response, and transfer functions of the accelerometers are given in the thesis. It is assumed that the test is performed properly and the results are accurate also.

Additionally, the effective mass values of the satellite are also computed. With the help of the effective masses, the frequency range that is relevant is correctly specified.

Then the computational results are compared with the experimentally obtained results basically in terms of the frequency values. Possible error localization of the FEM is completed by using the strain energies at each resonance frequencies, and the regions for modifications in the finite element model are specified.

In this study, the trial and error approach is taken into consideration in order to improve the FEM of the satellite. Although no formal optimization methodology is attempted; in terms of the formal optimization terminology, the objective function is to minimize the frequency difference between the sine vibration test resonance frequencies and the computational analysis natural frequencies by using the correlation requirements given and specified in the European Space Standardization mechanical handbook.

The effects of the accelerometer locations on the satellite and the masses of the accelerometers are not included in the FEM. Furthermore, the damping characteristics are not also included in the computational studies. Hence the comparisons and any possible improvements on the response levels are not considered in the current study.

The general methodology of the thesis is also given in Figure 1.1.

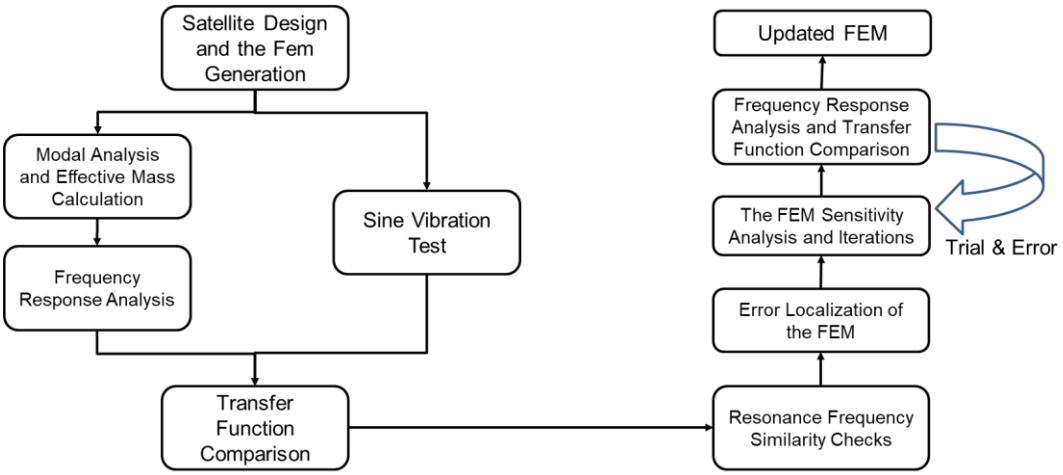

Figure 1.1. General Methodology of the Study

1.3 Layout of Thesis

In Chapter 1, the thesis topic is explained briefly. The layout and limitations of the thesis are given in this chapter.

In Chapter 2, a literature review of the thesis topic is introduced. The history of satellites and satellite types is clarified. Besides, communication satellites are elaborated further. Mechanical environments caused by launchers, which are very crucial for satellite design, are briefly introduced. The design and test of satellites are mentioned, and also the correlation of the vibration test is explained.

Chapter 3 addresses the general structural architecture of the communication satellite. Detailed information on the finite element model, material properties, and model checks are given in this chapter.

Chapter 4 demonstrates the sine vibration test results, including base excitation and the response of accelerometers. Sine vibration test of the satellite is mentioned, and information about shaker, accelerometer locations, types are given.

Chapter 5 explains the methodology of eigenvalue and frequency response analysis. Effective mass calculations, mode shapes of the satellite, and frequency response calculations of accelerometers on satellites are given.

Chapter 6 demonstrates the comparison of the transfer functions between the sine vibration test and frequency response analysis. Error localization studies and modal assurance criteria calculations are explained. The finite element modal improvements with several iterations and the results of these studies are shown.

In Chapter 7, the general conclusions are drawn, and the outcomes of the thesis are presented.

1.4 Limitations of the Thesis

The limitations of the thesis are listed below.

- Only the first four frequencies of the communication satellite, which have the highest effective mass in the x-direction, are considered.
- Only x-direction of the sine vibration test results is used for the finite element model improvement.
- The trial & error approach is used in order to improve the FEM of the satellite. No formal optimization method is attempted.
- The computational model is constructed as the undamped one. Therefore, no response level comparisons and improvements are attempted.

CHAPTER 2

LITERATURE REVIEW

2.1 Introduction

From the past to the present, many technological developments have occurred in the space industry. The space industry, which started to develop in the 20th century, enabled the infrastructure of many technologies that society uses in daily life today. Communication is one of these technologies, and communication satellites operate in space to provide this opportunity.

Satellites are subjected to many functional and structural tests from design to launch. Sine vibration, acoustic, and shock tests are the mechanical tests that satellites shall undergo before launch campaigns. The most important of these tests are the sine vibration tests. Verification and improvement of the structural design are directly related to the correlation between test results and calculations. Due to the increasing competition in the space industry today, it has become even more crucial to design the lightest and most effective satellite structure. A light satellite that achieves the requirements of the launcher means having a more beneficial transfer orbit and more payload. Besides, since the satellite launch cost is significantly reduced, the satellite service life in orbit increases.

Consequently, the correlation between the sine vibration test results and the finite element model is significant for designing lighter and more efficient products in satellite projects. Many methods have been developed to compare test and analysis results and to improve the finite element model.

In this chapter, the history of spacecraft and satellite types will be explained. Mechanically harsh environments caused by the launcher and mechanical tests will

be mentioned. In addition to those, literature about test and analysis comparison methods will be given in this chapter.

2.2 History of Spacecraft

In the 20th century, with the development in the aerospace area, rockets became powerful enough to reach space and initiated a new era for space exploration.

With the start of World War-2, rocket science was actively used as a long-range weapon. In the 1930s and 1940s, Germany developed V-2 missiles, which were the origin of today's launch vehicles. After World War 2, countries such as the United States and the Soviet Union developed their own rocket technology.

With the development of launch vehicles, the Soviet Union launched the world's first artificial satellite Sputnik 1, in 1957, shown in Figure 2.1. Sputnik was launched into low earth orbit. It has a sphere structure with a 58cm diameter, and its mass is 83.4kg. There are external radio antennas to broadcast radio signals to Earth, which is 2.4-2.9m long [1]

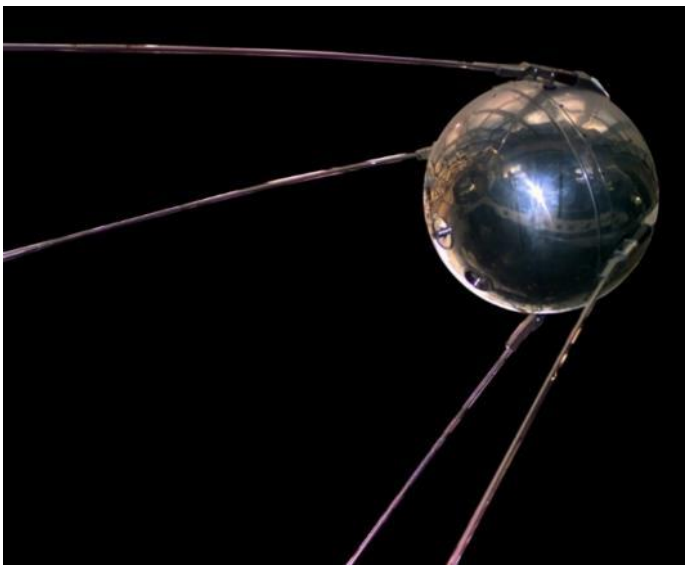

Figure 2.1. Sputnik -1 Satellite[1]

Since Sputnik 1, more than 9000 satellites have been launched with different mission purposes.

2.3 Types of Satellites

Satellites can be categorized with respect to the mission objective, maximum mass, and operating orbit, according to [2]. The first one, the mission objective base, can be divided into four sub-categories.

1. Technology Demonstration
2. Space Science
3. Earth Science
4. Earth Observation

NASA's laser communications relay demonstration (LCRD) is an excellent example of a technology demonstration shown in Figure 2.2 [3]. This mission uses a laser instead of a radio to communicate faster than 10 to 100 times. Additionally, this technology requires less mass and power on the satellite, which is very crucial. This technology will enable faster communication between Earth and Space in future missions such as the MARS mission.

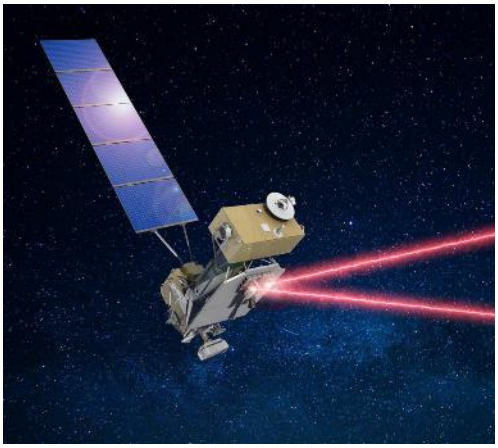

Figure 2.2. Example Technology Demonstration Satellite for LCRD [3]

Another mission type is space science missions. Space Science missions are used for deep space studies. Figure 2.3 shows the Rosetta spacecraft built by the European Space Agency [4]. Rosetta performed scientific exploration for the study of a comet by landing on it. It was launched in 2004, and its mission was completed in 2016 successfully. Its launch mass is 2900kg.

Figure 2.3. Example of Scientific Satellite: Rosetta [4]

Earth science missions help scientists to understand Earth's systems from the global to micro-scale processing by using satellites [5]. Additional to earth observation points, using satellite observation, these researches collect data about Earth's atmosphere, ocean, and land. One of the Earth science mission satellites is CYGNSS, which is shown in Figure 2.4. The Cyclone Global Navigation Satellite mission is a mission by NASA to establish research between the sea and air near the storms to improve weather predictions on tropical storm regions. These satellites are constellation satellites, having eight simultaneous satellites on orbit.

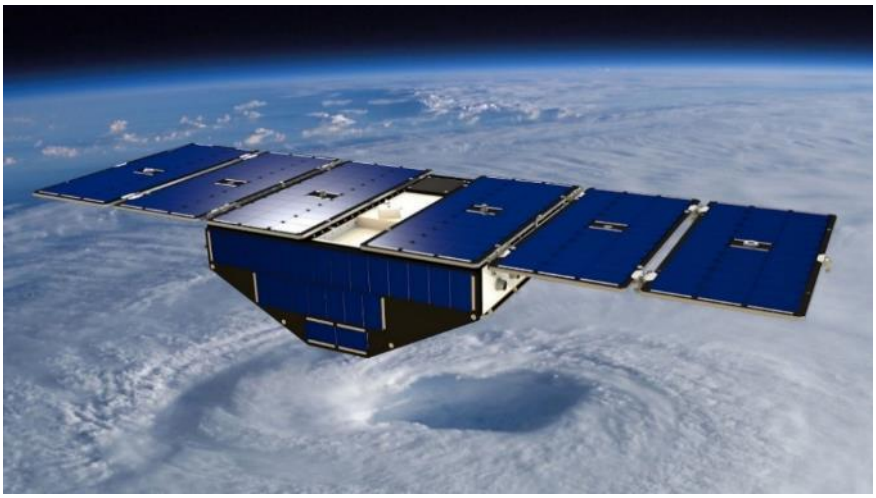

Figure 2.4. Example of Earth Science Satellite CYGNSS

Weather monitoring satellites are examples of earth observation missions, and one of these satellites is Sentinel-4, which is shown in Figure 2.5 [6]. This satellite is one of the constellation satellites, and the aim of the mission is to monitor Earth's atmosphere. Sentinel-4's launch mass is 3600kg, and its launch date is planned as 2021.

Figure 2.5. Example of Earth Observatory Satellite SENTINEL-4 [6]

The second criterion is the mass of the spacecraft. With respect to the mass of the spacecraft, there can be three types of spacecraft.

1. Large Spacecraft
2. Medium Spacecraft
3. Small Spacecraft

Large spacecraft is larger than 1000kg, and medium spacecraft's mass is between 500kg and 1000kg with propellant. Having a mass of less than 500kg, spacecraft can be categorized as small spacecraft.

The last criterion is the orbital regime, and it can be sub-categorized into three orbits.

1. Low Earth Orbit
2. Mid Earth orbit
3. High Earth & Geosynchronous orbit

These different orbits provide a different field of view of satellites depending on mission types and performance. Low earth orbit is up to 2000km altitude.

A high elliptical orbit is between 2000km and 35780km up from the earth's surface, while a geosynchronous orbit is more than 35780km altitude. With different orbits, satellites perform their missions with a constant field of view or changing. In Figure 2.6, Earth orbits are shown.

Figure 2.6. Demonstration of Earth Orbits [7]

Weather satellites and communication satellites are located in High Earth Orbit (HEO), while navigation satellites are in mid earth orbit. Earth-observing satellites and most scientific satellites are in low earth orbit.

For instance, the Göktürk-1 is an earth observation satellite, and it provides high-resolution earth images, and its orbit is low earth orbit [8]. Gökturk-1 launch mass is 1070kg, and It was launched in 2016 on the Vega launch vehicle, which is shown in Figure 2.7.

Figure 2.7. Example of Low Earth Orbit Satellite Göktürk-1 [8]

One of the mid-earth orbit satellites examples is a navigation satellite. In Figure 2.8, the Galileo satellite is shown, which is Europe's navigation satellite system that provides positioning and timing on the Earth's surface with high accuracy [9]. With around 700kg mass and more than 12 years of design life, the last Galileo satellites were put in orbit in July 2018.

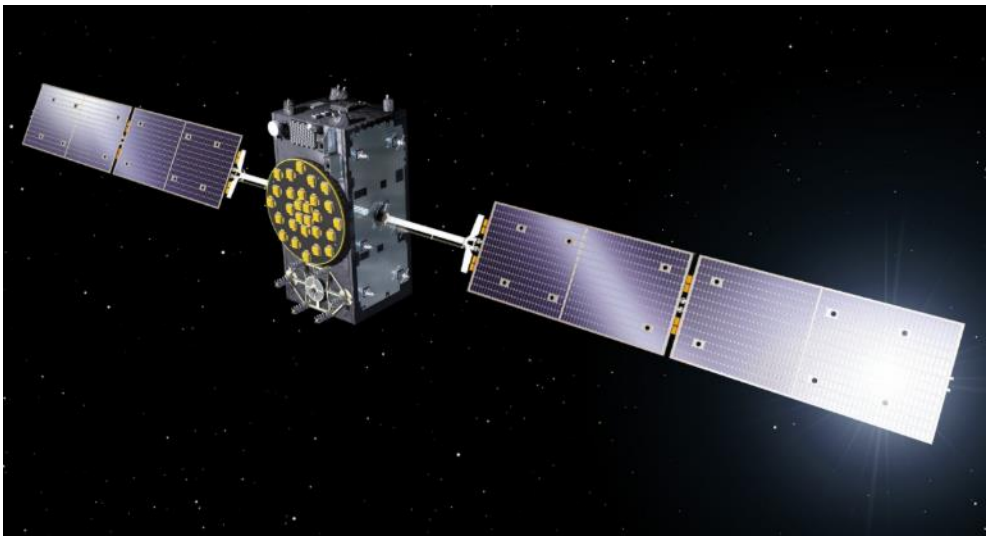

Figure 2.8. Example of Mid Earth Orbit Satellite Galileo [9]

Turksat-6A is Turkey's first communication satellite that was developed and manufactured with domestic capabilities[10], which is shown in Figure 2.9. The satellite is planned to be placed in geosynchronous orbit in 2023. It is more than 4000kg with ten Ku-band transponders. Its service life is expected to be more than 15 years.

Figure 2.9. Example of Geosynchronous Orbit Satellite Turksat-6A [10]

2.4 Launchers and Mechanical Environments

A launcher is a vehicle that is designed to carry a payload from Earth's surface to space. Launch vehicles can be classified with a different mission. However, the primary concern of launcher vehicles is the allowable payload mass and orbit ejection location.

For instance, the Soyuz launch vehicle is one of the first developed launchers. The Soyuz launch vehicle family launched the first artificial satellite, the Sputnik-1 (1957), and the first man Yuri Gagarin (1961). It had more than 1780 launches up to 2011. It has the capability of low earth orbit and geo transfer orbit ejection.

According to [11], the most severe design cases for satellite structures occur during the launch stage. The launchers depending on their target orbital missions have a different number of stages. The Soyuz launch vehicle has three stages, which are shown in Figure 2.10 [12]. During these stages, there are many sources of mechanical loads specified in every similar launcher, such as quasi-static acceleration, sine vibration (low frequency), acoustic vibration, and shock. Some of these loads can be predicted statistically or as a function of time. These mechanical environments are defined at the interface of launch vehicles and spacecraft for design purposes.

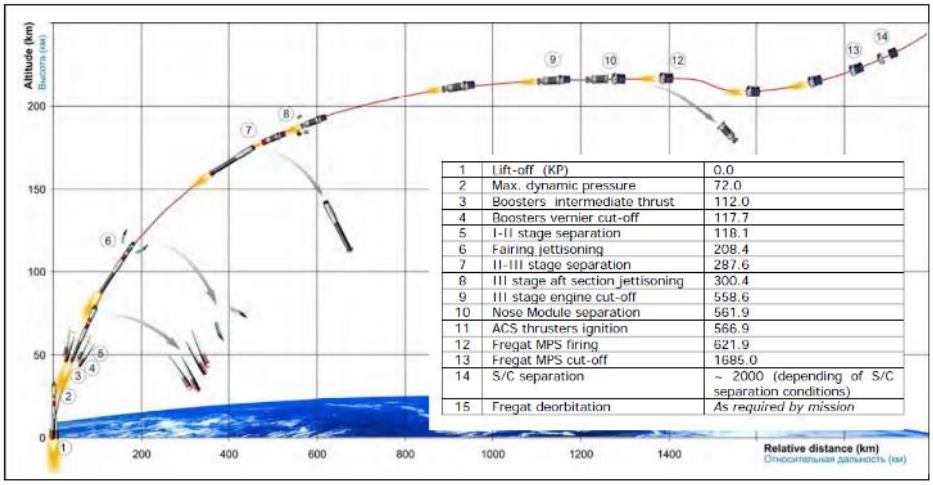

Figure 2.10. Typical Ascent Profile [12]

According to the ECSS handbook[13], the launch vehicle and spacecraft system are excited by various sources. In these excitations, launch vehicle engines are the main drivers. These excitations are transmitted to spacecraft with two different load paths:

- Structural transmission with the help of launcher structure, which spacecraft is excited at its interface.
- Acoustic transmission via the ambient air where the spacecraft is excited by the acoustic pressure inside the payload fairing and acting on all exposed structures.

In Table 2.1, different launch events and sources of vibrations are shown.

Table 2.1. Sources of Launch Vehicle Environments

	Acoustic	**Random Vibration**	**Sine Vibration**	**Shock**
Lift-off	X	X		
Aerodynamic/Buffet	X	X		
Separation (stage, fairing, spacecraft)				X
Motor Burn/ Combustion/ Propulsion Generated Oscillation (POGO)		X	X	

One of these excitations is quasi-static accelerations. Quasi-static acceleration is defined in both axial and lateral directions. The launch vehicle's thrust is the primary driver of axial accelerations, and it increases at every stage of launch while the mass of propellant decreases over time. Maximum axial acceleration occurs at the end of stages, which are shown in Figure 2.11. For instance, the Soyuz launch vehicle reaches maximum axial acceleration at the end of every stage and drops significantly after these stages. Lateral quasi-static accelerations are the results of lateral thrust components and angle of attack of launch vehicles during launch. These accelerations are superimposed with transient loads, and combined quasi-static loads are generated, which is specified in Table 2.2.

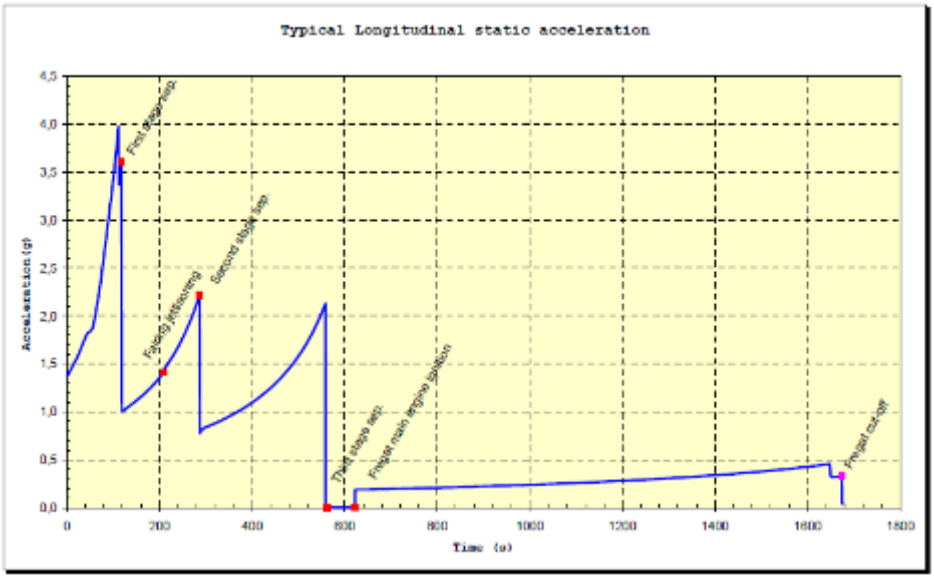

Figure 2.11. Typical Longitudinal Static Acceleration [12]

Table 2.2. Quasi-static loads of the Soyuz Launcher at Different Stages[12]

Load Event	Quasi-Static Loads (g)					
	Lateral			Longitudinal		
	Static	Dynamic	Total	Static	Dynamic	Total
Ground Transportation	-	± 0.3	± 0.3	-1.0	± 0.3	min -1.3 max -0.7
Lift-off	± 0.2	± 1.6	± 1.8	-1.0	± 0.6	min -1.6 max -0.4
Flight with maximum dynamic pressure (Qmax)	± 0.4	± 0.7	± 1.1	-2.4	± 0.4	min -2.8 max -2.0
First-Stage flight with maximal acceleration	± 0.1	± 0.8	± 0.9	-4.3	± 0.7	min -5.0 max -3.6
Separation between first and second stages	± 0.2	± 0.9	± 1.1	-4.1 -1.0	± 0.2 ± 0.4	min -4.3 max -0.6
Second-stage flight	± 0.1	± 1.1	± 1.2	-4.1 -1.0	± 0.4 ± 1.4	min -4.0 max -0.6
Separation between second and third stages	± 0.2	± 0.6	± 0.8	-4.1 -1.0	± 0.7 ± 1.5	min -3.3 max +1.3
Beginning of third-stage flight	± 0.2	± 0.6	± 0.8	-1.0	± 1.9	min -2.9 max +0.9
Third-stage engine cutoff	± 0.1	± 0.3	± 0.4	-4.1 -0.0	0.0 ±1.8	min -4.0 max +1.8

The sinusoidal excitation component is defined as the low-frequency vibration faced during launch, which is caused by engine thrust, engine-structure coupling, and attitude control limit cycle [11]. For instance, propulsion generated oscillations of Ariane 1 launch vehicle first flight at the end of the second stage is shown in Figure 2.12. This excitation is generated due to interaction between the structure, the hydraulics, and the propulsion[13]. Sinusoidal excitations are generally defined between 5-100Hz at the interface of spacecraft and launch vehicle interface. Ariane-5 equivalent sinusoidal excitation is specified in Table 2.3.

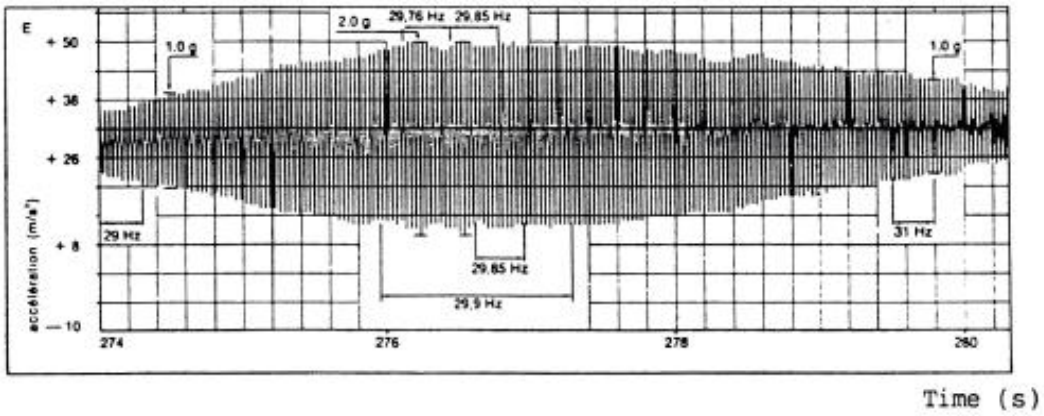

Figure 2.12. Ariane-1 First Flight- LV/SC Interface Acceleration [13]

Table 2.3. Limit Sine Vibration of the Ariane Launcher[14]

Direction	**Frequency Band (Hz)**	**Sine Amplitude (g)**
Longitudinal	2 - 50	1.0
	50 - 100	0.8
Lateral	2 - 25	0.8
	25 - 100	0.6

Higher frequency components during launch are considered as acoustic or random vibration environments. Acoustic excitation of air in the fairing and the excitation of structure cause a high-frequency random vibration environment on the spacecraft, which is emitted from exhaust jet and aerodynamic turbulence. These acoustic

environments are defined for every launch vehicle for spacecraft design purposes. In Figure 2.13, the limit acoustic environment of the Ariane-5 launcher is demonstrated.

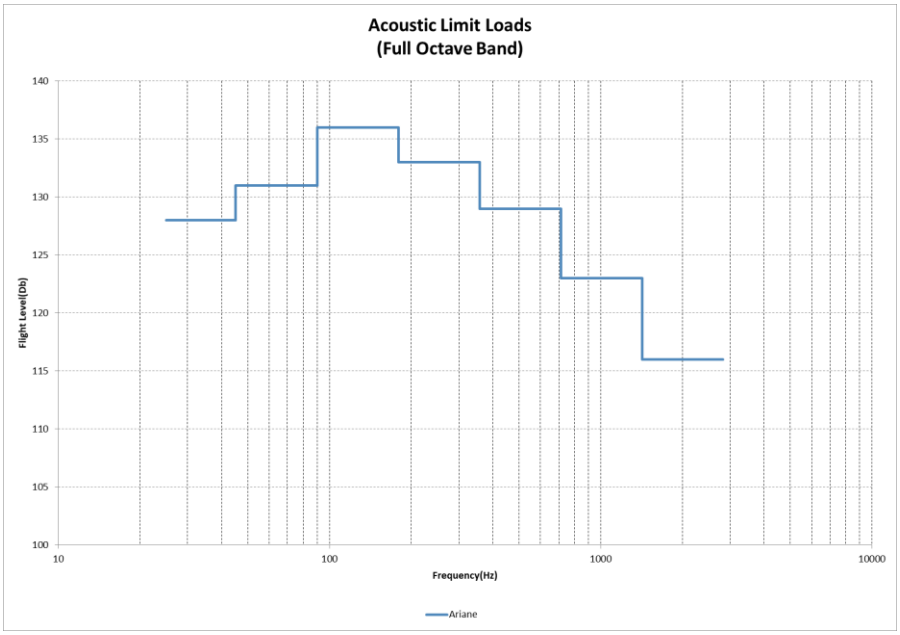

Figure 2.13. Limit Acoustic Environment [14]

During Launcher stage separation, jettison, and spacecraft separation, a transient regime occurs in the launcher structure. The primary source of these excitations is the pyro shocks. The shock environment is another essential excitation that should be considered in the satellite structure design. The shock environments are generated in Figure 2.14 as shock load spectra of the Ariane-5 vehicles.

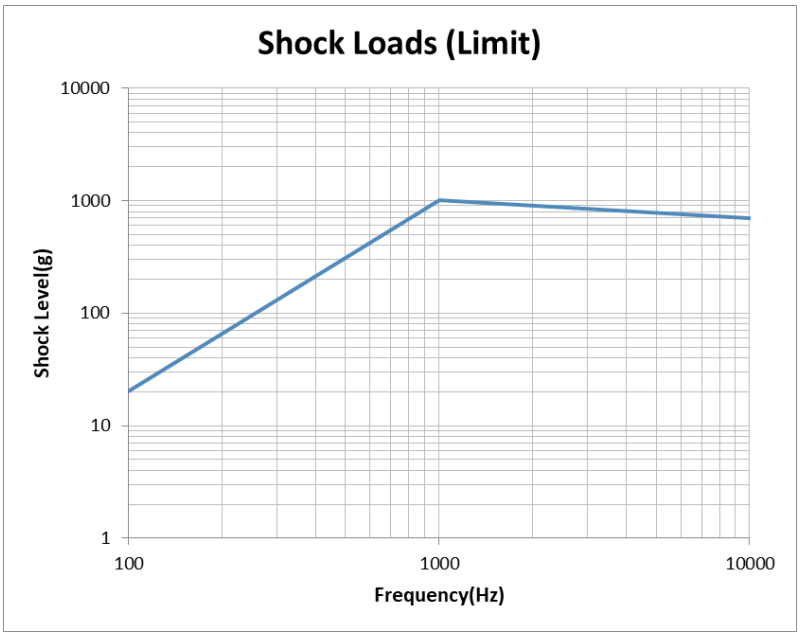

Figure 2.14. Shock Load Spectra During Spacecraft Separation [14]

2.5 Design and Mechanical Test of the Communication Satellites

A communication satellite is one type of satellite that enables communications on Earth. It amplifies radio signals using transponders, and it creates a connection from a source to different locations on Earth. Communication satellites are used for radio, television, communication, and the internet. These satellites generally operate in geostationary orbit. The first geostationary communication satellite is Syncom 3, and it was launched in 1964, which is shown in Figure 2.15.

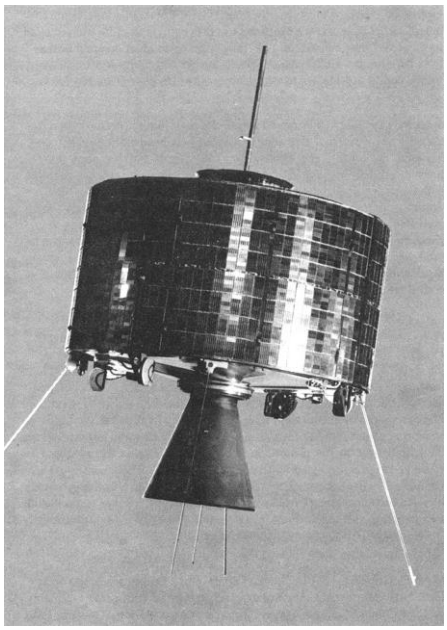

Figure 2.15. The First Geostationary Communication Satellite Syncom 3[15]

Satellites have a group of components that enable the satellite to achieve its mission successfully, and these components are called subsystems. A typical communication satellite consists of the following subsystems[16]:

- Attitude and Orbit Control Subsystem determines and controls the satellite's orbital position and altitude by using sensors.
- Propulsion Subsystem uses thrusters to change spacecraft's position and altitude. The propulsion subsystem generates its thrust by using chemicals or electrical systems.
- Communication Subsystem enables communication of Satellite with Earth. Especially in the communication satellites, there are transponders, which are a series of interconnected units. This subsystem transfers the received signals to specific areas on Earth by using feeders and reflectors.
- Command and Data Handling Subsystem process command from Earth and enables other subsystems to communicate with each other.

- The Electrical Power Subsystem generates, stores, and distributes electrical power, which satellites require to operate successfully. Generally, solar arrays generate the power that the subsystem requires.
- The Thermal Control subsystem keeps equipment temperatures within their acceptable levels by using thermal control components such as multi-layer insulations and heat pipes.
- Structure and Mechanism Subsystem supports all subsystems physically and keeps satellite unity during launch and its mission. It provides stiffness, positional stability, and strength.

Figure 2.16 shows the payload module, propulsion module, and platform module of an SGEO satellite.

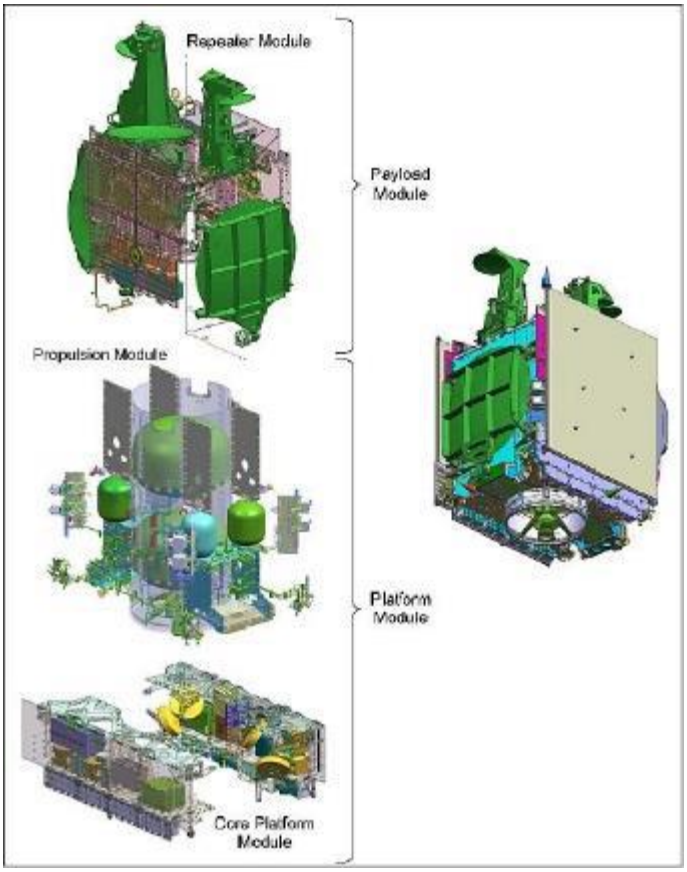

Figure 2.16. Example Modules of SGEO Satellite of ESA[17]

The structure and mechanism subsystem's main aim is to achieve minimum mass and maximum reliability requirements, resulting in minimum cost and schedule. The structure subsystem has close interaction with other subsystems, enabling it to understand other subsystems' requirements and provide efficient design.

The structure subsystem can be divided into three major components [16].

- The primary structure is the main load-carrying member of the satellite between components and the launch vehicle. It is usually designed for stiffness, mainly for the first bending mode of satellites. In addition, it withstands quasi-static accelerations and transient loading during launch.
- The secondary structures include support beams, reflectors, solar arrays, and propulsion tanks. In addition to primary structure loads, thermal loads in orbit and acoustic loads that are faced during launch are critical for secondary structures.
- The tertiary structures refer to the smallest structures, such as harness brackets and electronic box supports. High-frequency driven loads are most critical to tertiary structures. Also, stiffness, which is critical for dynamic coupling, and positional stability are other requirements for tertiary structures.

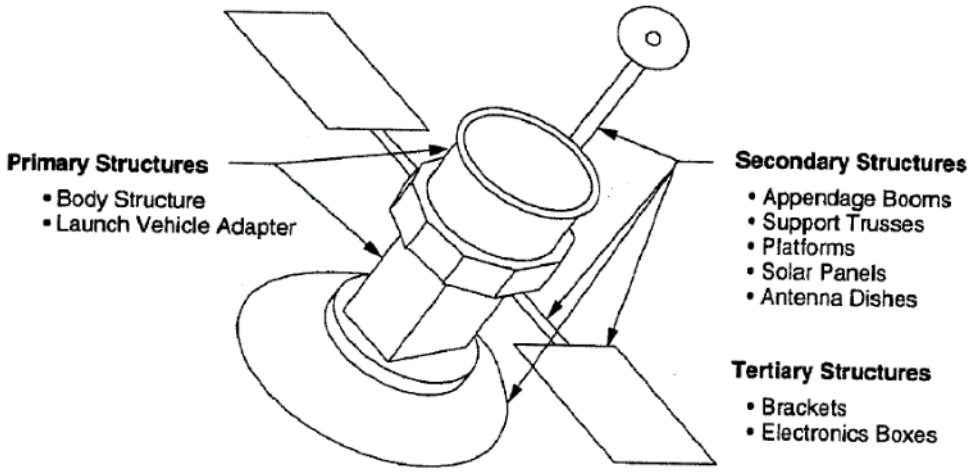

Figure 2.17. Categories of Structure [16]

Structural design starts with conceptual configuration design, material selection, and manufacturing method selection [18]. It continues with analysis-design iterations, and it completes with verification of structures with mechanical tests.

Qualification of the Satellite is another crucial milestone of satellite development upon completion of the design. According to [18], the following mechanical tests are generally performed.

- The static test is performed on the structure by applying quasi-static loads, which the structure will face during launch. The static test's aim is mainly to qualify the strength of primary structure and structure interfaces.
- The modal survey test aims to determine the satellite's modal characteristic by exciting structure with small exciters. With this test, natural frequencies, mode shapes, and damping of the satellites are determined.
- The Sine vibration test objective is to support the verification of the satellite mathematical model used to calculate the forced frequency response of satellite and show that satellite can withstand vibration environment during launch. The satellite is excited as a sweep of frequency from 5Hz to 100Hz. It is essential to assess the amplification of the excitation on the satellite's critical equipment and the interface of the satellite with the launcher.
- Random vibration test supports the verification of spacecraft units under random vibration environments experienced during launch.
- Shock test is the verification and qualification of satellite structure due to pyro shocks caused by interface clamp band, solar panels, and antenna hold and release mechanisms.
- The acoustic test is the demonstration of spacecraft structure strength against acoustic environments. Typically, a spectrum from 30Hz to 8000Hz is applied to the satellite.

One of the most crucial mechanical tests for spacecraft is the sine vibration tests. Sine vibration tests are performed on single-axis dynamic shakers, and the satellite is excited in three directions separately. The demonstration of a satellite on a

dynamic shaker is shown in Figure 2.18. The sine vibration testing profile is given explicitly in launch vehicle user manuals, and it generally covers from 5Hz to 100Hz. According to [13], the objective of the sine vibrations tests can be summarized as follows:

- To characterize the satellite's dynamic behavior to validate a mathematical model used for coupled load analysis with the launch vehicle,
- To show the satellite structure can withstand launcher sine vibration environment without any failure or structural degradation,
- To demonstrate there is not any over-loading on equipment in terms of acceleration,
- To detect workmanship errors.

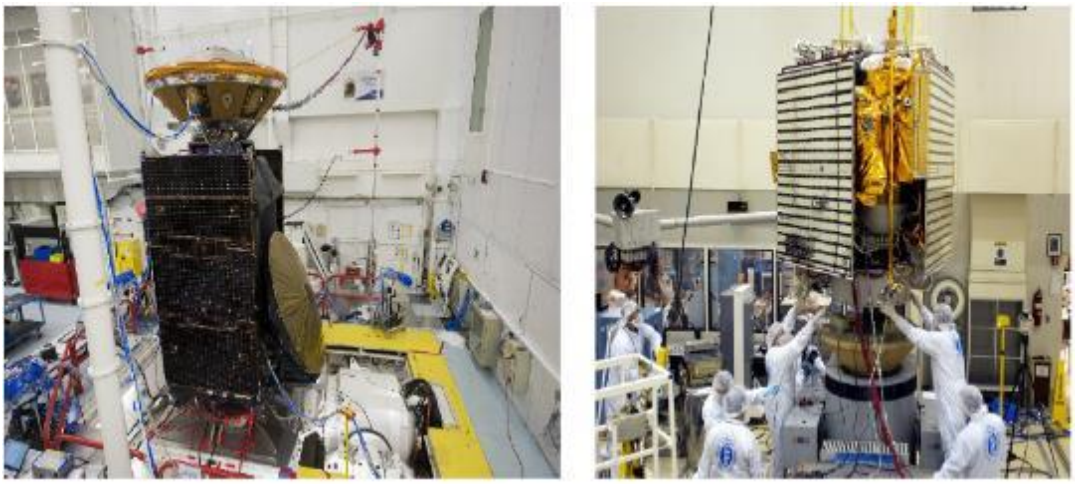

Figure 2.18. Demonstration of Satellites on Shaker at Sine Vibration Tests

In order to measure the accelerations on structure, accelerometers have to be implemented. These accelerometers are attached to the satellite's critical components such as reflectors, solar arrays, towers, and primary structure to ensure not to over-test these components. The sine vibration tests start with very low-level excitations and gradually increase excitation level for each test starting from 1/4, 2/4, 3/4, and

full level of base excitation [19]. At the end of the sine vibration test, an additional low-level test is performed to compare results with the first low-level test. These low-level runs aim to control the transfer functions of accelerometers before and after the test to check structural integrity. The diagram of the sine vibration test management process is given in Figure 2.19.

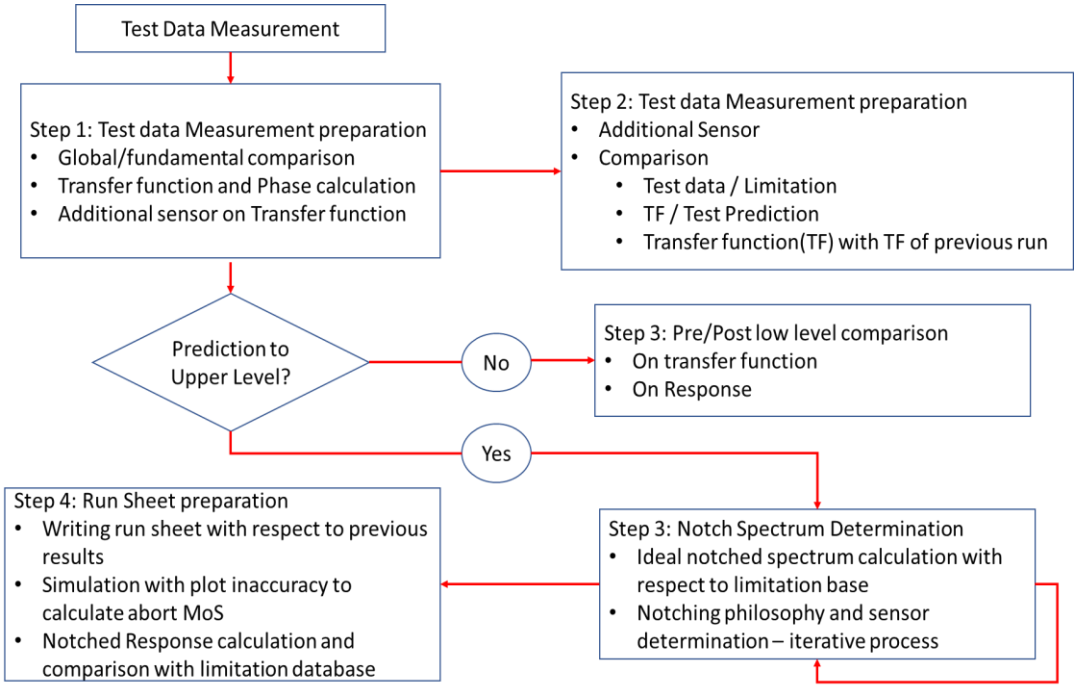

Figure 2.19. Sine Vibration Test Management Process Overview[13]

Performing a low-level test at the beginning of sine vibration is very crucial. This will show the functionality of sensors and the preliminary calculation of the transfer functions. Before increasing excitation levels, the satellite interface's primary notch level is estimated by extrapolating transfer functions of low-level sine vibration tests. The main objective of notching is to reduce excitation level during the sine vibration tests at resonance, not to exceed the sizing loads at the interface. By the estimation of notching and response of accelerometers for the next levels, the risk of over test

of satellite and equipment is minimized. In Figure 2.20, the base excitation of satellite with notching is demonstrated.

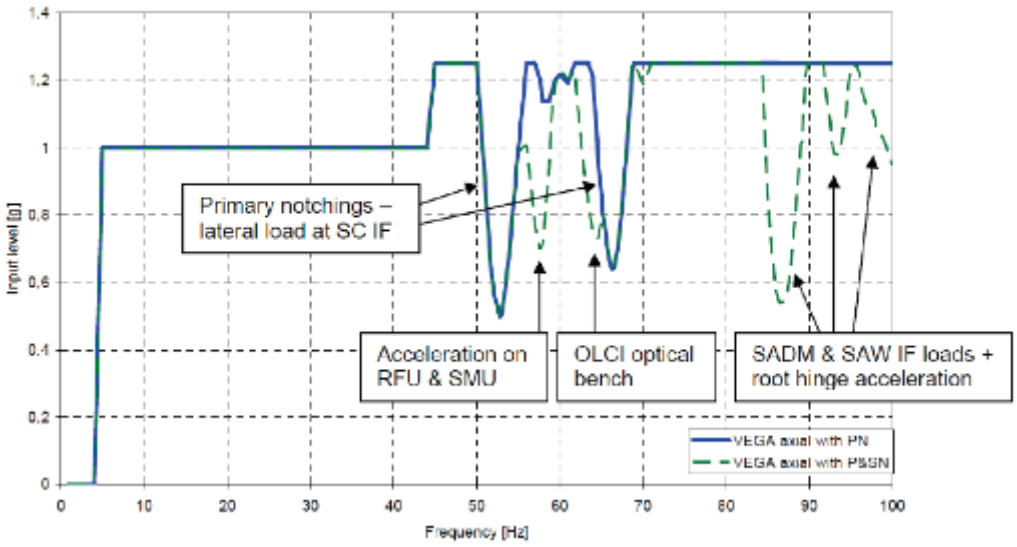

Figure 2.20. Example of Primary and Secondary Notching for Sentinel 3[13]

2.6 Mathematical Validation of the Satellite

With the increasing usage of finite element models in engineering and the generation of complex finite element models to estimate load paths and the strength of structures; research, and implementation of finite element model update methodologies are increased. The communication satellites have many natural frequencies below 100Hz, which cause dynamic coupling of structure parts and launchers[19]. As a result of this, the correlation and validation of the satellite finite element model become complex and crucial. Validation of the satellite finite element models using the sine test results becomes crucial for the following reasons:

- Validation of critical response of the satellites during launch,
- Verification of structural design and components on the satellite,
- Decrease system-level risk that can be faced during launch.

Correlation is the demonstration of similarity between two models: numerical calculation using finite element methods and the test data. According to [20], spacecraft design can be correlated by using dynamic response measurement via model assurance criteria checks. In Figure 2.21, a correlation flowchart of the spacecraft structure is demonstrated. There should be systematic identification of model updates, which can be specified as error location procedure, structural parameter selection, and parameter estimation. The location of the error in the frequency domain is performed by comparing numerical results and test results. Structural parameter selection is to define relevant structural parameters which are sensitive to the related result of interest. Parameter estimation is the process of parameter value iterations by using programming methods.

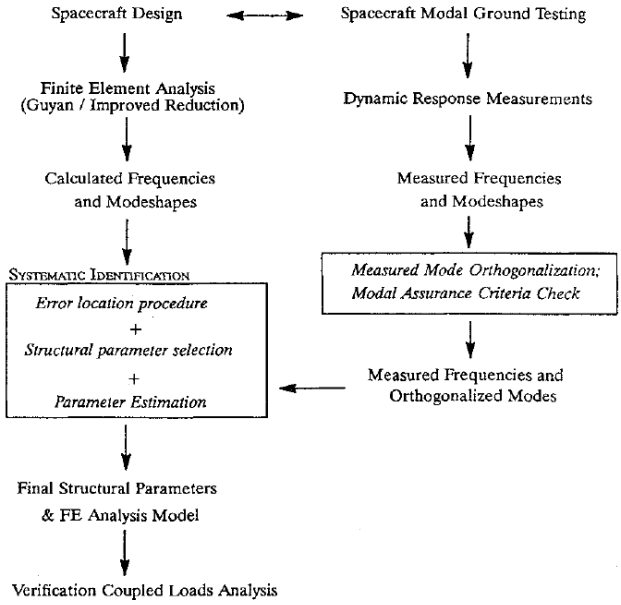

Figure 2.21. Analysis/Test Correlation for Spacecraft structures [20]

Error location process in the frequency domain is the first step of the finite element model validation. The most crucial method to compare dynamic test results and numerical results is modal assurance criteria. The modal assurance criteria are the

quality assurance indicator for experimental modal vectors that are estimated from the measured frequency response function[21].

$$\boldsymbol{MAC_{cdr}} = \frac{\left|\sum_{q=1}^{N_o} \boldsymbol{\psi_{cqr}\psi^{\star}_{dqr}}\right|^{2}}{\sum_{q=1}^{N_o} \boldsymbol{\psi_{cqr}\psi^{*}_{cqr}} \sum_{q=1}^{N_o} \boldsymbol{\psi_{dqr}\psi^{*}_{dqr}}} \qquad \text{Eq. 1 [21]}$$

In Eq. 1, ψ_{cqr} is the modal coefficient for reference c, degree-of-freedom q and mode r. ψ^{*}_{cqr} is the complex conjugate of ψ_{cqr}.

In criteria matrices, values are changing from 0 to 1. The diagonal values close to 1 and off-diagonal values close to 0 show a perfect correlation between two sets of data. 2D and 3D representations of MAC values are shown in Figure 2.22.

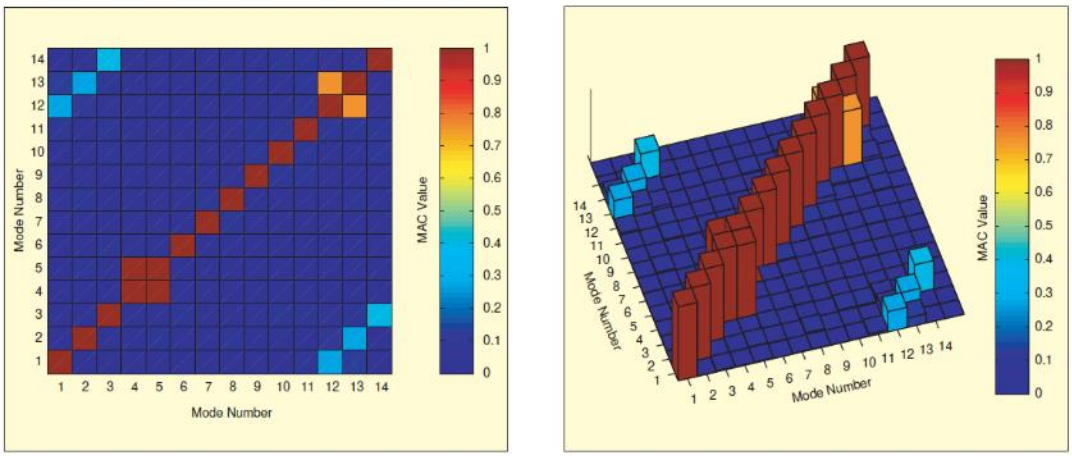

Figure 2.22. 2D and 3D presentation of MAC Values[21]

The frequency response assurance criterion (FRAC) compares the frequency response function at each frequency calculated by numerical calculation and test result.

$$\mathbf{FRAC} = \frac{|\{\boldsymbol{X^a(f)}\}^T\{\boldsymbol{X^t(f)}\}|^2}{|\ \boldsymbol{X^a(f)}\}^T\{\boldsymbol{X^a(f)}\ \|\ \{\boldsymbol{X^t(f)}\}^T\{\boldsymbol{X^t(f)}\}\ |} \qquad \text{Eq. 2 [19]}$$

The frequency-domain assurance criteria (FDAC) is similar to MAC and compares two vectors measured in the frequency domain, which are numerical and test.

$$\mathbf{FDAC}(\boldsymbol{f_i^a, f_i^t}) = \frac{|\{\boldsymbol{X_m^a(f_i^a)}\}^T\{\boldsymbol{X_m^t(f_i^t)}\}|^2}{|\ \boldsymbol{X_m^a(f_i^a)}\}^T\{\boldsymbol{X_m^a(f_i^a)}\ \|\ \{\boldsymbol{X_m^t(f_i^t)}\}^T\{\boldsymbol{X_m^t(f_i^t)}\}\ |} \qquad \text{Eq. 3 [19]}$$

In Eq. 2 and Eq. 3, m denotes measurement point and X is measured or calculated acceleration. f_i^a and f_i^t represents paired natural frequencies for analysis and test respectively.

In his study, Lim[19] showed correlation studies of the satellite by using FRAC and FDAC by including sensitivity analysis.

Another method mentioned in another study [22] is the base force assurance criterion (BFAC). This criterion uses force and moment values at the interface proportional to the effective mass of structure at each frequency.

$$\boldsymbol{BFAC_{jk}} = \frac{\left(\boldsymbol{P_j^T F_k}\right)^2}{\left(\boldsymbol{P_j^T P_j}\right)\left(\boldsymbol{F_k^T F_k}\right)} \qquad \text{Eq. 4 [22]}$$

In Eq. 4, P is the absoulute of force value that is transmitted to the structure in the frequency domain. F is the calculated force at the interface of the structure with the shaker.

Sairajan and Aglietti [22] used BFAC as a correlation criterion, and they stated that the BFAC criterion is more suitable for the tests with base excitations.

According to ECSS, a comparison of test and analysis criteria is given in frequency deviation and MAC values, which is shown in Table 2.4.

Table 2.4. Test-analysis Correlation criteria of ECSS [13]

Item	**Quality Criterion**	
Fundamental bending modes of a spacecraft	MAC:	>0.9
	Eigenfrequency deviation:	<3%
Modes with effective masses > 10% of the total mass	MAC:	>0.85
	Eigenfrequency deviation:	<5%
For other modes in the relevant frequency range	MAC:	>0.8
	Eigenfrequency deviation:	<10%
Cross-orthogonality check	MAC:	>0.9
	Eigenfrequency deviation:	<0.1

The other necessary procedure is error localization. Error localization is the determination of which part of the mathematical model needs to be modified. According to the study by Link and Santiago[23], substructure energy functions can be used for error localization. The larger value of the energy function indicates that it is sensitive to modifications. Strain energy function can be expressed as

$$\boldsymbol{\Delta\Pi_j^S} = \sum_{\boldsymbol{h=1}}^{\boldsymbol{N}} (\boldsymbol{\phi_{ah}} - \boldsymbol{\phi_{mh}})^{\top} \boldsymbol{K_j} (\boldsymbol{\phi_{ah}} - \boldsymbol{\phi_{mh}}) \qquad \text{Eq. 5 [23]}$$

and kinetic energy function as,

$$\boldsymbol{\Delta\Pi_j^K} = \sum_{\boldsymbol{h=1}}^{\boldsymbol{N}} (\boldsymbol{\phi_{ah}} - \boldsymbol{\phi_{mh}})^{\top} \boldsymbol{M_j} (\boldsymbol{\phi_{ah}} - \boldsymbol{\phi_{mh}}) \boldsymbol{\omega_{mh}^2} \qquad \text{Eq. 6 [23]}$$

In Eq. 5 and Eq. 6, M_j and K_j are the mass and stiffness matrices.

Finite element model updating is to correct the numerical values used in a mathematical model using test data obtained[24]. The numerical model estimations may differ from the physical model, including interfaces, material properties, and boundary conditions. According to[25], there are two methods for finite element model updating, which are;

- Direct Methods
- Iterative Methods

In the direct methods, mathematical models' stiffness and mass matrices are directly modified to increase the similarity between test and analysis results. Generally, finite element models have a large number of elements which results in high mass and stiffness matrix dimensions. These models require a reduction of numerical models to test model, which will reduce mass and stiffness matrices dimensions of a detailed model to the sensor set of vibration tests. One of these reduction techniques is Guyan reduction.

Wang et al. [20] and Aglietti et al. [26] used Guyan reduction to validate satellite finite element mode in their studies. The main drawback of direct methods by using reduction is the direct modification of mass and stiffness matrices. These modifications will satisfy the correlation between test and analysis, whose correlation criteria are given in Table 2.4; however, the sensitivity of the numerical model will be lost[19].

The objective of the iterative methods using test data is to improve correlation like in the direct methods. However, modifications are implemented by using a comprehensive alternative of parameters to the finite element model, not by directly mass and stiffness matrices. With respect to direct methods, iterative methods combined with sensitivity analysis are more powerful and efficient. The main difficulty of this method is setting parameters due to many uncertainties on the finite element model. This implementation is highly dependent on engineering experience.

Stochastic methods are implemented for model updates to overcome the necessity of engineering experience and not to face unreasonable model updates. Stochastic methods are based on probabilistic methods. This method minimizes the inaccurate implementation of parameter modification. One of the methods is the Bayesian update, which was implemented in the study by Calvi et al. [27]. In this study, sampling-based algorithms for the Bayesian update procedure were implemented where multi-level Markov chain Monte Carlo algorithms were adopted[27].

$$\boldsymbol{P}(\ \boldsymbol{\theta} \mid \boldsymbol{D}, \boldsymbol{M}\ ) = \frac{\boldsymbol{P}(\boldsymbol{\theta} \mid \boldsymbol{D}, \boldsymbol{M})\boldsymbol{P}(\boldsymbol{\theta} \mid \boldsymbol{M})}{\boldsymbol{P}(\boldsymbol{D} \mid \boldsymbol{M})} \qquad \text{Eq. 7 [27]}$$

In this formula, θ is referred to as adjustable unknown, $\mathcal{D}$ denotes experimental data, and M is the knowledge and experience of the engineer.

Drawbacks of stochastic methods are specified in the study of Calvi et al. [24]. Firstly, stochastic methods are complicated and computationally expensive, which requires parallelization. Another feedback is the characterization of structural uncertainty. Implementation of the stochastic method is difficult and time-consuming. It is dependent on satellite structural configuration, manufacturing, and materials that are used. In Figure 2.23, a mathematical parameter update of the reflector as a result of the correlation is shown.

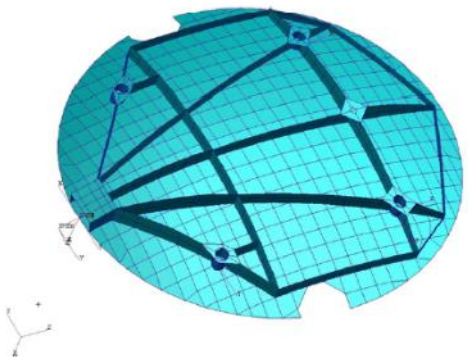

No.	Description	θ_{nom}	θ_{ref}	Δ (%)
Dish/ribs bracket stiffnesses [N/m] (TS), [N/rad] (RS)				
1	TS: ribs 1,2,4,17–20,22,23,25,26	1.00E7	5.00E5	95
2	TS: ribs 3,5,21,24	7.50E7	3.00E7	60
3	TS: ribs 6,11	1.30E8	1.95E8	−50
4	TS: ribs 7,9,12,14	1.50E8	8.25E7	45
5	TS: rib 8	1.00E8	1.50E8	−50
6	TS: rib 13	8.00E7	5.60E7	30
7	TS: rib 10	5.00E7	6.25E7	−25
8	TS: rib 15	1.00E8	5.50E7	45
9	RS: ribs 1,2,4,17–20,22,23,25,26	1.00E3	1.70E3	−70
10	RS: ribs 3,5,21,24	1.50E3	5.25E2	65
11	RS: ribs 6,11	2.50E3	3.63E3	−45
12	RS: ribs 7,9,12,14	3.00E3	4.05E3	−35
13	RS: rib 8	2.00E3	5.00E2	70
14	RS: rib 13	1.60E3	2.16E3	−35
15	RS: rib 10	1.00E3	7.50E2	25
16	RS: rib 15	2.00E3	7.00E2	65
17	RS: ribs 9,14	3.00E3	1.50E3	50
Dish/box bracket stiffnesses [N/m] (TS), [N/rad] (RS)				
18	TS 1	1.0E8	1.40E8	−40
19	TS 2	6.0E6	1.02E7	−70
20	RS 1	2.0E3	1.20E3	40
21	RS 2	1.0E2	7.00E1	30
Young's moduli [N/m^2]				
22	RS3/XN50: x-dir.	2.35E11	2.23E11	5.0
23	RS3/XN50: y-dir.	5.43E9	5.97E9	−10
24	RS3-C/Kevlar 49 Fabric [0,90]: x-dir.	2.41E10	2.23E10	7.5
25	RS3-C/Kevlar 49 Fabric [0,90]: y-dir.	2.57E10	5.99E10	5.0
26	RS3-C/T300 Fabric [0,90]: x-dir.	6.14E10	2.44E10	2.5
27	RS3-C/T300 Fabric [0,90]: y-dir.	6.17E10	6.36E10	−3.0
28	Core Kevlar / Epoxy: HRH: x-dir.	1.90E8	2.01E8	−6.0
29	Core Kevlar / Epoxy: HRH: y-dir.	2.30E8	2.28E8	1.0
30	Core Kevlar / Epoxy: HRH: x-dir.	1.80E8	1.73E8	4.0
31	Core Kevlar / Epoxy: HRH: y-dir.	2.00E8	1.88E8	6.0
32	Core AL: x-dir.	3.46E8	3.20E8	7.5
33	Core AL: y-dir.	3.03E8	2.88E8	5.0
34	Adhesive Hysolea	1.12E11	1.14E11	−2.0
35	Titanium	2.41E9	2.22E9	8.0
36	Laminate: x-dir.	4.25E10	3.83E10	10
37	Laminate: y-dir.	4.25E10	4.04E10	5.0

Figure 2.23. FE Model and Updated Parameters of Model[27]

CHAPTER 3

FINITE ELEMENT MODELLING AND TEST OF THE COMMUNICATION SATELLITE

3.1 Introduction

This section explains the overall design of the communication satellite and the finite element model of the satellite. Primary and secondary structural parts of the communication satellite are described. Firstly, panel descriptions, interface, and material types that are used in the satellite are mentioned. Then finite element model description, element types, panel, and material properties are given. Lastly, validation methods and results are presented in this chapter.

3.2 Structural Model of the Communication Satellite

The satellite structural architecture's primary purpose is to withstand the environmental loads that the satellite will be exposed during its service life and satisfy all subsystems' functional requirements in the satellite. Besides, it ensures access to necessary equipment and structural parts during the assembly phase.

Design of the communication satellite structure starts with mission definition, payload accommodation, thermal radiator calculations, launch mass estimations, solar array, and reflector dimension specifications with respect to mission specification. With every design and analysis iteration, the maturity of the structure increases and finalizes with launch configuration.

During these design and analysis iterations, the coordinate system shown in Figure 3.1 is used. The coordinate system's origin is the center of the launcher interface ring, which is located on the satellite-launcher interface plane. The direction towards Earth

is Z-axis. The satellite's flight direction in orbit is defined as the X-axis and the Y-axis perpendicular to both axes. The positive X-axis is called the East direction, and the positive Y-axis is called the South direction.

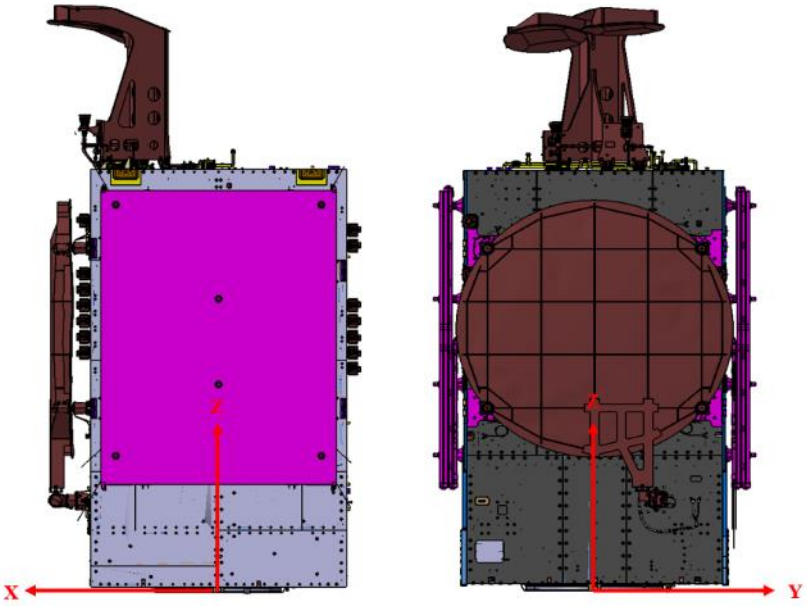

Figure 3.1. Coordinate System of the Satellite

In this thesis, the communication satellite is designed in accordance with traditional structural architecture. Generally, in communication satellites, the central cylinder is the main load-bearing member of the satellite structure. The central cylinder provides the interface of the satellite to the launcher. The structural panels that have an interface to the central cylinder are the shear panels and horizontal decks. The communication and service panels are integrated into the satellite through these shear panels. The solar panels and reflectors on the outside of the satellite are integrated into the communication panels.

With respect to each subsystem, the communication satellite's mass distribution is evaluated in the study is given in Table 3.1. As seen in Table 3.1, the satellite has a

chemical propulsion system, which is 52.5% of the total satellite mass. Two propellant tanks are located inside the central cylinder, which carries 1658.17kg of propellant. The central cylinder provides general strength and stiffness to the satellite. Outer panels are integrated to the central cylinder via the shear panels and decks. Loads acting on these panels are transmitted to the central cylinder and via the shear angle webs.

Table 3.1. Mass Distribution of the Satellite

Subsystems	**Mass [kg]**	**Percentage [%]**
Structural Subsystem	424.94	13.5%
Thermal Subsystem	101.80	3.2%
Payload Subsystem	283.95	9.0%
Electrical Power Subsystem	276.80	8.8%
Harness Subsystem	94.96	3.0%
Attitude Control Subsystem	58.73	1.9%
Propulsion Subsystem	180.37	5.7%
Propellant	1658.17	52.5%
Command Data Handling Subsystem	32.63	1.0%
Communication Subsystem	43.95	1.4%
Total	3156.31	

Sandwich panels are used in the structure of the satellite. Aluminum or Carbon Fiber-Reinforced Polymer (CFRP) skin sandwich panels are preferred concerning the equipment's thermal requirements on related panels. The regions where highly heat dissipating equipment are mounted, aluminum embedded heat pipe sandwich panels are preferred. Heat pipes distribute the heat homogeneously through the panel and dissipate it into space by radiation. For the other panels, composite ones are used for mass reduction and high stiffness purposes. Composite and aluminum panel examples are given in Figure 3.2.

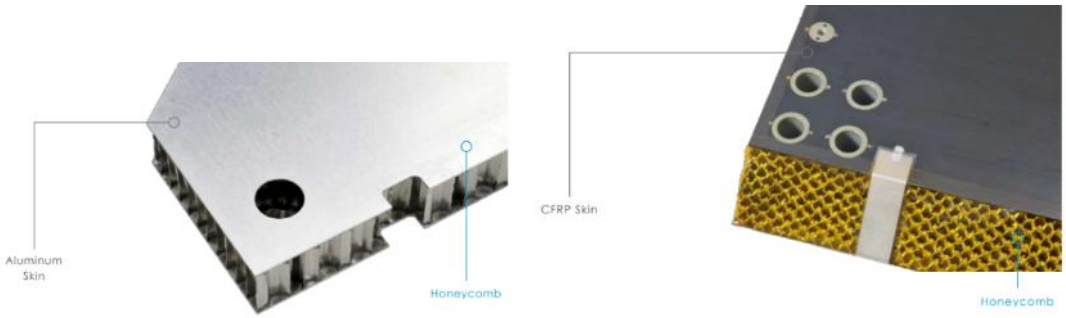

Figure 3.2. Example of CFRP and Aluminum Sandwich Panel [28]

The structure panels are connected with brackets and direct panel to panel connections via inserts. For panel to panel and equipment to panel connections, different types of embedded inserts are designed and used in the sandwich panels. With respect to the required allowable of inserts, through-the-thickness, fully potted, and partially potted inserts are used in the satellite, which is shown in Figure 3.3. Different densities of honeycombs and skin thicknesses are optimized in panels with respect to the structural inserts' strength.

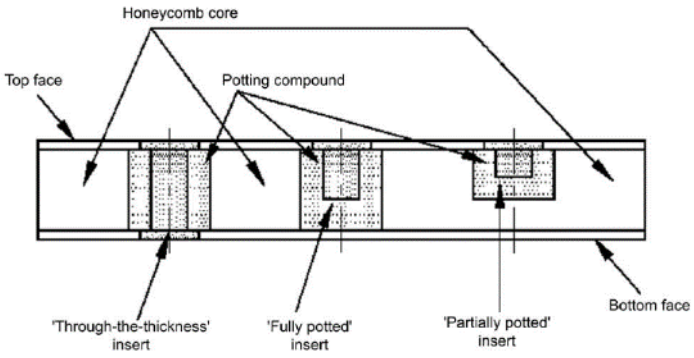

Figure 3.3. Structural Inserts Types [13]

The structural subsystem is divided into primary and secondary structures:

1. Primary structures are the main structural components that carry the environmental loads acting on the satellite during launch, test, and ground operations and provide the required stiffness.
2. Secondary structures support the primary structure and mostly withstand the local loads caused by acoustic and sinusoidal vibration on the satellite. Another function of secondary structures is to carry other subsystem equipment and meet their functional requirements.

The primary structure consists of a central cylinder, the shear panels, the anti-earth deck, the mid-deck, and the earth deck. Secondary structures are communication panels and service panels. The general panel naming of the communication satellite is given in Figure 3.4.

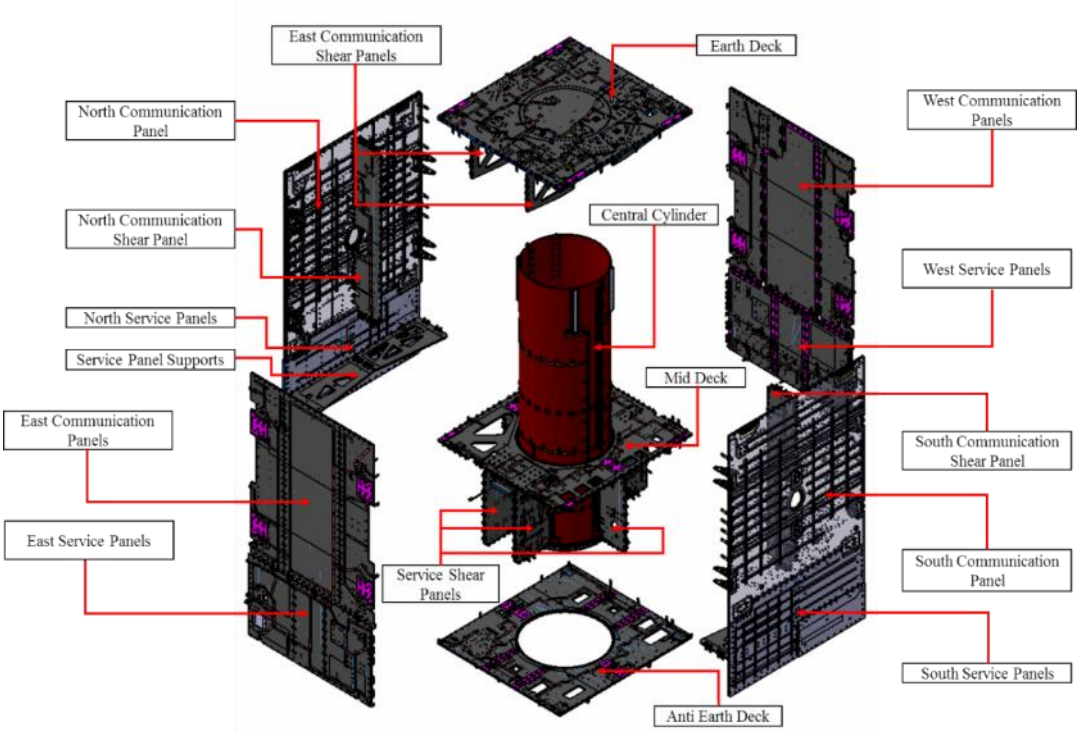

Figure 3.4. Structural Parts of the Satellite

The Central Cylinder is the main component of the primary structure and transfers loads acting on the satellite during the launch to the launcher via the adaptor. The Chemical Propulsion System's fuel tanks are located within the central cylinder structure, whose mass is half of the satellite. In addition to the two tanks, the altitude control subsystem's reaction wheels are attached to the central cylinder, requiring high dimensional stability. Central Cylinder is a CFRP sandwich structure and includes metallic frames, flanges, inserts, and aluminum ring parts. Other primary structural components are assembled to the central cylinder, which are the shear panels and the decks.

The anti-earth deck carries sensors and reaction control thrusters of the satellite. Mid-deck is the panel between the communication module and the service module. It provides interfaces between communication and service modules. The harness between the service module and communication module pass-through this panel via cutouts. Earth deck carry tower, feeder of payload module, and star trackers of altitude control subsystem. The horizontal decks of satellites are CFRP sandwich panels, and the thickness of the honeycomb differs with respect to the bending stiffness of panels.

The most critical panels to transfer loads from outer panels to the central cylinder are the shear panels. Shear panels are working under shear loads. These panels are CFRP sandwich panels to provide stiffness and strength.

The north and south service panels carry power and altitude control subsystem equipment. These panels are aluminum heat pipe embedded sandwich structural panels, which is mandatory to reject excessive heat dissipating from power subsystem equipment. These panels are connected to the central cylinder via north and south shear panels.

The east and west service panels are mainly used as access panels and carry antenna deployment mechanism support. So as to increase stiffness and decrease the mass of the panel, CFRP sandwich structures are used.

Payload and telecommand subsystems have high heat-dissipating equipment, which requires them to be placed on north and south communication panels. Heat rejects from aluminum sandwich panels with a sophisticated heat pipe network via radiation. Besides, the solar array drive mechanism and hold-release mechanisms are attached to the north and south panels. The loads are transferred from these panels with the north and the south communication shear panels to the central cylinder.

East and west communication panels carry reflectors and provide access to the interior of the satellite during assembly and integrations. The hold and release mechanisms of the reflector are located on these panels. These panels are CFRP sandwich panels to provide stiffness and mass reduction.

Tower, solar array, and reflector of satellites are mounted to outer panels of the satellites. These structures consist mainly of aluminum and CFRP panels. These appendages are shown in Figure 3.5.

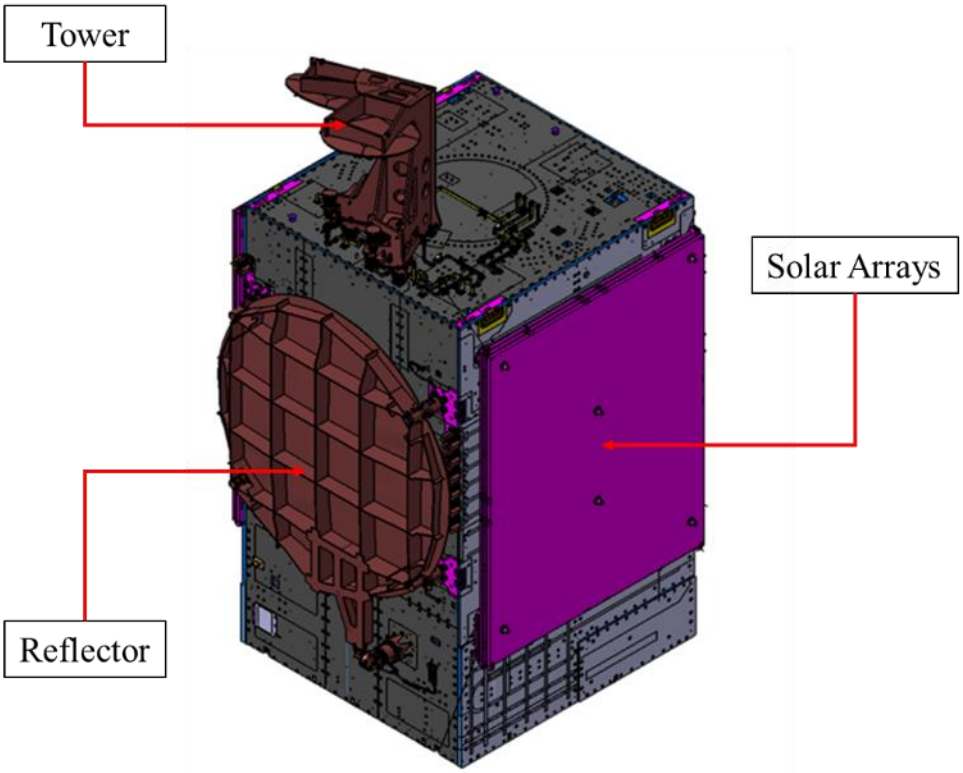

Figure 3.5. Appendages of the Satellite

3.3 Finite Element Model of the Communication Satellite

During design and analysis iterations of the structural subsystem, various types of analysis are performed, which are given in the following:

- Quasi-static analysis
- Eigen frequency calculation
- Frequency-response analysis
- Global Buckling analysis

The finite element method is used to assess the structural strength and dynamic behavior of the satellite. It is critical to understand structural behavior and select

correct elements to obtain the correct mathematical model of the satellite. The increasing complexity of the finite element model causes difficulty in evaluating results and causes unnecessary computational load.

At the beginning of the global finite element model generation, the mesh convergence study is performed on the central cylinder by using CQUAD4 elements. The first bending frequency of the central cylinder is the objective of the convergence study. Element sizes from 400mm to 40mm are investigated, and results are given in Table 3.2.

Table 3.2. Mesh Convergence Iterations

Element Size [mm]	**Number of Element**	**First Bending Frequency of Central Cylinder [Hz]**
400	91	62.57
300	156	63.45
200	360	64.06
150	676	64.29
100	1480	64.43
50	5921	64.53
40	9140	64.55

It is observed that 40mm is an effective element size to have accurate eigenvalue results. In Figure 3.6, the mesh convergence graph is demonstrated. The different element size in the central cylinder is shown in Figure 3.7. In the satellite's global finite element model, there are 9105 elements with approximately 40mm element size in the central cylinder. For the satellite primary structure, the maximum element size is chosen as 40mm.

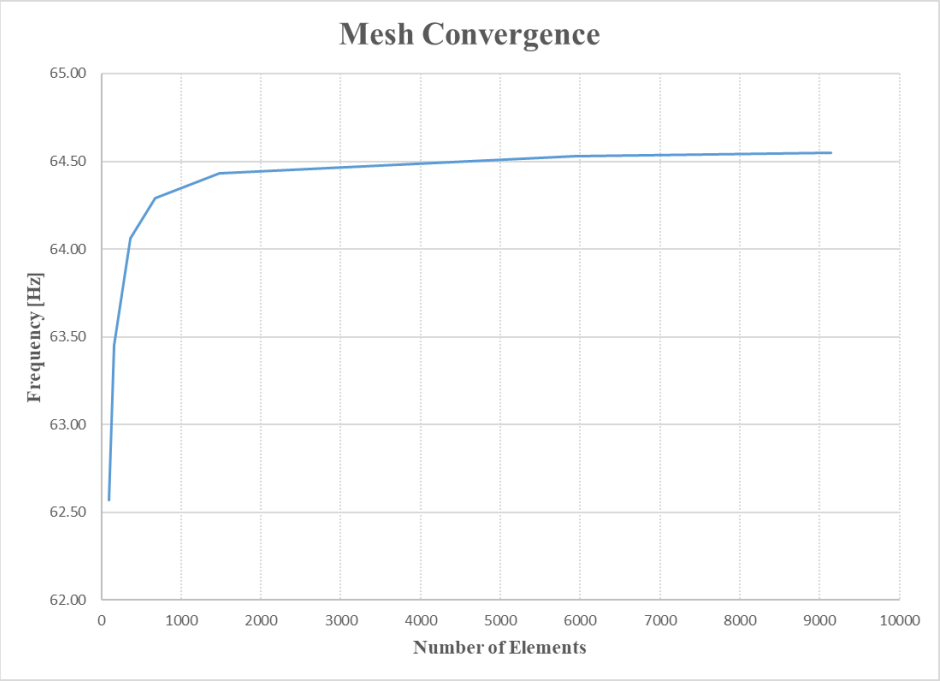

Figure 3.6. Mesh Convergence Graph of Central Cylinder

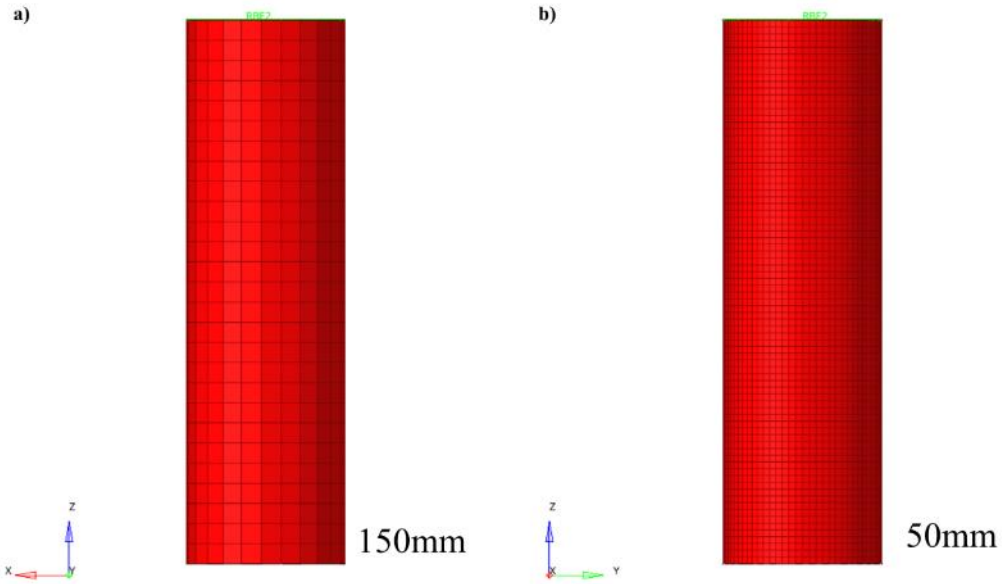

Figure 3.7. Example of Central Cylinder Finite Element Model with Different Element Size

In this study, only eigenvalue and frequency response analyses are considered. A global finite element model (FEM) is generated to assess the dynamic behavior of the structure. Since the satellite's global stiffness is the most critical case in eigenvalue and frequency response analysis, only its primary and secondary structure is modeled. Structural panels are included in FEM using low-order elements. Interfaces, brackets, small cutouts, and equipment are not included in FEM details. Major components that have natural frequency up to 120Hz at hard-mounted conditions are included in FEM, which are solar arrays, reflectors, towers, and tanks. In the sine vibration test, these equipment are dynamically coupled with the structure's panels, and it is crucial to include them in FEM in order to get accurate results. Other equipment with higher natural frequencies are integrated to FEM with structural point mass. Interface between structural parts is modeled with rigid elements and beam elements. Other structural parts and equipment are included in FEM as a distributed mass. The FEM of the satellite is shown in Figure 3.8.

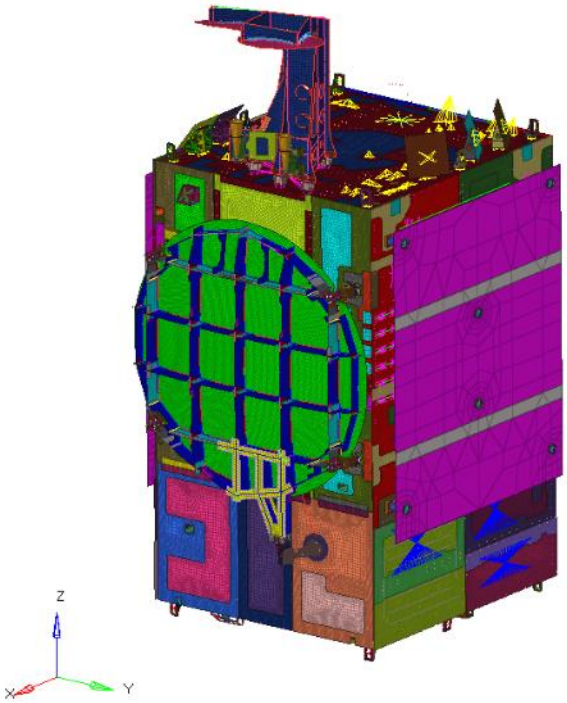

Figure 3.8. Finite Element Model of the Satellite

Hypermesh is used for FEM generation of the satellite, and MSC NASTRAN is used as solver. All structural panels used in the satellite's primary and secondary structure are the sandwich panels with aluminum and CFRP skins. As indicated previously, in order to get high stiffness with less structural mass, sandwich panels are preferred. Sandwich panels are simplified with two-dimensional quadrilateral and triangular shell elements, which are CQUAD4 and CTRIA3 at their mid-surface. CTRIA3 elements are generally used in the transition region and are avoided to be used in FEM since these elements are stiffer than CQUAD4 elements.

Properties of the sandwich panels are created with PCOMP property in MSC NASTRAN. For Aluminum sandwich panels, three layers of composite properties are defined. The first and third plies represent aluminum skins, and the second ply represents honeycomb. For CFRP sandwich panels, laminate is defined with respect to each lamina ply orientation.

Additionally, aluminum sandwich panels have embedded and external heat pipes for thermal control purposes. However, these heat pipes increase the stiffness of the panel and work as a stiffener. These heat pipes are modeled with the one-dimensional element, which is the CBEAM element. CBEAM elements are preferred since they carry bending, and shear loads and are more representative than CROD elements.

Especially in solar arrays, reflectors, and reaction wheels, there are major thickness variations in their structural parts. These parts are modeled with three-dimensional CTETRA and CHEXA elements. CTETRA elements are preferred in regions with complex geometrical shapes and various thicknesses.

Multipoint constraints (MPC) are used in the panel-to-panel interface and equipment-to-panel interface. Two types of multipoint constraints are used, which are RBE2 and RBE3 elements. RBE2 elements are used for connection purposes and simulate fasteners. Since RBE2 elements have infinite stiffness, zero-length spring (CBUSH) elements are used in panel-to-panel interfaces to include fasteners' stiffness and evaluate loads affecting the fasteners. Another purpose of the RBE2 usage is to distribute equipment loads to panels. Equipment that have a natural

frequency higher than 120 Hz are modeled with concentrated mass elements (CONM2), and RBE2 elements are used to distribute loads caused by CONM2 to the panels. RBE3s are only used to read cumulative forces and accelerations in the interface regions of appendages and equipment.

Tank models are integrated into the global finite element model as super elements. These elements have only mass and stiffness matrices for related interface nodes. Visualization of these super elements are performed with PLOTEL elements

The element types, number of elements, and nodes in FEM are given in Table 3.3.

Table 3.3. Element Types and Numbers, Node Numbers

Element Type	**Number**
CROD	2370
CBEAM	9795
CQUAD4	450835
CTRIA3	41550
CHEXA	1364
CTETRA	114073
RBE2	5172
RBE3	190
CONM2	294
CBUSH	3602
PLOTEL	797
Total Element	*630042*
GRID POINTS	720859

The central cylinder is modeled with CQUAD4 and CTRIA3 elements. Tanks that are modeled with supplements are integrated into the central cylinder with RBE2 elements. In addition, reaction wheels are modeled with CTETRA elements, which have complex geometrical shapes and various thicknesses. Central Cylinder, tanks, and Reaction wheels are shown in Figure 3.9.

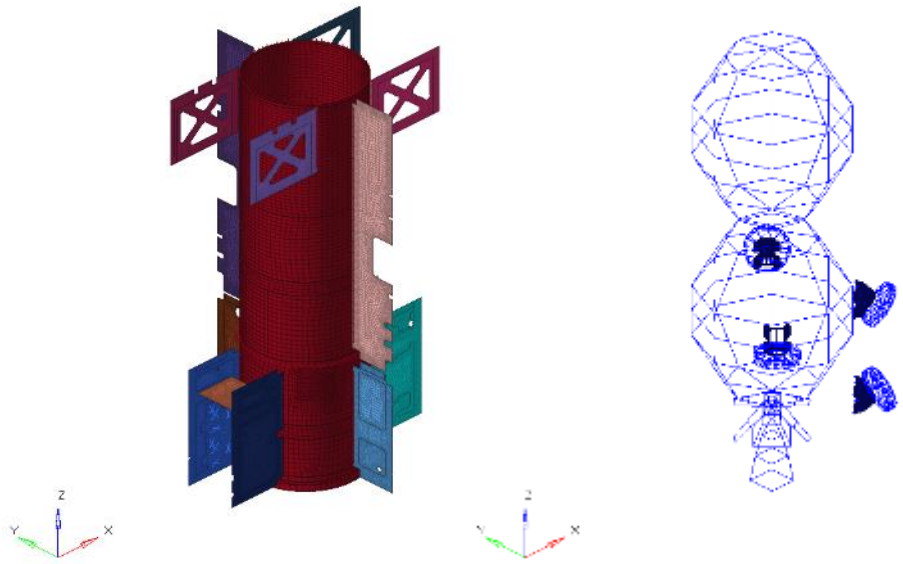

Figure 3.9. FEM of Central Cylinder, Shear Panels and Super-Element Models of Tanks and Reaction Wheels

Shear panels, anti-earth, mid, and earth deck connections are modeled with CBEAM and RBE2 elements. CBUSH elements are used to represent interface stiffness. Central cylinder is an orthotropic CFRP sandwich structure with a variable thickness along its length. While the bottom side has high number of plies, the top part has the minimum number of plies in their skin. The main purpose is to satisfy the satellite's bending stiffness and have strength at the bottom, which is highly loaded during launch. In addition, there are also reinforcements in plies around tank interface to satisfy skin strength. FEM of the central cylinder and different properties are given in Figure 3.10. In Figure 3.10 (b), different colors represent different properties of the central cylinder.

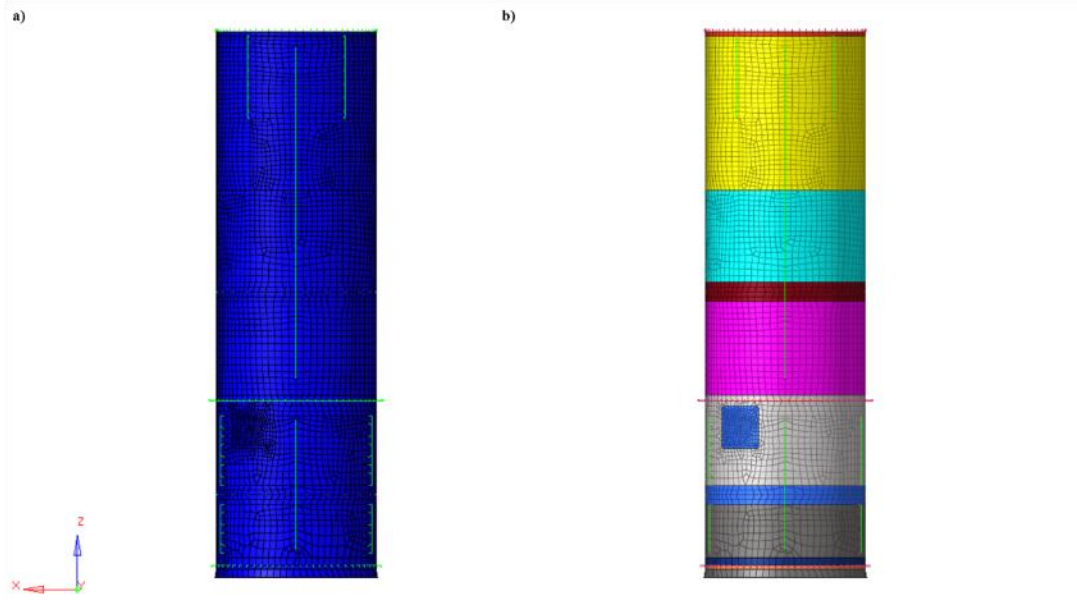

Figure 3.10. (a) The FEM of Central Cylinder, (b) Different Properties of the Central Cylinder

The Shear Panels are transition panels between the outer surface of the satellite and the central cylinder. These panels are modeled with CQUAD4 and CTRIA3 elements and interface from other panels modeled with RBE2 and CBUSH elements. The shear Panels are CFRP sandwich panels, and properties are included with PCOMP cards in NASTRAN. Since these panels carry shear loads, ply orientations are 45°, and lamina properties are quasi-isotropic properties. These shear panel edges have embedded inserts for interface purposes, and in structural design, there are doublers to increase inserts in-plane load carrying properties. Furthermore, a high-density honeycomb is preferred at insert regions to increase inserts' out-of-plane allowable. This kind of property difference in panels is included in FEM with different PCOMP properties. In Figure 3.11, the FEM of communication shear panels and service shear panels are shown.

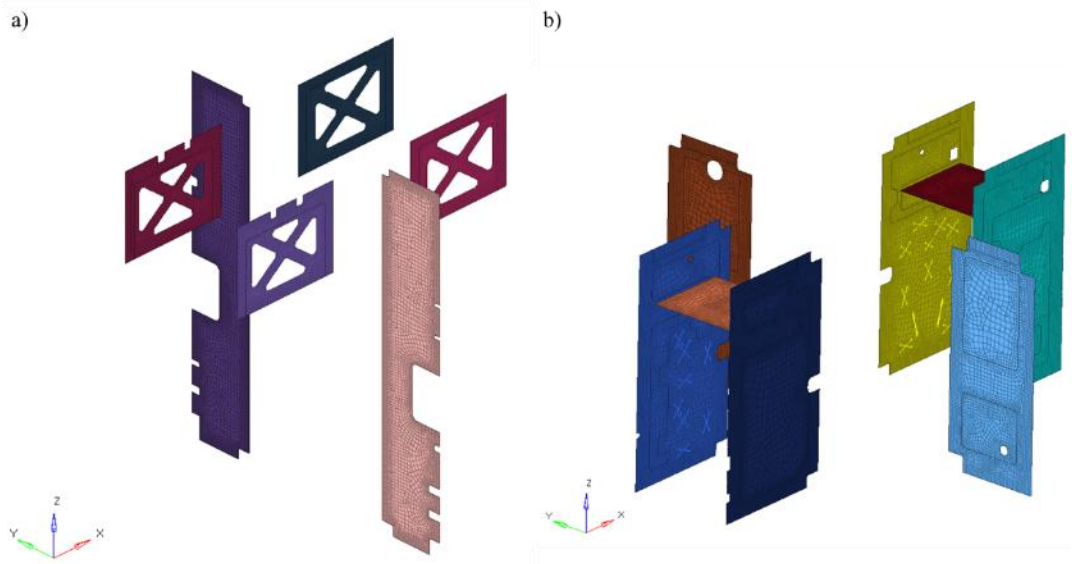

Figure 3.11. The FEM of (a) the Communication and (b) Service Shear Panels

Decks are CFRP sandwich panels and modeled with CQUAD4 and CTRIA3. The Anti-Earth deck has four pieces of panels, while the mid-deck has two panels because of assembly and integration purposes. Star trackers are mounted on the earth deck, and thrusters are mounted to the anti-earth deck, which is shown in Figure 3.12. These equipment are modeled with CQUAD4 and CTRIA3 elements and connected to decks via RBE2 and CBUSH elements. Other equipment modeled with concentrated mass. Mid-deck and anti-earth decks have large cutouts, which are modeled in FEM as well.

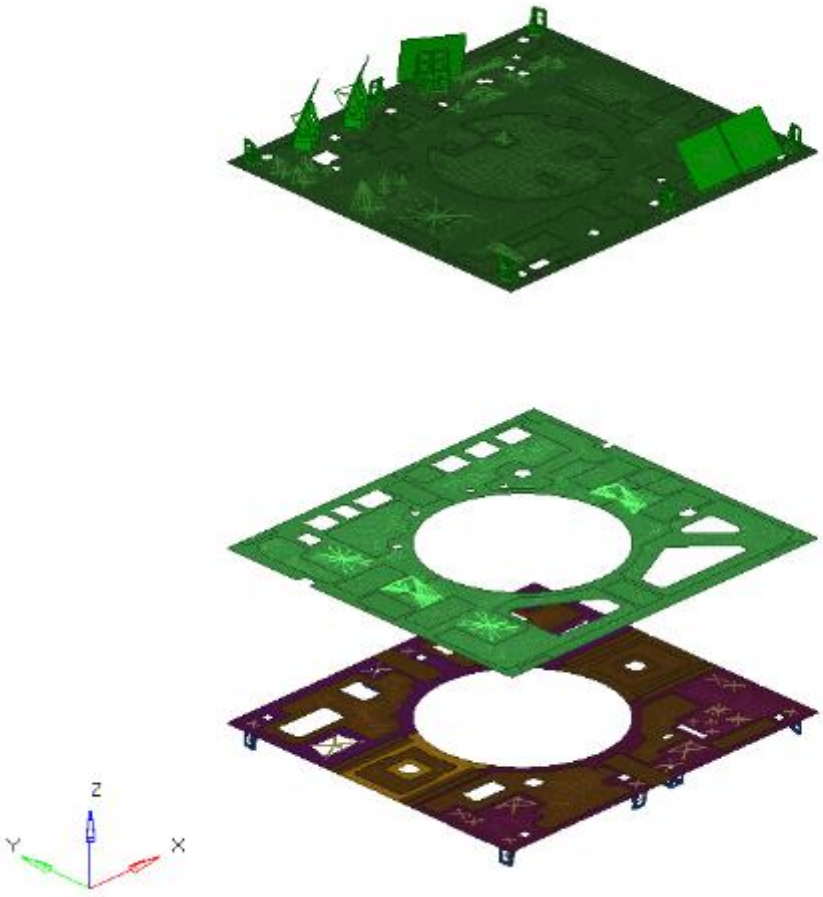

Figure 3.12. The FEM of Satellite Decks

Interface with other panels are implemented with RBE2 and CBUSH elements. Ply orientations of skin are 60°, and lamina properties are quasi-isotropic properties. Like in other structural panels, there are different skin thickness and honeycomb density properties among panels to increase in-plane and out-of-plane stiffness. These differences are included with PCOMP property cards in MSC-Nastran. Details of decks FEM are given in Figure 3.13.

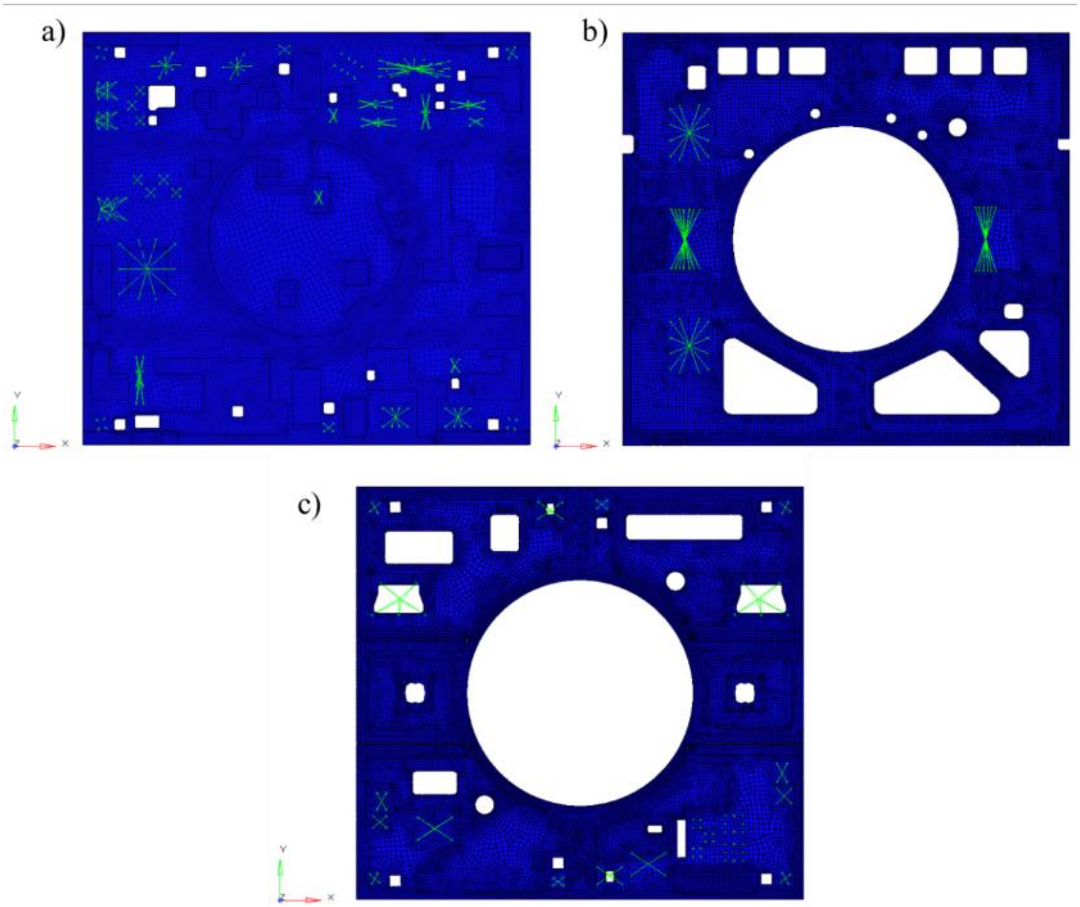

Figure 3.13. The FEM of (a) Earth Deck, (b) Mid Deck, and (c) Anti-Earth Deck

The communication module consists of four parts, which are shown in Figure 3.14. North and south communication modules are single pieces of aluminum sandwich panels. These panels host payload equipment, solar array hold, and release mechanism, and solar array drive mechanism. East and west communication panels have three pieces of CFRP sandwich panels because of assembly and integration purposes. Reflector's hold and release mechanisms are integrated into these panels.

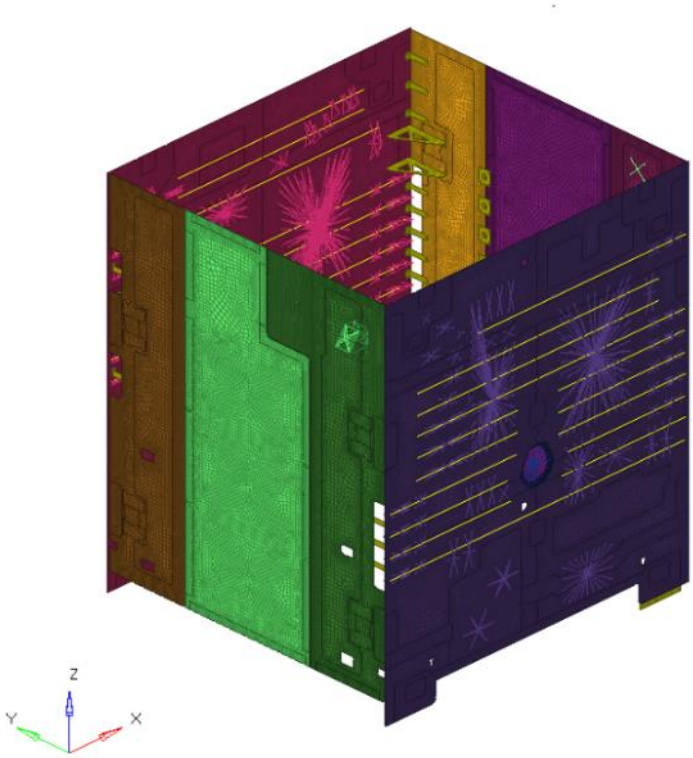

Figure 3.14. The FEM of Communication Module

North and south communication panels are modeled with CQUAD4 and CTRIA3 elements. Payload equipment are modeled with CONM2 elements. Embedded heat pipes are used to design these panels, and these heat pipes are modeled with CBEAM elements. Two-dimensional element nodes and CBEAM nodes are equivalence to include heat pipes' bending stiffness in panel stiffness. The aluminum sandwich structure is used in panels, and mechanical properties are included with PCOMP cards. In addition, local reinforcements are included in the model. Detailed FEM of north and south communication panels are given in Figure 3.15.

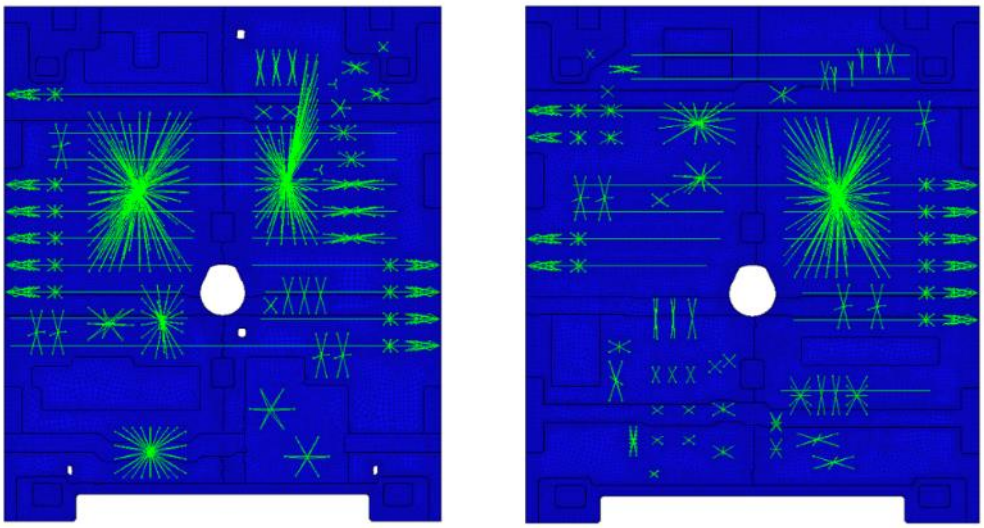

Figure 3.15. The FEM of South and North Communication Panels

East and west communication panels are CFRP sandwich structures and modeled with CQUAD4 and CTRIA3 properties. Ply orientations of skin are 60°, and local reinforcements with different honeycomb densities are implemented with PCOMP cards. There is not any equipment on these panels.

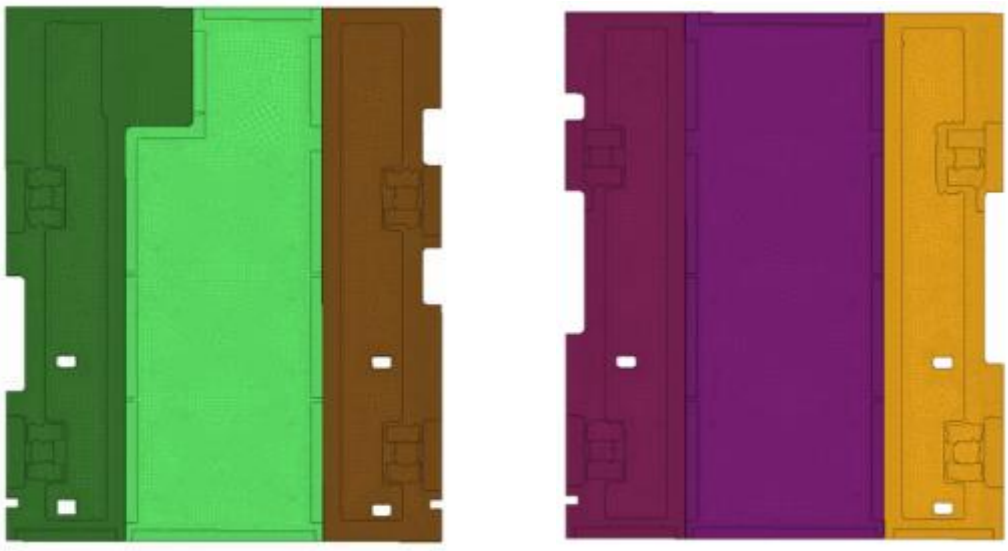

Figure 3.16. The FEM of West and East Communication Panels

Service Module consists of north, south, east, west service panels, and support panels. North and South panels have separate three panels because of equipment requirements, and they carry batteries of the satellite. East panels are three pieces, and west panels are four pieces. Support panels increase the north and south panels' out-of-plane stiffness since they carry the heaviest equipment, which is batteries. The general FEM of the service module is shown in Figure 3.17

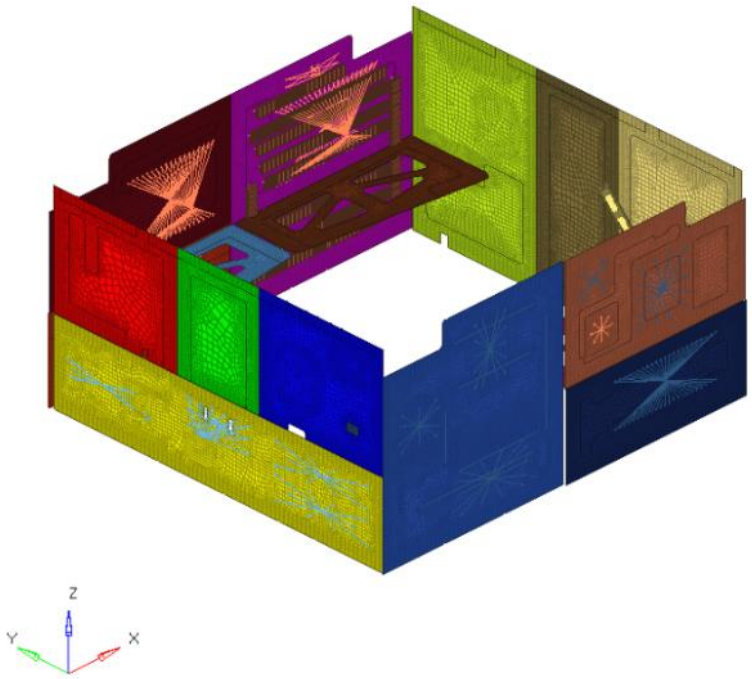

Figure 3.17. The FEM of Service Platform

North and south service panels are modeled with CQUAD4 and CTRIA3 elements. Batteries and altitude control subsystem equipment are mounted on these panels. External heat pipes are implemented to panels that have batteries. These external heat pipes are modeled with offset CBEAM elements. For equipment modeling, CONM2, RBE2, and CBUSH elements are used. Each panel has a different honeycomb thickness and density to increase bending stiffness. In addition, these

panels are aluminum sandwich panels. Properties of panels are modeled with a PCOMP card. Detailed FEM of north and south service panels are shown in Figure 3.18.

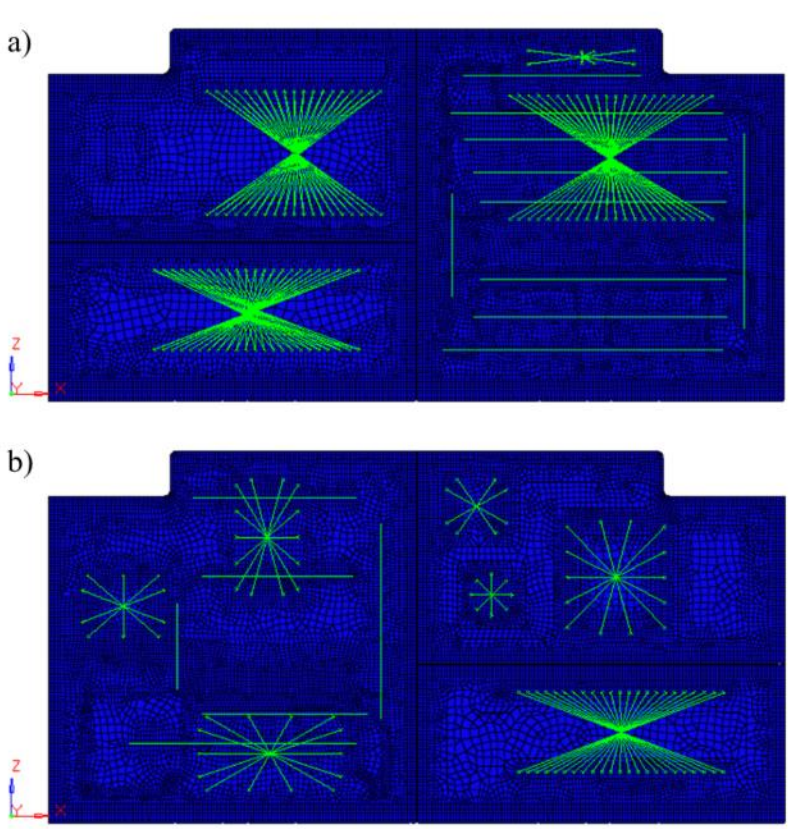

Figure 3.18. The FEM of (a) South and (b) North Service Panels

East and west service panels are modeled with CQUAD4 and CTRIA3 elements. The reflector deployment mechanism is attached to the base model and modeled as RBE2 and CBUSH elements. These panels are CFRP sandwich panels, and ply orientations and honeycomb thickness properties are included in the PCOMP card in MSC NASTRAN. The FEM of panels is shown in Figure 3.19.

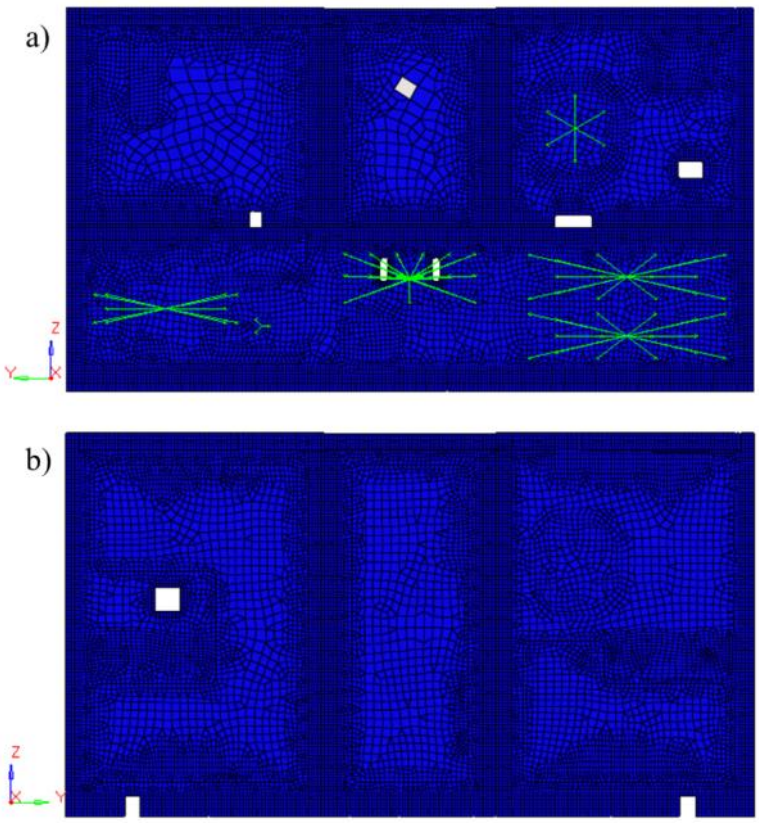

Figure 3.19. The FEM of (a) West and (b) East Service Panels

Solar arrays, the tower, and reflectors are modeled with CQUAD4, CTRIA3, CHEXA, and CTETRA elements. Materials of these structural parts are a combination of composite, aluminum, and sandwich panels. FEM of solar arrays, towers, and reflectors are given in Figure 3.20.

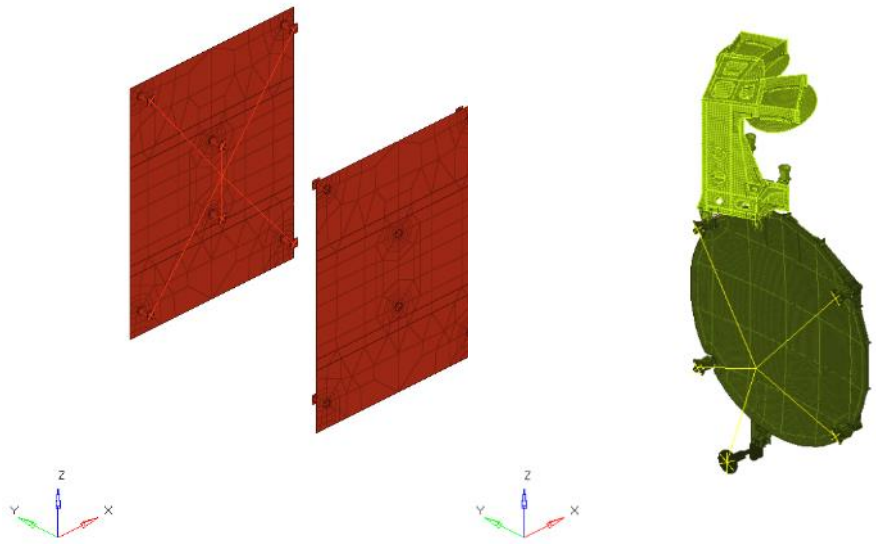

Figure 3.20. The FEM of Solar Arrays, Reflector, and Tower

Mechanical properties of metallic materials are given in Table 3.4. F_{tu} and F_{ty} are tensile ultimate and yield strength of the material. L and LT are the grain directions that describe the rolling direction of metal after being manufactured as a sheet. μ is the Poisons ratio. In addition, E and G represent Young's modulus and shear modulus of the material, respectively.

Table 3.4. Mechanical Properties of Metallic Materials

	F_{tu} [MPa]		F_{ty} [MPa]		*E* [GPa]	*G* [GPa]	μ	*Density* [kg/m3]
	L	**LT**	**L**	**LT**				
Aluminum 2024 T851	455.1	455.1	393.0	393.0	73.8	27.6	0.33	2768.0
Aluminum 7050 T7451	510.2	510.2	441.2	441.2	71.0	27.0	0.33	2823.4

Different cell sizes and densities of aluminum honeycombs are utilized in structural panels. Mechanical properties of honeycombs which are used in FEM are given in Table 3.5

Table 3.5. Mechanical Properties of Honeycombs [29]

Honeycomb Type	**Cell Size [mm]**	**Density [kg/m3]**	**L Direction Shear Modulus [GPa]**	**W Direction Shear Modulus [GPa]**
1/8-5056-.0007	3.2	50	0.34	0.16
	3.2	98	0.83	0.34
3/16-5056-.0007	4.8	32	0.23	0.12
	4.8	50	0.34	0.18

M18-55J is the used pre-preg type in CFRP panels, which consist of a high modulus fiber with high allowable tensile and compressive strength. Mechanical properties of carbon fibers are given in Table 3.6.

Table 3.6. Mechanical Properties of CFRP Laminate [30]

Property of M55J	**Value**
Tensile Strength	2020 MPa
Tensile Modulus	338 GPa
Compressive Strength	890 MPa
Flexural Strength	1180 MPa
Flexural Modulus	274 GPa

In FEM, each structural panel has a different thickness and skin material. Those properties are used in the PCOMP card in MSC Nastran. For aluminum sandwich panels, properties that are used in FEM are given in Table 3.7.

Table 3.7. Aluminum Sandwich Panel Properties

Panel Name	Skin Material	Honeycomb Type	Skin Thickness [mm]	Honeycomb Thickness [mm]	Total Panel Thickness [mm]
North and South Communication Panels	AL 7050 T7451	1/8-5056-.0007	0.53	24.52	25.59
North and South Battery Panels	AL 2024 T851	1/8-5056-.0007	0.66	58.47	59.80
South-East and South-West Service Panels	AL 2024 T851	1/8-5056-.0007	0.66	42.70	44.03
North-East and North-West Service Panels	AL 2024 T851	1/8-5056-.0007	0.66	24.50	25.82

For CFRP sandwich panels, properties that are used in FEM are given in Table 3.7.

Table 3.8. Composite Sandwich Panel Properties

Panel Name	Skin Material	Honeycomb Type	Ply Number and Orientation	Skin Thickness [mm]	Honeycomb Thickness [mm]	Total Panel Thickness [mm]
East and West Shear Panels	M18-55J	1/8-5056-.0007	16 Ply - 45°	1.76	26.52	30.04
North and South Shear Panels	M18-55J	1/8-5056-.0007	16 Ply - 45°	1.76	15.79	19.31
Service East and West Panels	M18-55J	3/16-5056-.0007	12 Ply - 30°	1.32	22.79	25.43
East and West Communication Corner Panels	M18-55J	3/16-5056-.0007	12 Ply - 30°	1.32	22.79	25.43
Service Support Panels	M18-55J	1/8-5056-.0007	12 Ply - 30°	1.32	15.79	18.43
East and West Communication Middle Panels	M18-55J	1/8-5056-.0007	6 Ply - 30°	0.66	22.55	23.87
Earth Deck	M18-55J	1/8-5056-.0007	12 Ply - 30°	1.32	58.47	61.11
Mid Deck	M18-55J	1/8-5056-.0007	12 Ply - 30°	1.32	28.28	30.92
Anti-Earth Deck	M18-55J	1/8-5056-.0007	12 Ply - 30°	1.32	28.28	30.92

3.4 Finite Element Model Checks

After completion of the finite element model generation, the validity of the model is checked. Validation of finite element models ensures that finite element models are generated accurately. Validation can be performed with the two methods.

- Computer-aided model checks
- Mathematical model checks

Computer-aided checks are completed by using Hypermesh commercial software. With the help of the software, element quality checks, normal checks, and material orientation checks are performed.

In element quality check, four geometrical parameters are checked for QUAD4 elements, which are interior angle, taper, skew, and warpage. For CTRIA3 elements, there are three geometrical parameters, which are interior angle and skewness. Interior angle check controls the interior angles of each element in specified tolerances. The taper test controls the geometrical deviation of quadrilateral elements from the rectangular shape. Skew test controls the distortion of the element by evaluating the angle between lines that join mid of the opposite sides. Warpage is the evaluation of element planarity intolerances. MSC-NASTRAN element quality tolerances are given in Table 3.9.

Table 3.9. MSC-NASTRAN Element Quality Tolerances[31]

Element Quality Checks	**Tolerances**
Taper Ratio	≤ 0.5
CQUAD4 Interior Angle	$\geq 30°$ and $\leq 150°$
CTRIA3 Interior Angle	$\leq 160°$
Warpage	≤ 0.05
CQUAD4 Skew Angle	$\geq 30°$
CTRIA3 Skew Angle	$\geq 10°$

Element normal check is another check which is performed after completing the finite element model. The main reason of the element normal check in this study is to define offsets and ply orientations of the skins correctly. In Figure 3.21, an example of normal checks is shown for service shear panels. Red and blue colors show the direction of the element normal. It is crucial to have the same direction on each side of the panels.

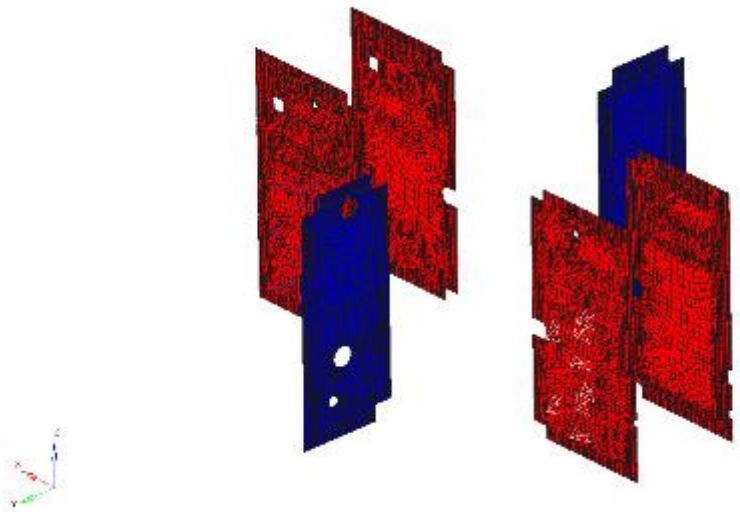

Figure 3.21. Element Normal Check Example

Material orientation check is another important criterion. Especially for composite modeling, the direction of material is critical to achieving the structure's accurate equivalent stiffness. CFRP plies and honeycombs have orthotropic material properties that have different properties in different directions. In order to get an accurate equivalent stiffness of sandwich panels, each layer orientation should be defined correctly. In the material orientation check, each ply orientation is controlled, which is given in Figure 3.22.

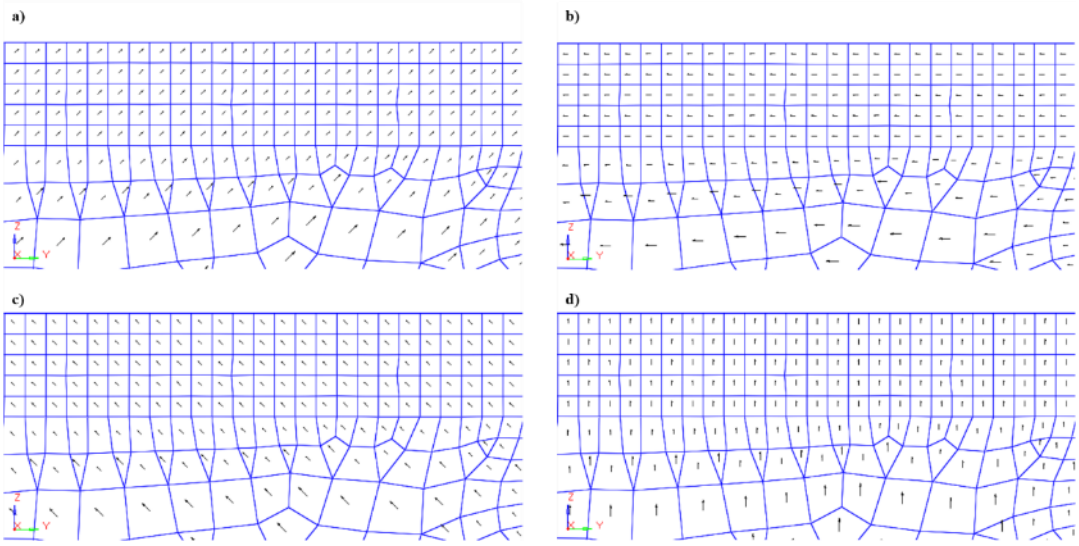

Figure 3.22. Ply Orientations of Shear Panels: (a) First Ply, (b) Second Ply, (c) Third Ply, and (d) Fourth Ply

Another crucial check is the mass and center of gravity (CoG) control. It is very critical to model structural design with accurate mass and CoG. A comparison between the structural model and FEM is given in Table 3.10. It is seen that the FEM of the satellite is representative in terms of mass and CoG.

Table 3.10. Mass and Center of Gravity (CoG) Comparison

Mass and Center of Gravity Comparison		
	Cad Model	**FEM**
Mass [kg]	3156.31	3156.46
CoG X [m]	0.0035	0.0052
CoG Y [m]	0.0031	0.0062
CoG Z [m]	1.2119	1.2069

Another finite element model validation method is mathematical validation. With respect to the purpose of the FEM generation, there are many methods. Unit enforced displacement and rotation check control boundary conditions in the model by applying unit displacement and rotation from the model's constraints. If the finite element model's purpose is to use for quasi-static analyses, unit gravity loading in all directions shall be performed. Reaction forces in constraints are controlled. Unit temperature increase check is applied to the finite element model when it is used for thermal distortion analyses. With the implementation of the same material properties in the model, there should be close to zero stress for iso-static boundary conditions.

In this study, free-free dynamics with stiffness equilibrium checks are implemented, and results are presented. In this check, the first six frequency of eigenvalue analysis should be close to zero, which are rigid body modes when the model is unconstrained. In addition, the stiffness matrix is checked that it does not have any grounding effect. [32] Strain energies are checked in order to verify the model not to include automatically or unintentionally created constraints. Any strain energy significantly higher than zero indicates that the parts of the FEM are not constrained correctly and/or are numerically unstable.

Rigid body mode calculations are performed with a normal mode solver (SOL 103) in MSC NASTRAN. For free-free dynamic checks, FEM is not constrained in the analysis. Strain Energies are lower than the limit, which is shown in Table 3.11.

Table 3.11. Strain Energy Check Results

Direction	**Strain Energy**	**Pass/Fail**
1	0.6445	Pass
2	0.5172	Pass
3	0.3110	Pass
4	0.7972	Pass
5	2.2927	Pass
6	0.1207	Pass
	LIMIT = 14.42	

The first six rigid body frequencies are close to zero, and the seventh frequency is higher than rigid body frequencies. These results show that there is no mechanism in the FEM, and the results satisfy the free-free dynamic checks shown in Table 3.12.

Table 3.12. Rigid Body Frequencies of FEM

Mode No	Frequency [Hz]
1	0.00213
2	0.00160
3	0.00145
4	0.00232
5	0.00343
6	0.00476
7	19.474

Rigid body mode shapes are demonstrated from Figure 3.23 to Figure 3.28. Translational X, Y, and Z mode shapes are given in Figure 3.23, Figure 3.24, and Figure 3.25. Rotational X, Y, and Z mode shapes are shown in Figure 3.26, Figure 3.27, and Figure 3.28

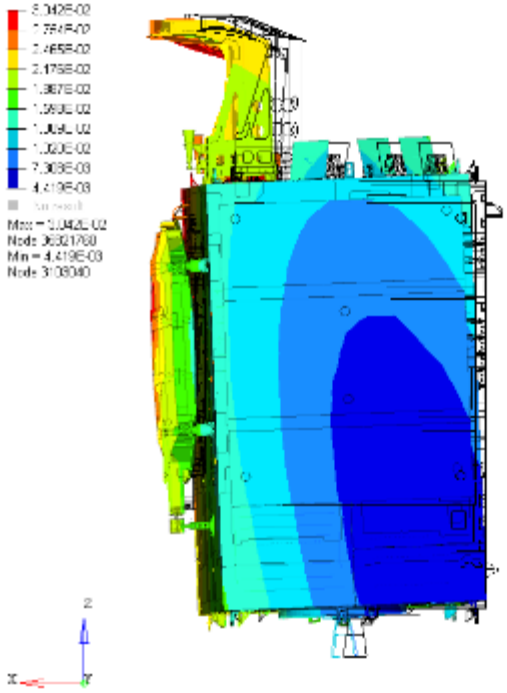

Figure 3.23. Free Boundary Condition Translational X Result

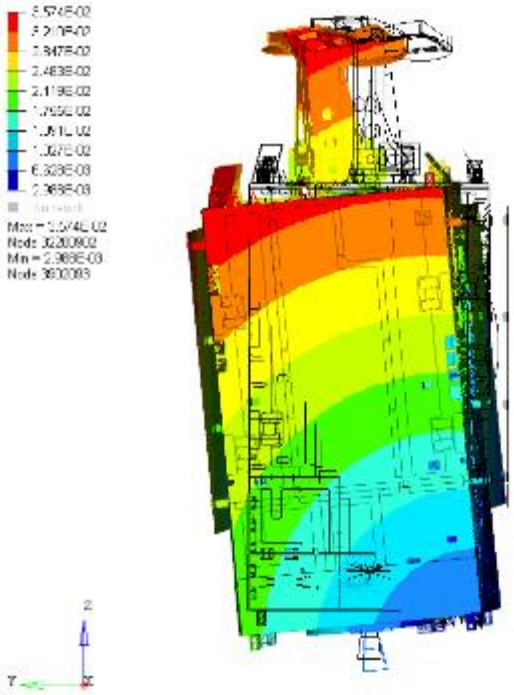

Figure 3.24. Free Boundary Condition Translational Y Result

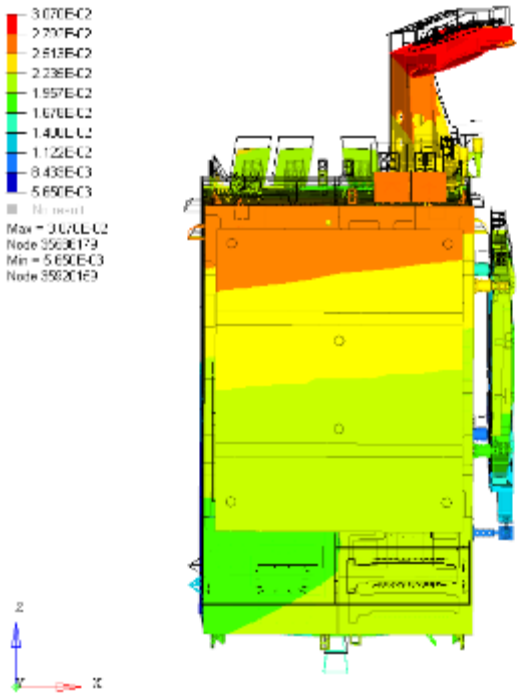

Figure 3.25. Free Boundary Condition Translational Z Result

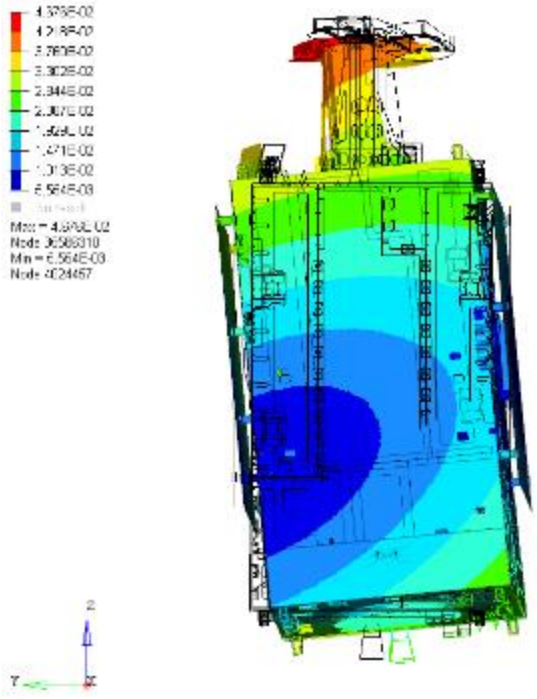

Figure 3.26. Free Boundary Condition Rotational X Result

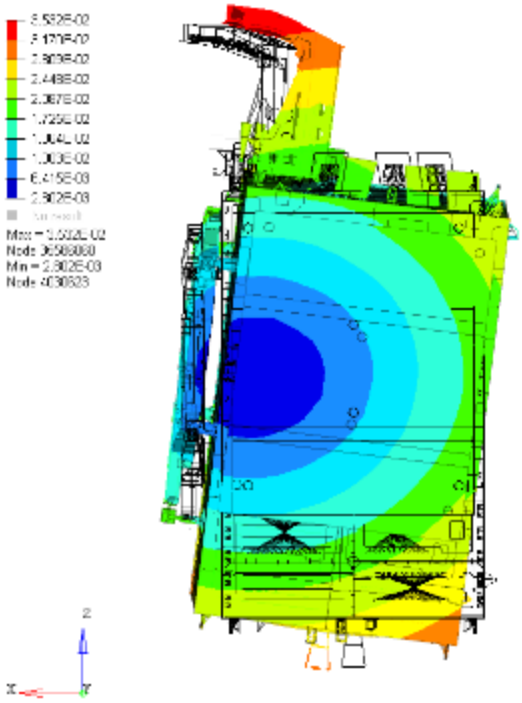

Figure 3.27. Free Boundary Condition Rotational Y Result

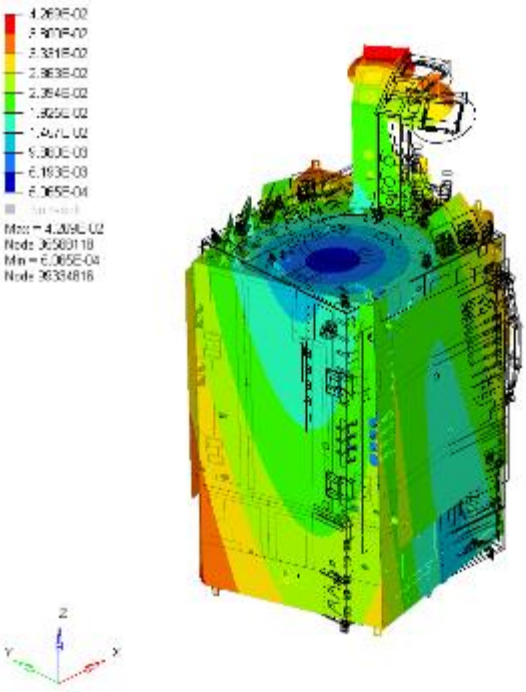

Figure 3.28. Free Boundary Condition Rotational Z Result

3.5 Conclusion

In this chapter, structural parts and panel naming are explained. General mass breakdown of the communication satellite is given to emphasize which subsystem is critical for design. For the satellites which use chemical propellants for maneuvering, propellant mass is %52.5 of the satellite mass. Hence two propellant tanks are located inside the main load-carrying member of the satellite. Structural panels and material properties are given with an explanation of their objective. Thermal dissipation is the main criteria of skin material selection with strength purposes as well.

Furthermore, the FEM of the communication satellite is briefly explained. Included subsystem details and simplifications are described for each structure part. Element types are given briefly. Panel properties and material properties that are used in the model are given. Finally, validation methods of the FEM are presented, which are computer-aided and mathematical checks. Results are demonstrated, which shows the finite element model's suitability for eigenvalue and frequency response analysis.

CHAPTER 4

SINE VIBRATION TEST RESULTS OF THE COMMUNICATION SATELLITE

4.1 Introduction

This section explains the conducted sine vibration test and the related results for the communication satellite. In the beginning, the test configuration and test system specifications are explained. Then the accelerometer type, which is used in the sine vibration test, is shown. The location of accelerometers on the satellites is also demonstrated. The sine vibration test steps with the results of the accelerometers are shown. Last but not least, the transfer function is briefly introduced, and the transfer functions of accelerometers are shown.

4.2 Sine Vibration Test Configuration

The sine vibration test starts with the definition of excitation at a specific frequency range, excitation direction, and accelerometer locations. After implementing the accelerometers, the satellite is mounted on a shaker via a slip table for lateral excitations and a head expander for axial excitations. Specification of the system is given in Table 4.1.

Table 4.1. Vibration Test System Specifications

Vibration Test System Specifications	
Maximum Load Capacity	8000kg
Maximum Force Capacity for Sine Vibration Test	289kN
Frequency Range	5-2000Hz

Before starting vibration tests, accelerometer names and directions are defined in the shaker's data acquisition system, and calibrations are performed.

4.3 Accelerometer Type, Locations, and Installations

Before the sine vibration test, accelerometers are mounted on the satellite in specific locations. 3-axis PCB-356A33 accelerometers are used in tests, which are shown in Figure 4.1. Accelerometer mounting starts with accelerometer selections. For accurate measurements, a smooth and flat surface should be prepared for attaching an accelerometer. At the contact surface, there should not be metal burrs or any other foreign objects.

With respect to mounting methods, the frequency response of the accelerometer should be investigated. There are four mounting methods available, which are stud, screw, adhesive and magnetic mounting.[33] Adhesive mounting is preferred since there are CFRP sandwich panels on satellites, and damage to the structure is avoided during tests.

Figure 4.1. Picture of PCB-356A33 Accelerometer [33]

Examples of mounted accelerometers on the reflector and earth deck of the satellite for the sine vibration tests are given in Figure 4.2.

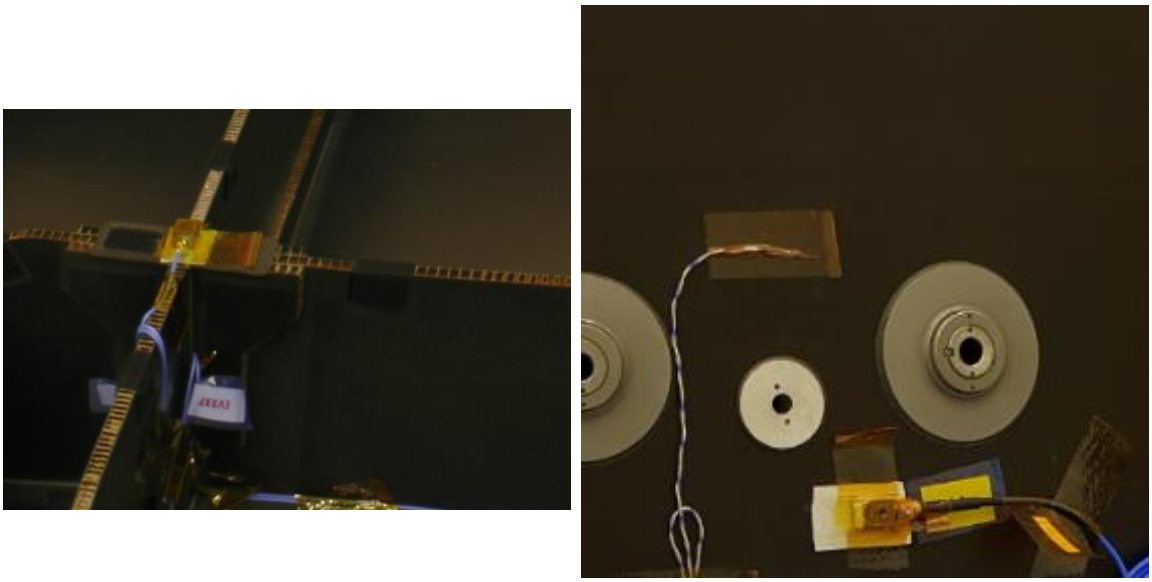

Figure 4.2. Example of Installed Accelerometers on the Satellite

Eleven accelerometers are implemented on the satellite. Three of them are on the primary structure of the satellite. Four of them are on the tanks. The remaining four are on reflectors.

The accelerometers on the primary structures are located on the earth deck and mid-deck. These locations are chosen to obtain results for X-direction sine vibration tests without any local mode. On the Earth deck, accelerometer locations are close to the central cylinder interface, which are not sensitive to the earth panel's local panel mode. Similarly, the accelerometer on the mid-deck is located interface with the east service shear panel. The accelerometer locations are demonstrated in Figure 4.3, namely accelerometer #1, #2, and #7.

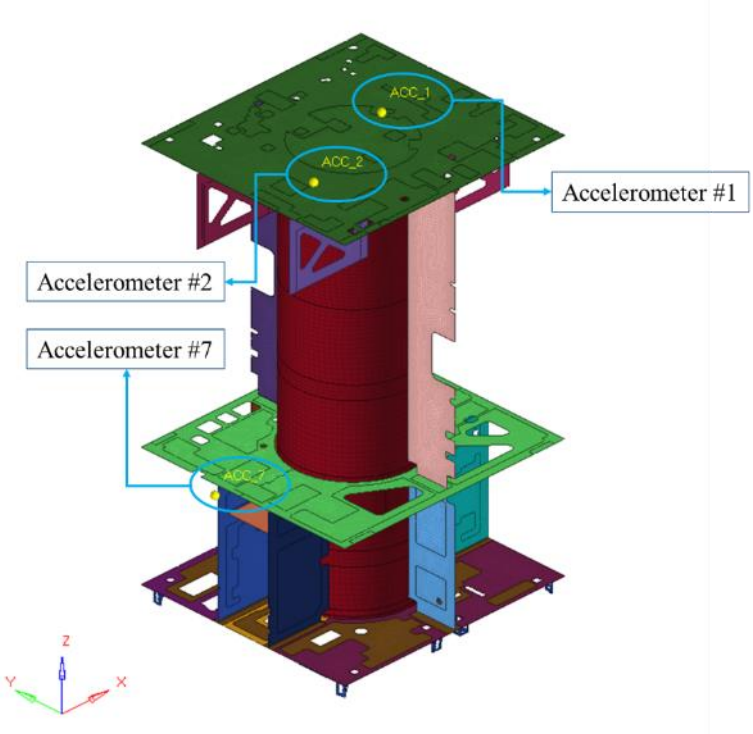

Figure 4.3. The Accelerometer Locations on Primary Structure

Half of the satellite mass belongs to chemical propellants, and two tanks carry these propellants on the satellite. In order to get the response of tanks in the sine vibration test, accelerometers are placed on the upper and lower part of the tanks. The accelerometer locations on the tanks are shown in Figure 4.4, namely accelerometer #3, #4, #5, and #6.

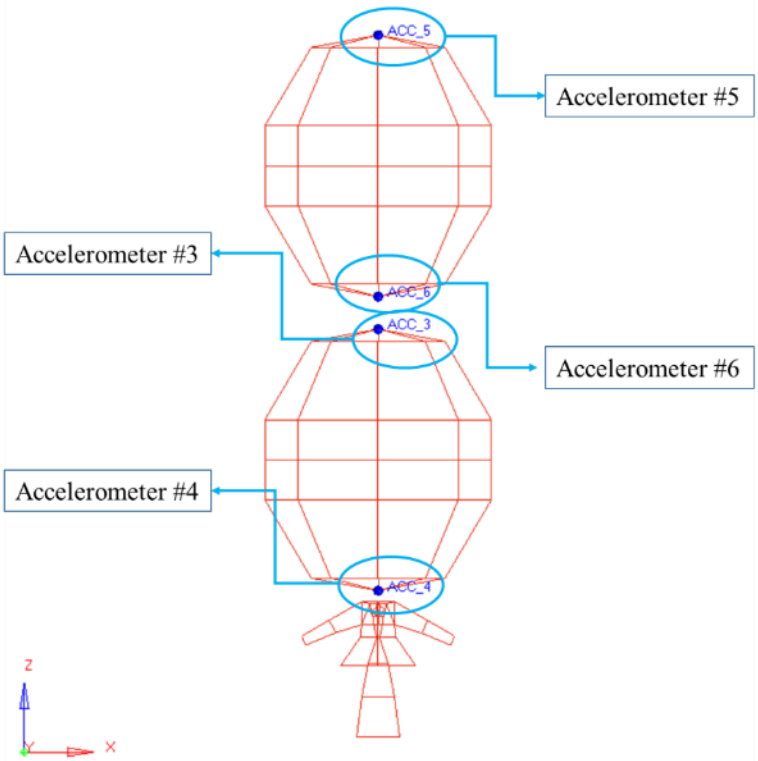

Figure 4.4. The Accelerometer Locations on Upper and Lower Tanks

The reflector is located at +X direction of the satellite, and in X direction sine vibration test, the response of the reflector is critical. Because of that, four accelerometers are mounted on the ribs of the reflector. In Figure 4.5, accelerometer locations on the reflector are shown.

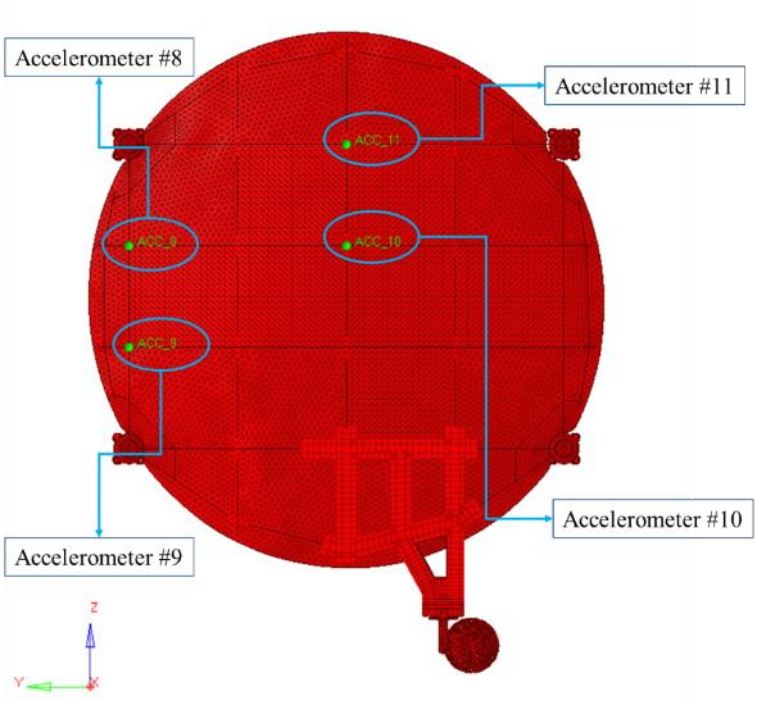

Figure 4.5. The Accelerometer Locations on Reflector

4.4 Sine Vibration Test Steps

During the launch of a typical communication satellite, sinusoidal vibrations up to 100Hz are usually generated by the launch vehicle. The launch vehicle induces these vibration loads to the satellite interface. Sine vibration tests are implemented on the communication satellite in order to simulate these vibration loads by changing the excitation frequencies in a sweep from a lower to an upper limit. The sine vibration tests are performed for lateral and axial directions of the satellite separately. At each test direction, steps that are shown in Figure 4.6 are implemented. The sine tests start with low-level base excitation, which is %5 of qualification excitation level. According to European Space Standardization requirements (ECSS)[13], low-level tests are conducted in order to identify resonance frequencies and verify the structural integrity after the full level run.

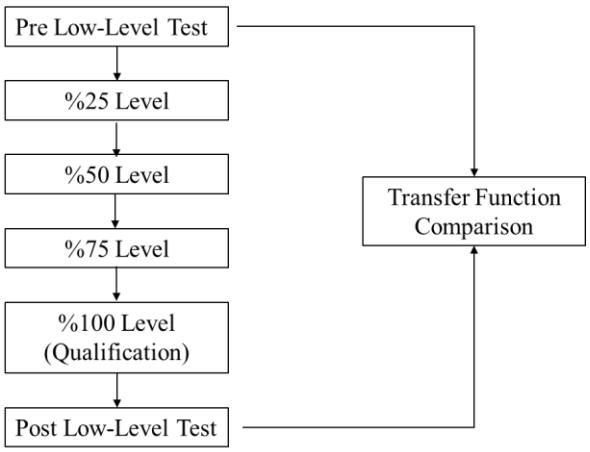

Figure 4.6. The Sine Vibration Test Steps

After low-level base excitation, 25%, 50%, 75% of the qualification level is applied in order. Finally, 100% of excitation is implemented on the structure. Base excitation of these steps is shown in Figure 4.7

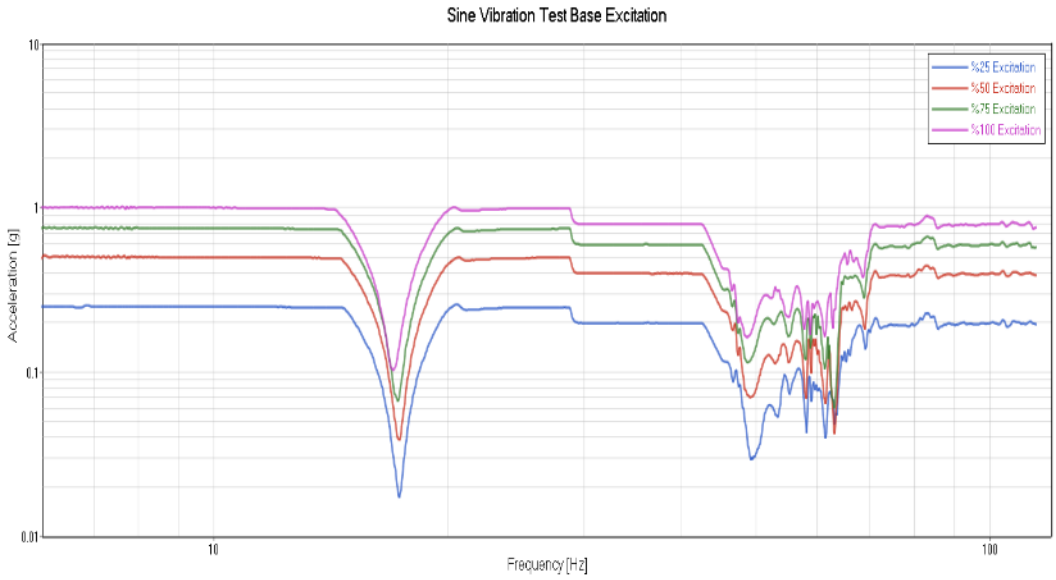

Figure 4.7. 25%, 50%, 75%, and 100% Base Excitation of the X-direction Sine Vibration Test

In order to observe structural unity, another low-level test is performed, and results are compared, which is shown in Figure 4.8. Comparison of pre-low-level and post-level transfer functions should be identical, and there should not be any frequency and amplitude differences in results. This comparison is assumed to show the verification of the structural unity after the qualification sine vibration test campaign.

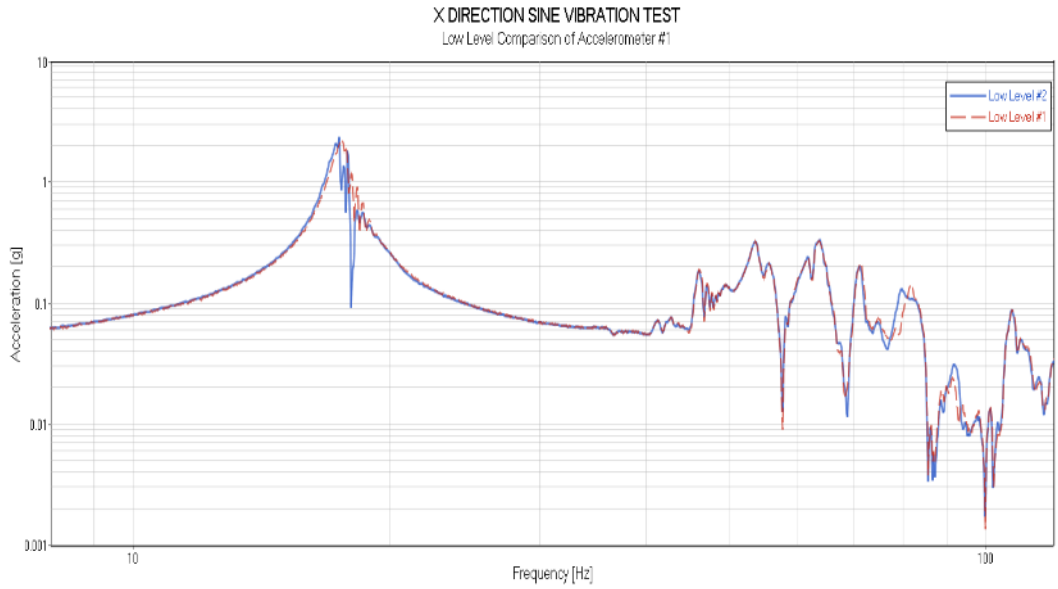

Figure 4.8. Low-Level Comparison of X-direction Sine Vibration Test

4.5 Sine Vibration Test Results

Base excitation and the response of the accelerometers, which are obtained in the x-direction sine vibration test, are shown in Figure 4.9, Figure 4.10, and Figure 4.11. Figure 4.9 shows the x-direction sine vibration test excitation level and the accelerometer responses on the primary structure. Figure 4.10 gives the acceleration levels that are obtained on the upper tank and lower tank accelerometers. The x-direction sine vibration response of the reflector accelerometers is shown in Figure 4.11.

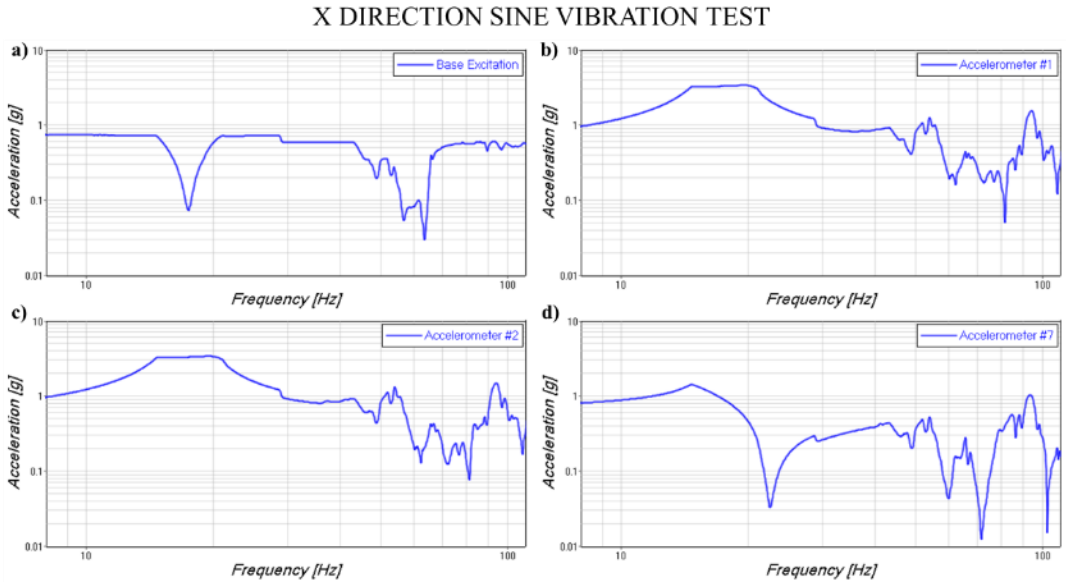

Figure 4.9. (a) Base Excitation, Response of Accelerometer (b) #1, (c) #2 and (d) #7

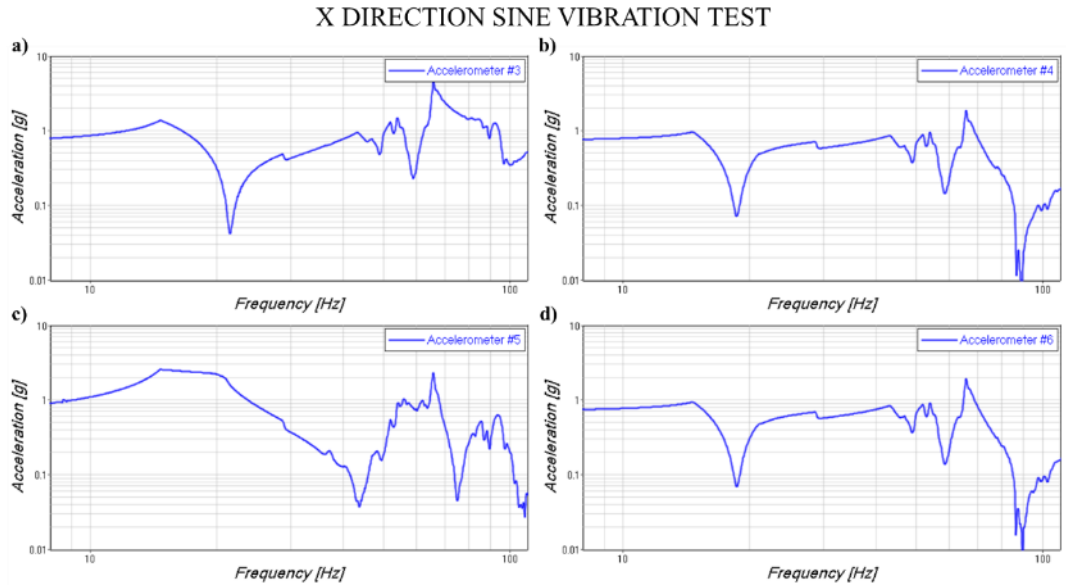

Figure 4.10. Response of Accelerometer (a) #3, (b) #4, (c) #5 and (d) #6

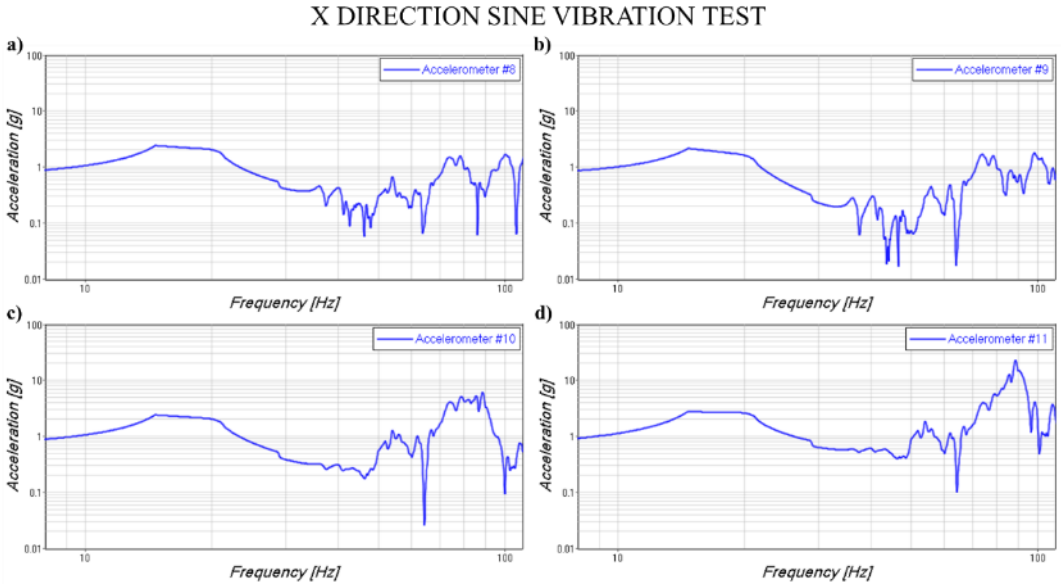

Figure 4.11. Response of Accelerometer (a) #8, (b) #9, (c) #10 and (d) #11

To compare accelerometer results at each step of the sine vibration test and to compare test and FEM results, the transfer functions are calculated for each accelerometer. Transfer function calculations are performed with the following equation:

$$\boldsymbol{Transfer\ Function} = \frac{\boldsymbol{Output\ of\ Accelerometer}}{\boldsymbol{Base\ Excitation}} \qquad \text{Eq. 8}$$

As a result, each accelerometer's transfer functions are generated, which are shown in Figure 4.12, Figure 4.13, and Figure 4.14. In Figure 4.12, the accelerometers' transfer functions on the primary structure show the satellite's bending mode, which is measured as 17.49Hz.

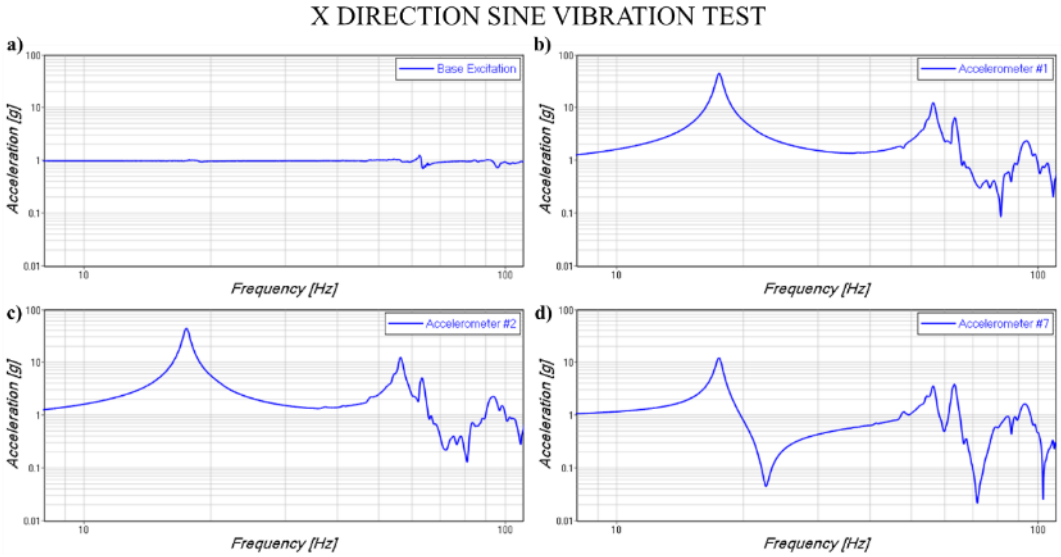

Figure 4.12. Transfer Function of (a) Base Excitation, (b) Accelerometer #1, (c) #2 and (d) #7

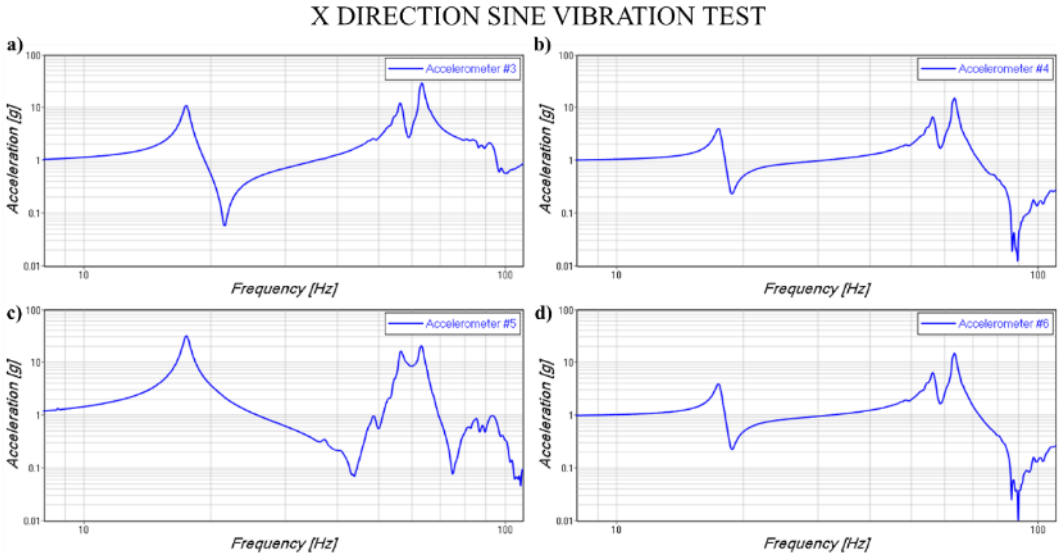

Figure 4.13. Transfer Function of Accelerometer (a) #3, (b) #4, (c) #5 and (d) #6

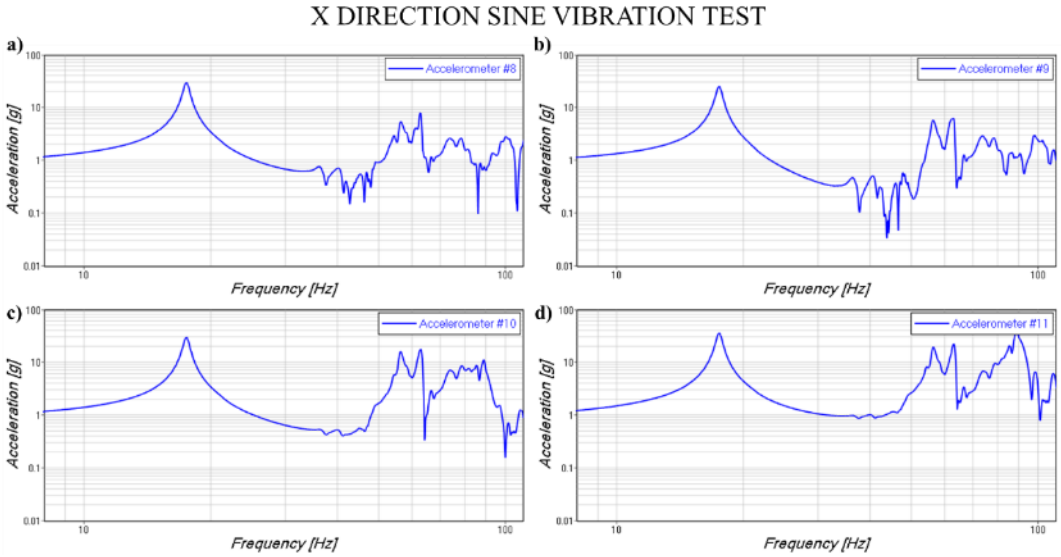

Figure 4.14.Transfer Function of Accelerometer (a) #8, (b) #9, (c) #10 and (d) #11

In Figure 4.13, the transfer functions of accelerometers on tanks are shown. It is seen that tanks bending modes' responses, which are 56.19Hz and 63.19Hz, are higher than the satellite's bending frequency. In Figure 4.14, transfer functions of accelerometers on the reflector are shown. The reflector's bending frequency, which is 88.86Hz, can be observed.

4.6 Conclusion

In this chapter, the sine vibration test configuration, accelerometer types utilized, and the accelerometer locations on satellite during the tests are explained in detail. The x-direction sine vibration accelerometer responses which are used in this study are shown. Finally, the transfer functions of the accelerometers, which are generated for comparison purposes with the numerically obtained results, are also given.

CHAPTER 5

COMPUTATIONAL FREQUENCY RESPONSE ANALYSIS OF THE COMMUNICATION SATELLITE

5.1 Introduction

In this chapter, eigenvalue, and frequency response analysis results are presented. Firstly, the eigenvalue analysis procedure and effective mass calculations are explained briefly. The boundary condition is demonstrated, and results with effective mass calculations and mode shapes are given. Then the frequency response analysis, damping values, and residual vectors are explained. The x-direction response of accelerometers in FEM as a result of x-direction unit excitations is given in graphs.

5.2 Effective Mass Results

The structural subsystem needs to be designed to achieve many requirements. One of the crucial requirements comes from launchers. Every launcher has its own frequency requirements and dynamic behavior. For instance, the Ariane-6 launcher vehicle has a requirement for satellites to have more than 6 Hz for the lateral frequency and 20 Hz for the axial frequency [14]. Every satellite should satisfy these requirements to be launched with launch vehicles. The structural design should consider these requirements while keeping structural mass as low as possible.

Eigenvalue analysis is one of the analyses that is performed for modal identification and design requirement checks. Since the FEM of the satellite is a large model, the LANCZOS method is used in normal mode analysis in MSC NASTRAN. With this solver, the equation of motion for natural frequencies is solved, which is given in Eq. 9, and eigenvalues are obtained. M and K are the mass and stiffness matrices, respectively. u and ü are displacement and acceleration values.

$$[\mathbf{M}]\{\ddot{\mathbf{u}}\} + [\mathbf{K}][\mathbf{u}] = \mathbf{0} \qquad \text{Eq. 9 [31]}$$

In the eigenvalue analysis, the boundary condition is modeled with RBE2 in the launch vehicle interface. The boundary conditions, which are constrained translational and rotational degrees of freedom, are shown in Figure 5.1.

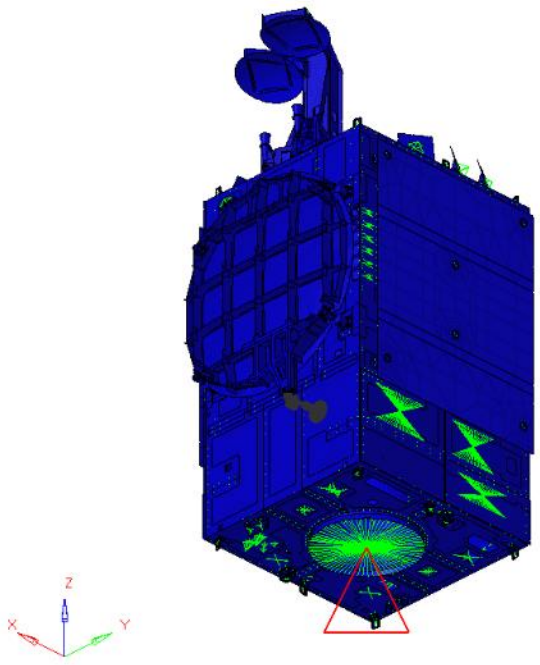

Figure 5.1. The Boundary Conditions of the FEM

Modal effective mass or modal participation factor is an essential tool to identify the structure's critical modes. In the effective mass calculations, the results show how much mass in each mode contributes to the total modal mass of a structure. Modes with high effective mass are excited with base excitation easily. On the other hand, with less effective mass, mode excitation is limited to the local area and should be evaluated in that direction. In MSC-NASTRAN, the modal effective mass is

calculated with the MEFFMASS case-control card in the SOL103 solver. The participation factor is calculated with Eq. 10 in MSC NASTRAN. In the equation, P is the participation factor, $\boldsymbol{\Phi}$ is the eigenvector, M is the mass matric, and $\boldsymbol{D_R}$ is the rigid-body vector in the associated direction.

$$\boldsymbol{P = \Phi^T M D_R} \qquad \text{Eq. 10 [31]}$$

As a result of normal mode analysis with effective mass calculation, frequencies, mode shapes, and participation factors are obtained. A total of 181 modes are calculated up to 110Hz. With the help of Excel, effective mass percentages of each mode are calculated. The effective mass percentage of each mode, which has greater than 5%, is given in Table 5.1.

Table 5.1. Effective Mass Results

Frequency [Hz]	**Effective Mass Percentage**						**Description**
	Tx [%]	**Ty [%]**	**Tz [%]**	**Rx [%]**	**Ry [%]**	**Rz [%]**	
16.95	45.1	3.6	0.0	6.9	82.2	0.0	Global X Bending Mode
17.02	3.8	43.8	0.0	82.2	6.8	0.0	Global Y Bending Mode
31.85	0.0	0.0	0.0	0.0	0.0	63.9	Global Torsional Mode
38.45	0.1	0.0	0.0	0.0	0.1	7.2	Torsional Modes
42.33	0.1	0.0	0.0	0.0	0.0	9.1	
48.26	6.5	6.7	0.0	0.2	0.5	0.2	Tank Asymmetric Bending Mode
54.97	10.1	0.3	0.0	0.0	0.5	0.0	Tank X Bending Mode
55.52	0.0	5.1	0.0	0.2	0.0	0.1	Tank Y Bending Mode
62.39	0.2	0.0	11.1	0.0	0.0	0.0	
63.89	0.0	0.0	22.1	0.0	0.0	0.0	Tank and Structure Axial Modes
64.41	0.0	0.0	8.5	0.0	0.0	0.0	
66.47	0.1	0.2	24.0	0.0	0.0	0.0	
66.91	0.1	0.3	13.9	0.0	0.0	0.0	
77.33	3.2	0.1	0.0	0.0	0.0	0.8	Reflector Bending Mode

The primary bending frequencies of the satellite in X and Y directions are 16.95Hz and 17.02Hz, respectively. In x bending frequency of the satellite, 45.1% of the satellite mass moves in translational-x and 82.2% moves in rotational-y while in y bending frequency of the satellite, 43.8% of the satellite mass move in translational-y, and %82.2 moves in rotational-x. The mode shapes of the primary bending modes are shown in Figure 5.2 and Figure 5.3.

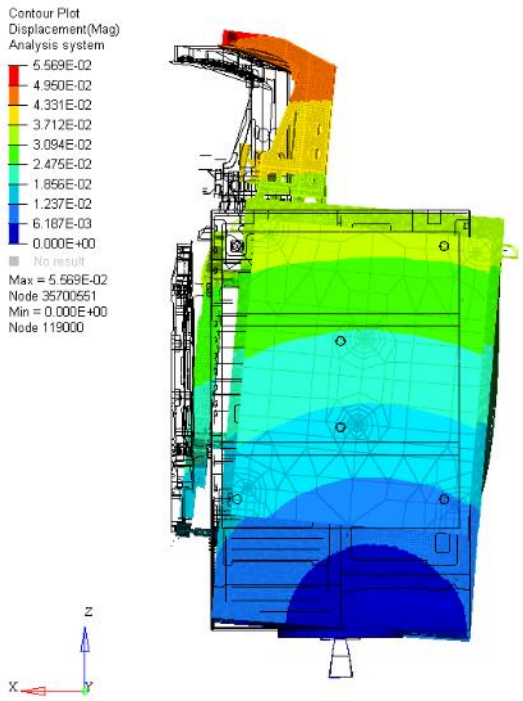

Figure 5.2. Global X Wise Bending Mode of the Satellite

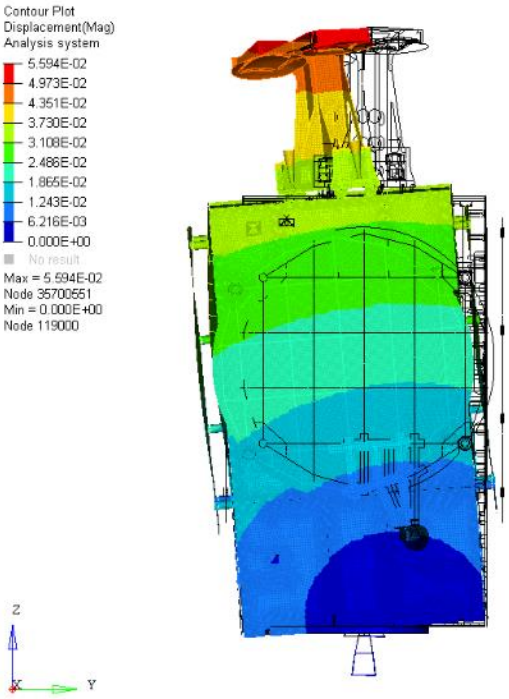

Figure 5.3. Global Y Wise Bending Mode of the Satellite

The satellite's main torsional mode is 31.85Hz, and it has an effective mass of 63.9%. The main torsional mode of the satellite is shown in Figure 5.4. x-direction tank bending mode is 54.97Hz, and it has an effective mass of 10.1%. In order to demonstrate tank bending mode clearly, only the primary structures and tanks are shown in Figure 5.5

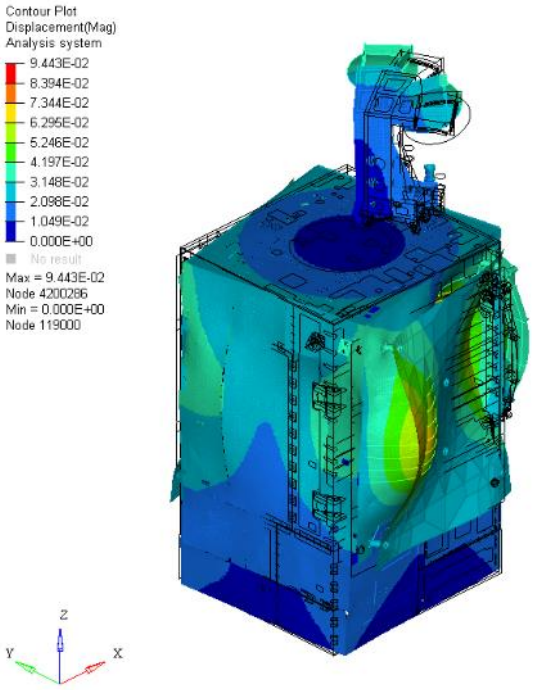

Figure 5.4. Global Torsional Mode of the Satellite

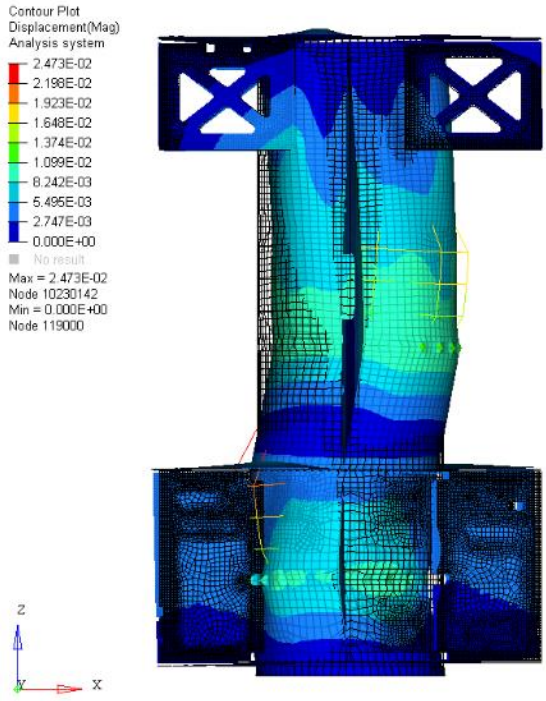

Figure 5.5. Tank X Wise Bending Mode of the Satellite

The eigenvalue analysis is performed at a supercomputer with 24 CPUs. CPU time and properties of platforms are given in Table 5.2. The normal mode analysis is completed in 21 minutes with 24 CPUs.

Table 5.2. CPU Time and Platform Properties for Eigenvalue Analysis

Platform Properties	
CPU	Intel
Clock Frequency	2500 MHz
Number of CPUs	24
RAM	257701 MB
Total CPU Time	30265 Sec

5.3 Frequency Response Analysis Results

Another crucial analysis is the frequency response analysis. Frequency response analysis is performed during structural subsystem design iterations for the following reasons:

- To simulate the dynamic environment specified by the launch vehicle and simulate the sine vibration tests after the design.
- To check the strength of structural panels, interfaces, and appendages.
- To check equipment qualification accelerations.

In this study, the simulation of the sine vibration test in the x-direction is considered. Frequency response analysis is performed with unit acceleration excitation to get transfer function at specific nodes. In MSC-NASTRAN, Solver 111 is used as a solver for modal frequency response analysis. The modal frequency response method uses mode shapes of the structure to reduce the size and perform a more efficient numerical solution for large models.[31]

In frequency response analysis, the response of the satellite is required up to 110Hz. In order to get accurate responses up to 110Hz, the normal mode solution is extended

to 220Hz in frequency response analysis. In the analysis, structural damping is included as 2% percent. The use of residual modes is implemented to obtain more accurate results, including the RESVEC case-control card in MSC-NASTRAN [34]. In addition, since solar arrays and reflectors of the satellite have a flexible structure, the air effect is included in the solution as an industrial practice. In MSC-NASTRAN, the MFLUID card is used in the solver deck. Virtual mass matrix is generated in solution, representing the air-coupled to surface elements of the reflector and solar arrays [34]. The unit acceleration is given as base excitation to the satellite, shown in Figure 5.6 (a).

Transfer functions of nodes that represent base excitation and accelerometers are given from Figure 5.6 to Figure 5.8. In Figure 5.6, the base excitation and transfer functions of accelerometers on the primary structure are given. In Figure 5.7, the results of upper and lower tank accelerometers are presented. Figure 5.8, results of accelerometers on reflectors are presented.

In Figure 5.6, transfer functions of the accelerometers' locations on the satellite's primary structure are given. It is seen that the x-direction bending mode of the satellite is calculated as 16.95Hz. Transfer functions of the points, which are the tanks accelerometers' locations, are given in Figure 5.7. 48.26Hz and 54.97Hz can be seen in graphs, which are tanks’ bending modes. In Figure 5.8, the transfer function calculations of the reflector accelerometer locations are given. The bending mode of the reflector, which is 77.33Hz, can be observed in graphs.

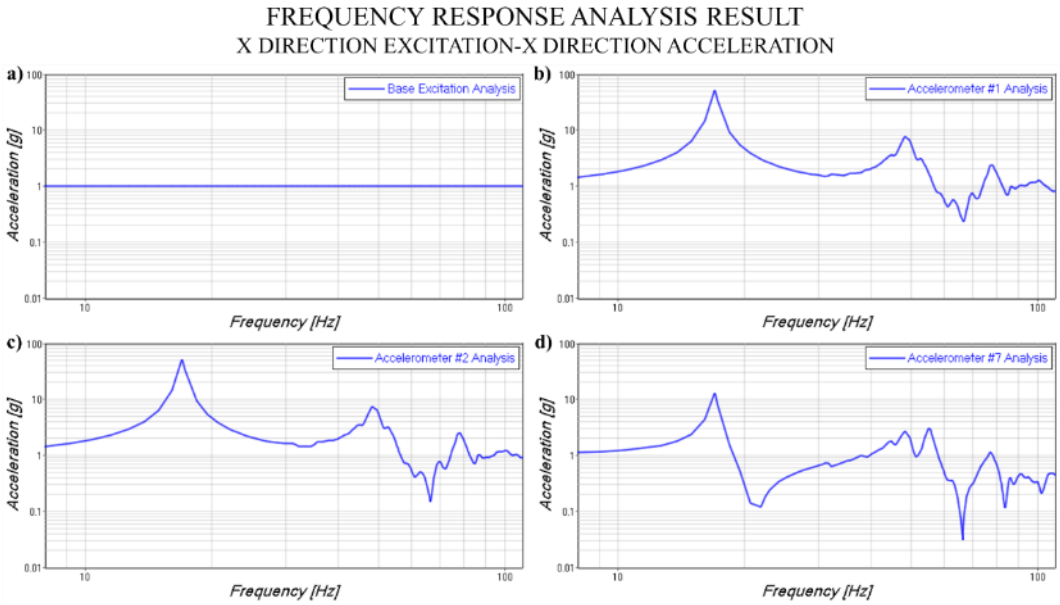

Figure 5.6. Frequency Response Analysis Transfer Function Result of (a) Base Excitation, Accelerometer (b) #1, (c) #2 and (d) #7

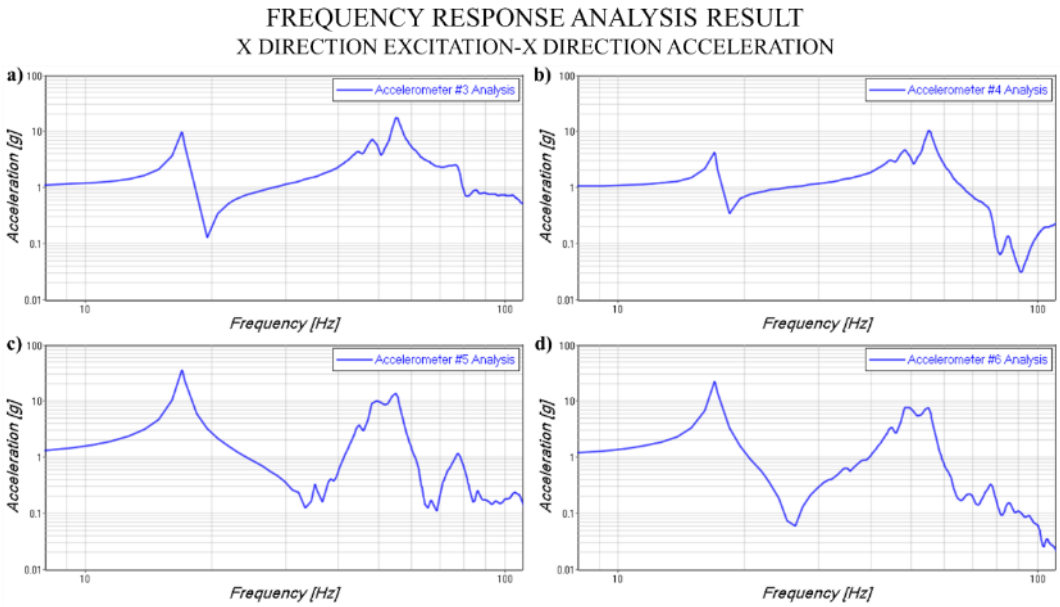

Figure 5.7. Frequency Response Analysis Transfer Function Result of Accelerometer (a) #3, (b) #4, (c) #5 and (d) #6

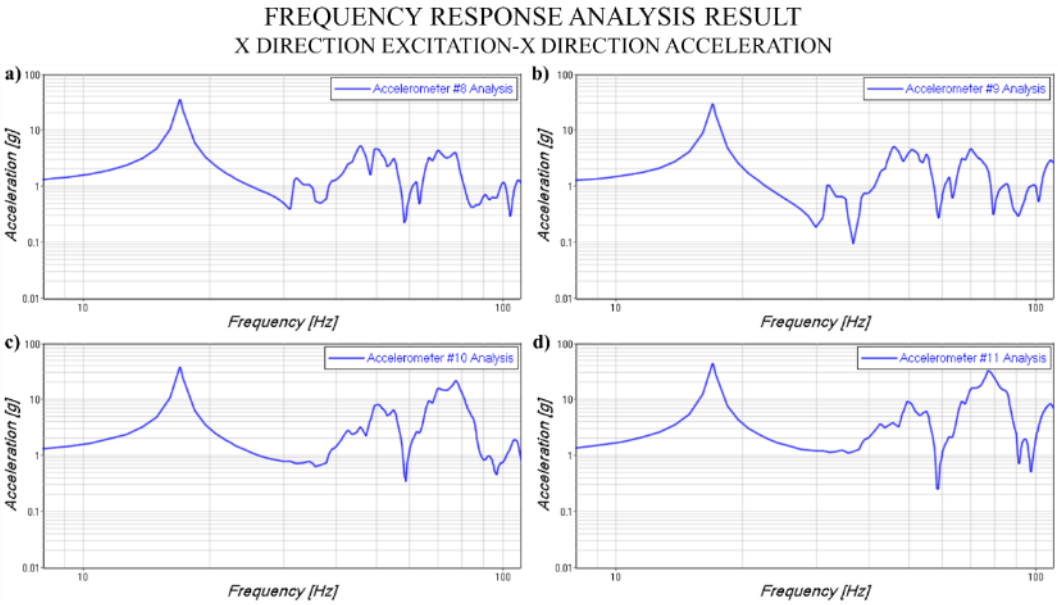

Figure 5.8. Frequency Response Analysis Transfer Function Result of Accelerometer (a) #8, (b) #9, (c) #10 and (d) #11

Frequency response analysis is performed at a supercomputer with 24 CPUs. CPU time and properties of platforms are given in Table 5.3. Frequency response analysis is completed in 39.2 minutes with 24 CPUs.

Table 5.3. CPU time and Platform Properties for Frequency Response Analysis

Platform Properties	
CPU	Intel
Clock Frequency	2500 MHz
Number of CPUs	24
RAM	257701 MB
Total CPU Time	56456 Sec

5.4 Conclusion

In this chapter, the eigenvalue analysis and effective mass calculations are outlined in detail. The usage of effective mass or participation factors in complex finite element models is an efficient method in order to identify the major structural modes. The normal mode and effective mass calculations are performed with an MSC-NASTRAN solver. In the satellite, there are 118 modes up to 110Hz. Most critical modes with more than 5% effective mass are shown, and the major mode shapes are demonstrated.

Frequency response analysis is also explained in this chapter. In the analysis, the structural modes, which are up to 220Hz, are extracted, the residual vectors and the effect of air are also included in order to increase the accuracy. The acceleration responses are given in specific nodes, which represent accelerometers on the satellite. The frequency response analysis is performed by using MSC-NASTRAN sol111 solver.

CHAPTER 6

FINITE ELEMENT MODEL IMPROVEMENT BY USING THE SINE VIBRATION TEST RESULTS

6.1 Introduction

In this chapter, first, the frequency response analysis results and the x-direction sine vibration test results are compared. For each frequency that is in interest, the accelerometers are chosen, and the frequency range details are demonstrated.

Frequency response assurance criteria are studied in order to show the similarities of the two datasets. Post-processing of the results is explained, and the mode pairing results are checked with assurance criteria.

The error localization is another crucial step in updating the finite element model. The Strain energy density plots are presented for each frequency in order to specify the modification regions in the FEM.

Finally, FEM iterations are performed by using the results of the error localization. All the iterations and improvements for interested frequencies are presented.

6.2 Test and Analysis Comparison

By using the results of the frequency response analyses and x-direction sine vibration tests, the transfer functions of the test and analysis are compared at each accelerometer location. For primary structure, a comparison of the results is given in Figure 6.1, Figure 6.2, and Figure 6.3. The location of the accelerometers is explained in Section 4.3.

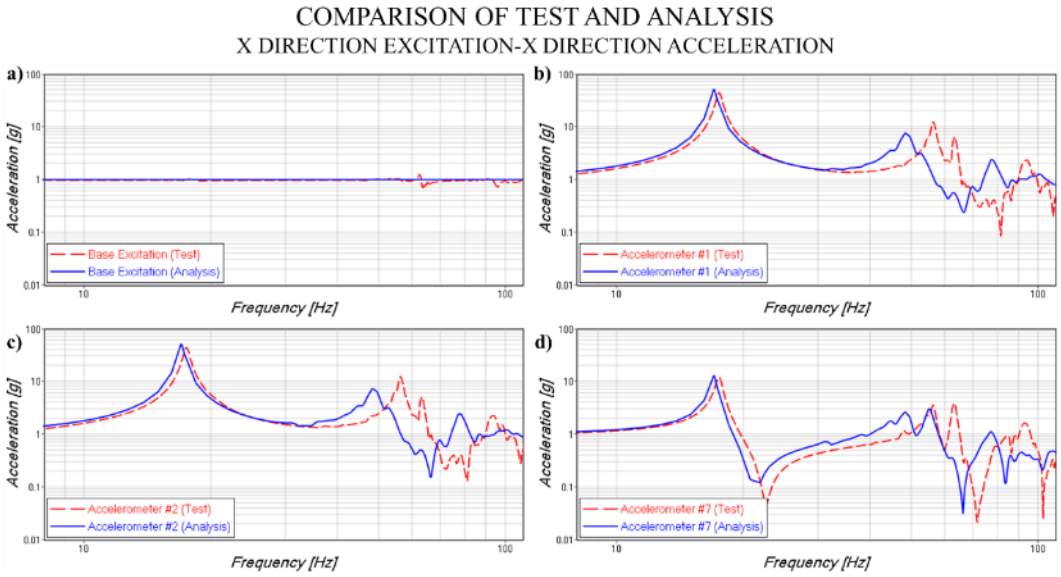

Figure 6.1. Test and Analysis Transfer Function Comparison of (a) Base Excitation, Accelerometer (b) #1, (c) #2 and (d) #7

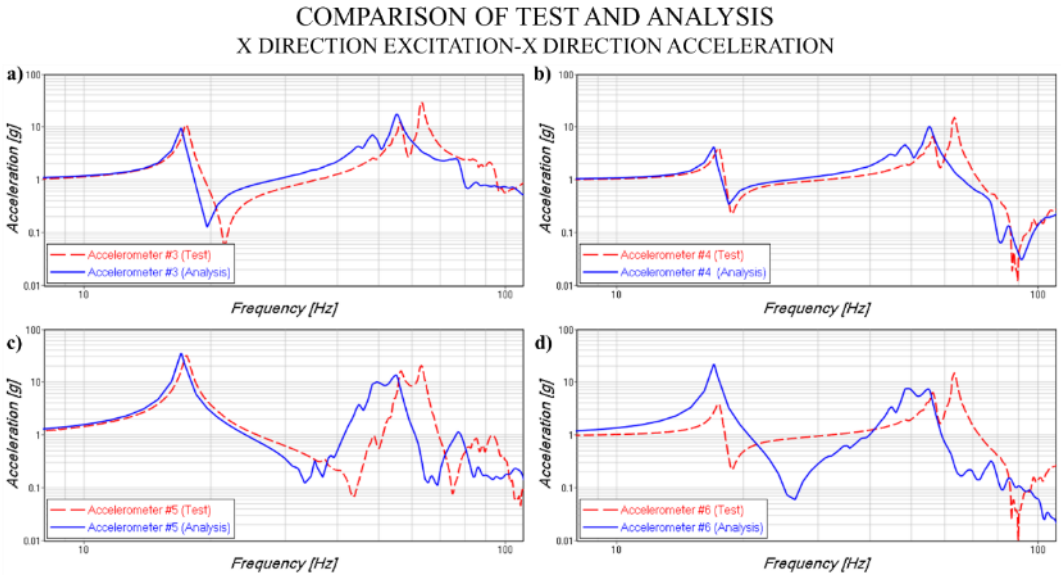

Figure 6.2. Test and Analysis Transfer Function Comparison of Accelerometer (a) #3, (b) #4, (c) #5 and (d) #6

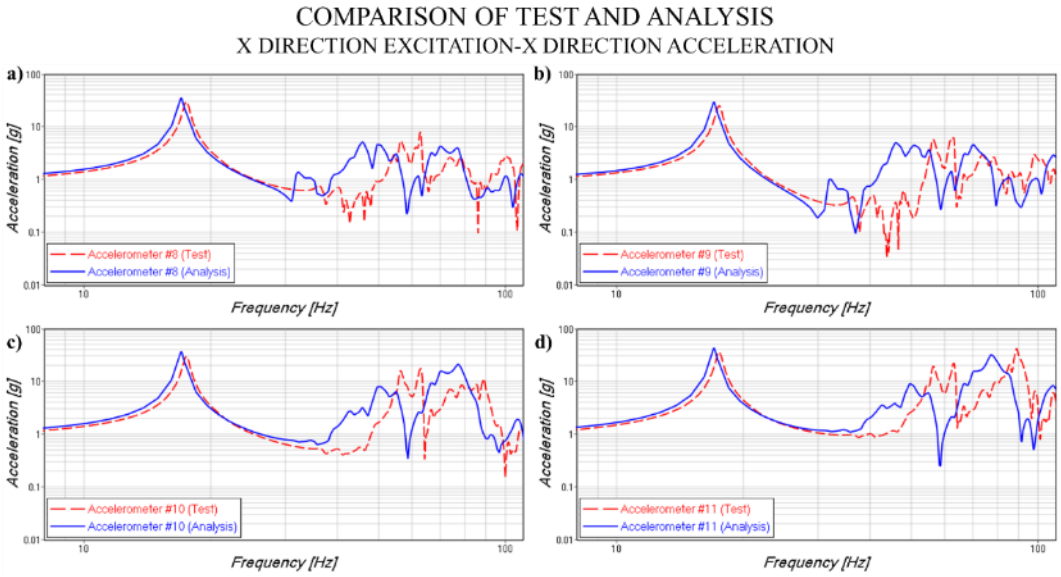

Figure 6.3. Test and Analysis Transfer Function Comparison of Accelerometer (a) #8, (b) #9, (c) #10 and (d) #11

One of the modes in the x-direction is the first bending mode of the satellite. The structure's behavior at 16.95Hz is clearly observed at every accelerometer on satellite; although the analysis results slightly underestimate this resonance frequency. Figure 6.4 shows the sine vibration test, and analysis results are detailed by zooming the frequency range in interest. This also highlights the difference in the compared resonance. In the analysis, the calculated frequency is 16.95Hz, while in the test, it is measured as 17.49Hz. Since this resonance frequency is the satellite's bending mode, this difference shows that the satellite's theoretical stiffness close to the boundary condition is lower than the real case.

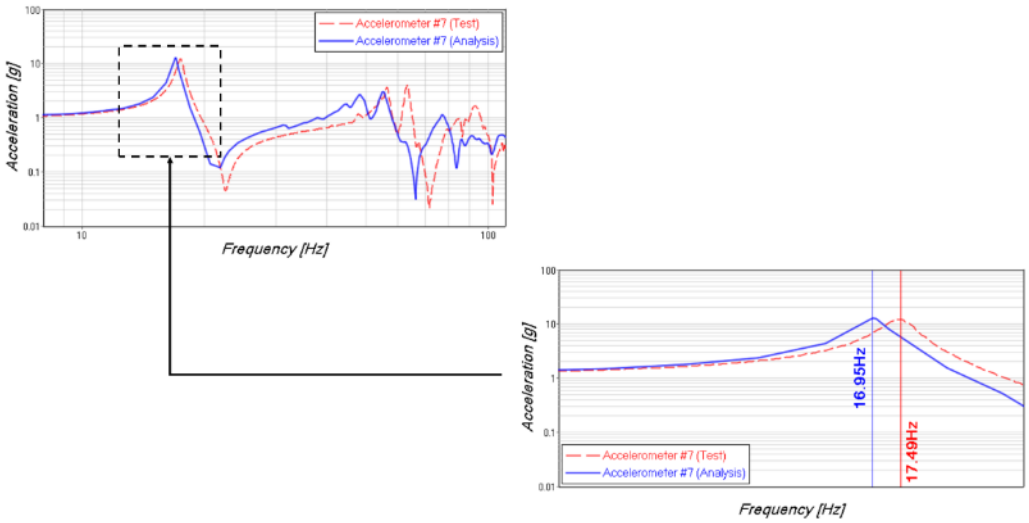

Figure 6.4. Detailed View of Satellite X-direction Bending Mode Response of Test and Analysis

Other prominent modes in the x-direction are the tank bending modes. At 48.26Hz and 54.97Hz, there are asymmetric bending modes and the x-direction bending mode of the tanks. These modes are similar in amplitude and frequency of test results, which are obtained at 56.19Hz and 63.19Hz in the x-direction sine vibration test. A comparison of these frequencies is given in Figure 6.5 by zooming the frequency range in interest.

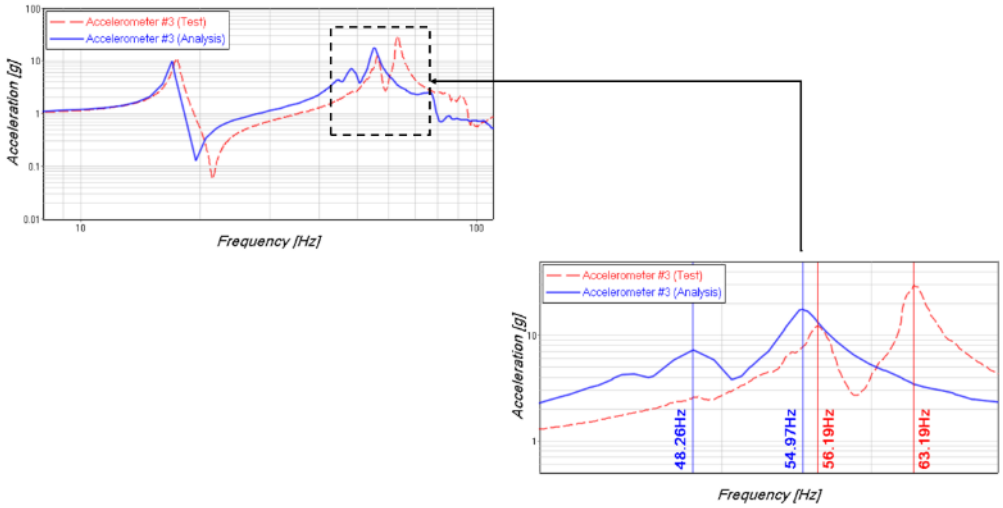

Figure 6.5. Detailed View of Tanks' Bending Mode Responses of Test and Analysis

The last important mode considered in the x-direction is the reflector bending mode. In the analysis, it is calculated as 77.33Hz, and it is observed as 88.86Hz in the test. The details of the comparison are given in Figure 6.6.

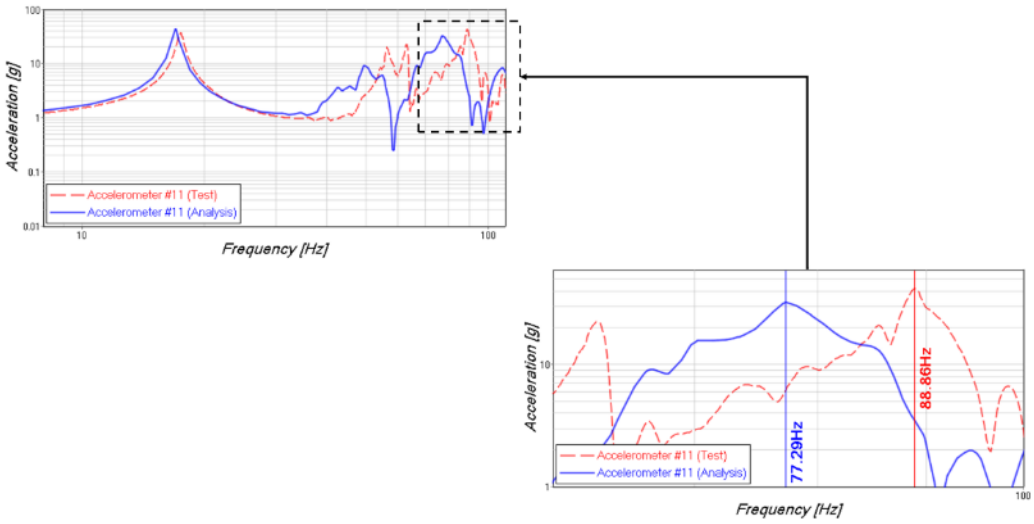

Figure 6.6. Detailed View of Reflector Bending Mode Response of Test and Analysis

There is a 3.19% difference between test and analysis for the first frequency, the satellite's fundamental x-direction bending mode. There are 16.43% and 14.95% of differences in bending modes of the tanks. For the reflector's bending mode, there is a %14.91 difference. A comparison of the frequencies is given in Table 6.1.

Table 6.1. Frequency Comparison of Test and Analysis

Mode Description	**Analysis [Hz]**	**Test [Hz]**	**Percentage Wrt Test [%]**
X-direction First Bending of the Satellite	16.95	17.49	-3.19%
Asymmetric Bending Mode of the Tanks	48.26	56.19	-16.43%
X-direction Bending Mode of the Tanks	54.97	63.19	-14.95%
Bending Mode of the Reflector	77.33	88.86	-14.91%

Table 6.1 shows that numerically calculated frequency values are lower than the sine vibration test results. With the assumption of the mass and the dimensions of the satellite components are not changing, the satellite's stiffness, which is modeled in the FEM, is lower than the actual satellite. For the first bending mode of the satellite in the x-direction, the stiffness of the regions close to the boundary conditions is expected to be lower than the satellite. For second and third frequencies, which are the tanks' bending modes, there may be variation in tank stiffness and interface stiffness in the FEM. For the last mode, the reflector bending mode, reflector stiffness, and interface between satellites should be investigated.

6.3 Modal Assurance Criteria of the Test and Analysis Results

For the modal assurance criteria (MAC) of the x-direction sine vibration test results and the analysis results, four natural frequencies with the most effective mass percentage on x-direction are selected. These frequencies are 16.95Hz, 48.26Hz, 54.97Hz, and 77.33Hz. A total of eleven accelerometers are used for calculating the modal assurance criteria values. In order to increase the robustness for the assurance criteria matrices calculations, a FORTRAN script is written. In this script, the frequency response analysis results and test data are used as input, and output is given as MAC matrices. Frequency response analysis output is requested as a punch

file, which is formatted data of acceleration response in MSC-NASTRAN. Test data is used as universal test output data. The diagram of the program is given in Figure 6.7.

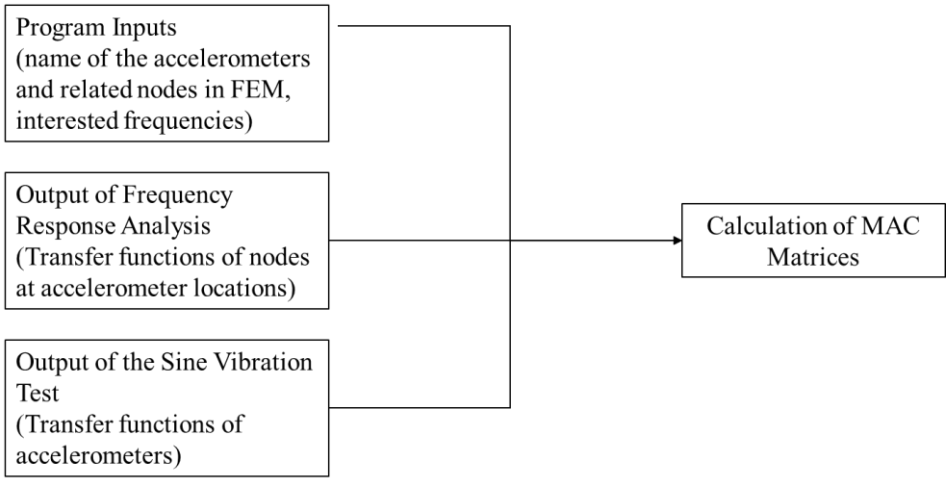

Figure 6.7. Diagram of the Developed FORTRAN Script for MAC Calculations

By using the specified frequencies, the MAC results of the test and analysis are calculated. These results show the eigenvectors of test and analysis similarity. Calculated MAC values and their graph are given in Table 6.2 and Figure 6.8, respectively. The results show that the four frequencies are similar. For the x-direction bending mode, which is measured as 17.49Hz, the diagonal MAC value is 0.960. For the asymmetric bending mode and the x-direction bending mode of the tanks, which have frequencies of 56.19Hz and 63.19Hz in the test, it has diagonal MAC values of 0.790 and 0.901, respectively. Finally, for the reflector's bending mode, which is 88.86Hz, the MAC value is 0.920.

Table 6.2. The Modal Assurance Criteria Between Test and Analysis Results

Frequency [Hz]		**Test**			
		17.49	56.19	63.19	88.86
Analysis	16.95	0.960	0.291	0.008	0.019
	48.26	0.034	0.790	0.035	0.105
	54.97	0.023	0.029	0.901	0.074
	77.33	0.165	0.258	0.001	0.920

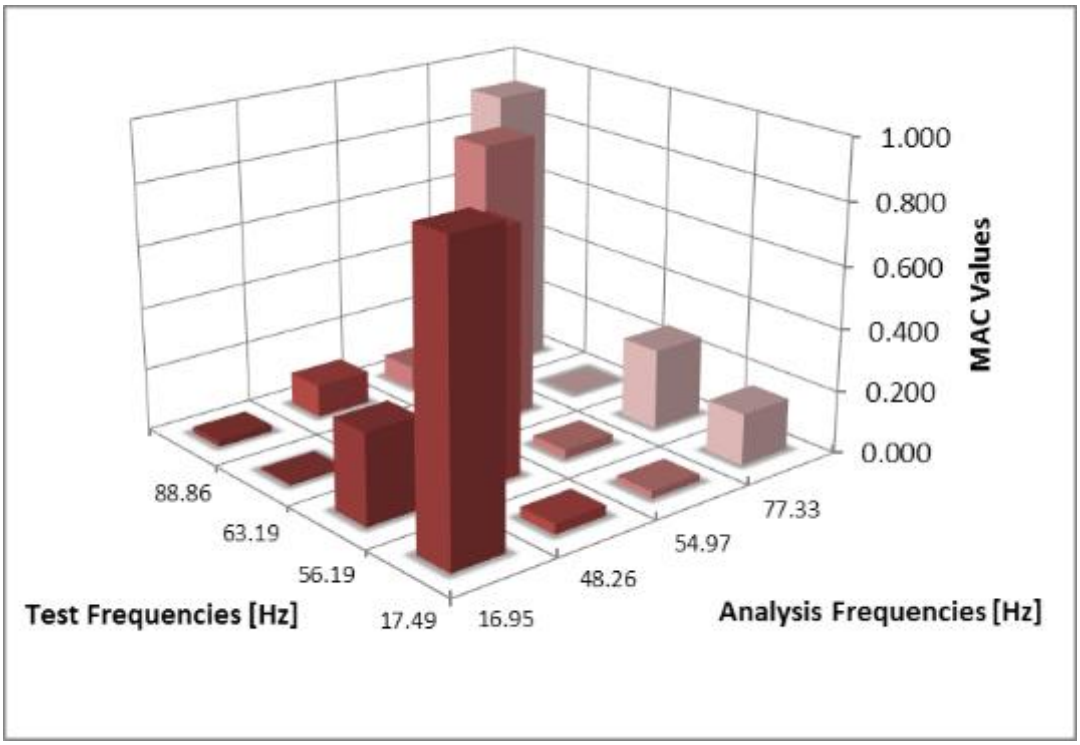

Figure 6.8. The Modal Assurance Criteria Between Test and Analysis Results

6.4 Error Localization of the FEM

Element strain energy is an efficient tool to determine the potential elements to modify in order to reduce the differences in frequencies. In the eigenvalue analysis, the ESE card is used in MSC-NASTRAN to calculate strain energies. Element strain energy can be defined as in Eq. 11 [31]. u_e is the element displacement and $[K_{ee}]$ is the stiffness of the element.

$$\mathbf{ESE}_e = \mathbf{0.5} \cdot \{\boldsymbol{u_e}\}^T[\boldsymbol{K_{ee}}]\{\boldsymbol{u_e}\} \qquad \text{Eq. 11 [31]}$$

Elements with high strain energy are an excellent candidate for modification to shift frequency effectively.

For the first frequency under consideration, which is calculated as 16.95Hz and measured as 17.49Hz, the structure's strain energy is concentrated around the launch vehicle adaptor. A strain energy contour plot at 16.95Hz is given in Figure 6.9.

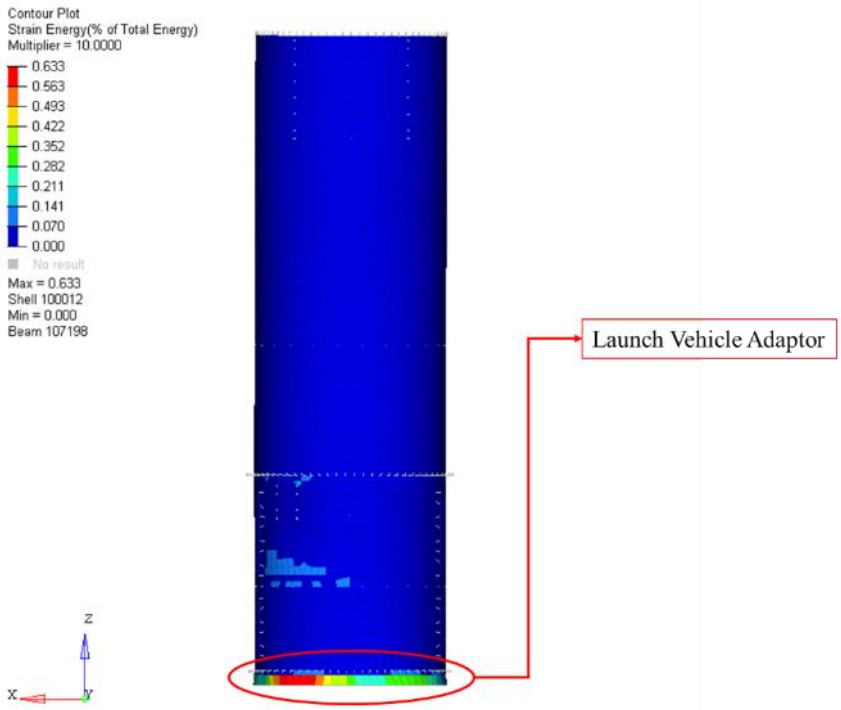

Figure 6.9. The Strain Energy Contour Plot at 16.95Hz

For the calculated natural frequencies of 48.26Hz and 54.97Hz, the strain energy densities are higher with respect to other elements at upper and lower tank interfaces. Also, the high strain energies are obtained at the lower part of the central cylinder. Tank interfaces and the lower part of the central cylinder are good candidates for modifications. The strain energy contour plots of 48.26Hz and 54.97Hz are demonstrated in Figure 6.10 and Figure 6.11, respectively.

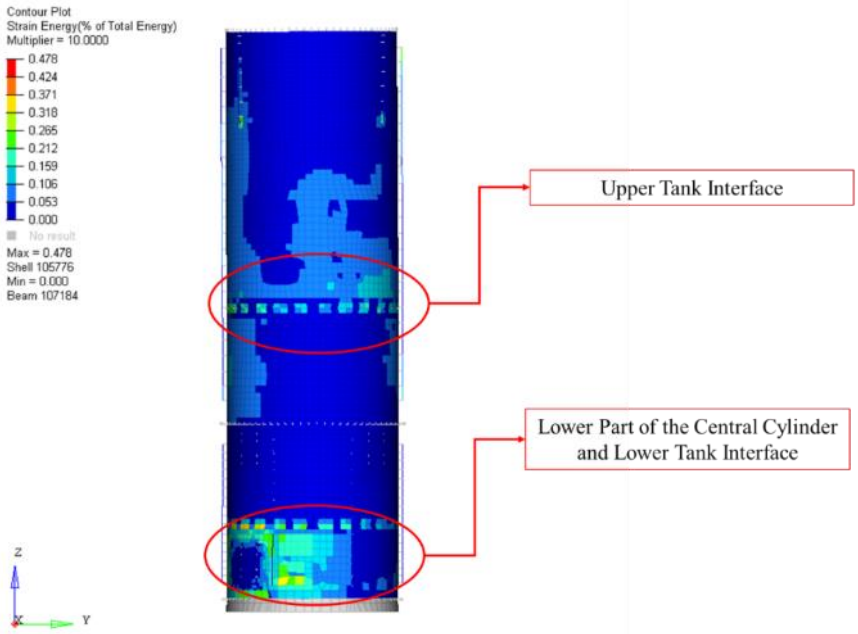

Figure 6.10. The Strain Energy Contour Plot at 48.26Hz

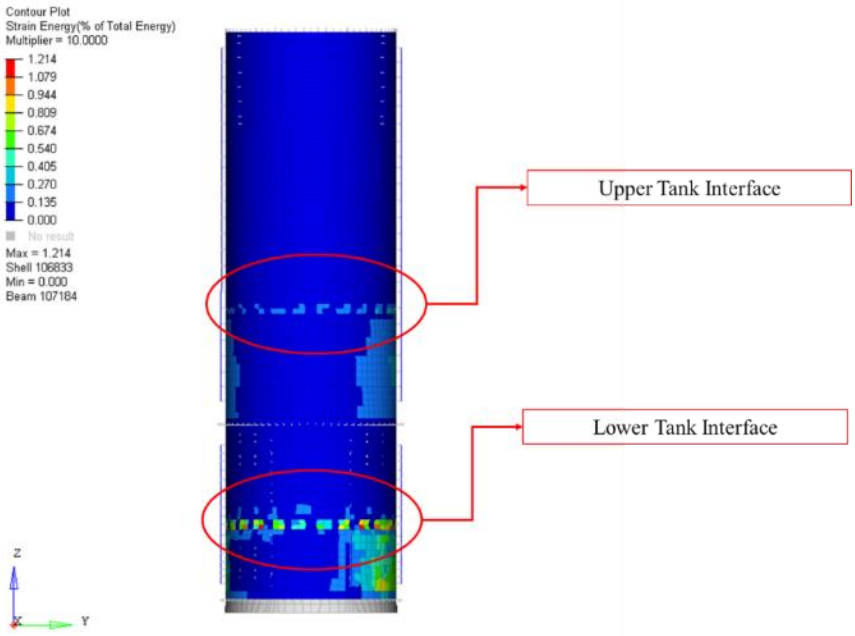

Figure 6.11. The Strain Energy Contour Plot at 54.97Hz

For the last interested natural frequency, which is calculated as 77.33Hz, the structure's strain energy is concentrated on the reflector rib and the interfaces of the

reflector with the satellite. A strain energy contour plot at 77.33Hz is given in Figure 6.12.

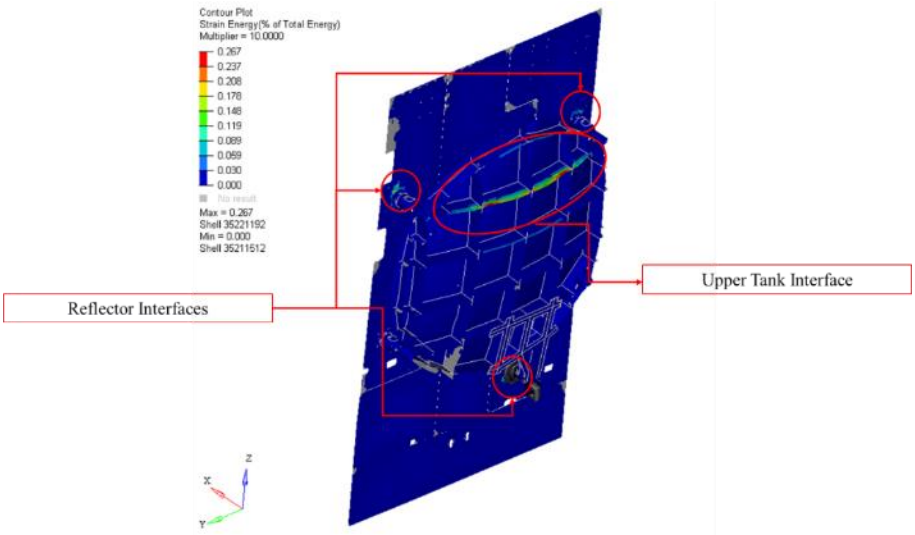

Figure 6.12. Strain Energy Contour Plot at 77.33Hz

6.5 Finite Element Model Iterations and Comparison

The aims of this section are to reduce the differences between the frequencies of the sine test results and the computational results and also to improve the MAC values. The object of the iterations is specified by using the European Space Standardization requirements.

According to European Space Standardization requirements (ECSS) [13], the difference in a satellite's fundamental bending frequency should be less than 3%. In this study, it was computed as 16.95 Hz and measured as 17.49 Hz, hence the deviation with respect to the experimental value is 3.19%. For the mode which has the highest effective mass, the requirement indicates a maximum deviation of 5%. In this study, it is the third mode, which has an effective mass higher than 10 %. Its frequency is computed as 54.97Hz and measured as 63.19Hz, thus showing a deviation of 14.95 % with respect to the experimental value. For the other mode the requirements indicate a deviation less than 10%, and in this thesis, the second mode

value is determined as 48.26Hz and 56.19 Hz, the fourth mode values, on the other hand, are computed as 77.33Hz and determined as 88.86Hz in the tests. Additionally, the MAC values should be higher than 0.9 for the fundamental bending mode and more than 0.85 for the modes with higher than 10% effective mass, which is the third mode of this thesis.

With the assumption that the sine vibration test results have been appropriately conducted and yielded accurate results, several parameter modifications are implemented on the FEM for sensitivity analysis after completing the error localization procedure. The sensitivity analysis's main aim is to evaluate each parameter's effect on the frequencies under consideration. In Eq. **12**, the effect of each parameter modification in stiffness matrices is shown. $\boldsymbol{K_j}$ is the stiffness matrices of the jth group of finite elements. Coefficient $\boldsymbol{\theta_j}$ is the updating parameters, and $\mathbf{K_0}$ is the initial stiffness matrices of the FEM [25].

$$\mathbf{K} = \mathbf{K_0} + \sum_{j=1}^{l} \boldsymbol{\theta_j K_j} \qquad \text{Eq. 12 [25]}$$

Goller et al. [35] modified several parameters in their study to update the FEM of the GOCE satellite. Elastic modulus, Poisson's ratio, shear modulus, densities of isotropic and orthotropic materials, and interface stiffness of the FEM are examples of parameters varied in their study. Goller et al. [35] limited the variation of the material properties by 10%, while for the stiffness of interface elements, the deviation went up to 100%. On the other hand, Doupe et al. [36] allowed a 25% deviation of material elasticity and stiffness in their study for the FEM update.

Firstly, the launch vehicle adaptor's different equivalent elasticity effect on the satellite's first bending mode is evaluated by applying 5% decrease and 5%, 10%, %15 increases in the value of the equivalent elasticity. In Figure 6.13, it is seen that increasing the equivalent elasticity of the launch vehicle adaptor causes an increase

in the bending frequency of the satellite. Since the frequencies resulting from the finite element analysis are lower than the sine vibration test results, the increase in stiffness values is considered for sensitivity analysis. The upper limits of the modification studies are taken as 10% for the elasticity properties and %100 percent for the stiffness values, as explained in Goller et al. [35].

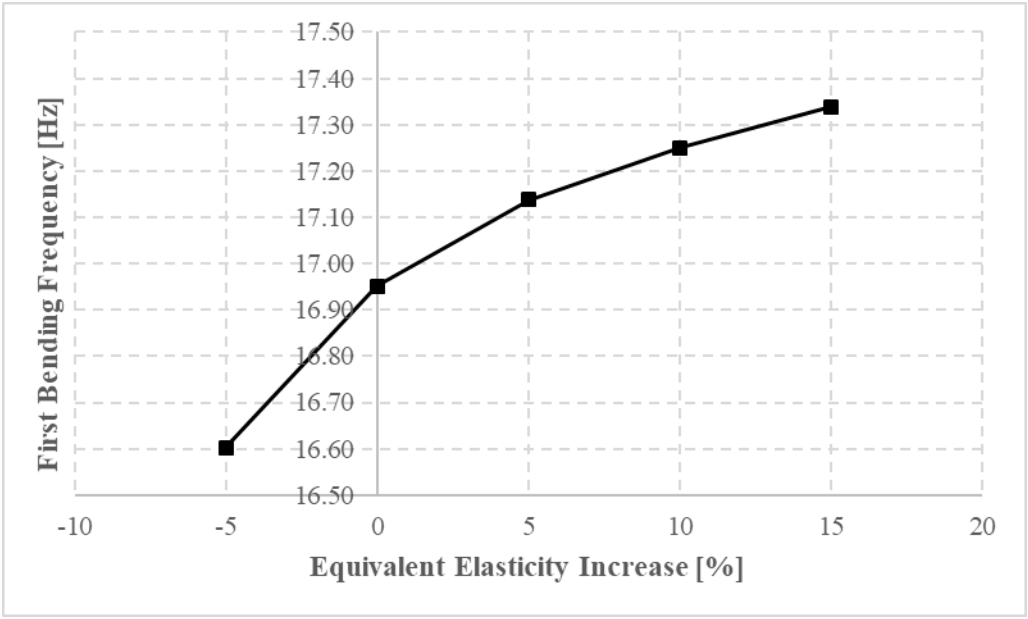

Figure 6.13. The Effect of the Launch Vehicle Adaptor Equivalent Elasticity on the X-direction Bending Mode of the Satellite

This study assumes that the dimensions and the masses of the satellite components are not changing. Therefore, design parameters that only change the stiffness values in the FEM are considered. The definition of parameters is mainly concentrated on the regions resulting from the error localization results. All parameters are increased by %10 for sensitivity analysis, which is defined as the upper limit of the material properties variation. In order to evaluate the effect of each parameter on the frequencies, the following iterations are performed;

1. Since there are simplification differences in the FEM of the launch vehicle adaptor, the equivalent elasticity of the adaptor increased by 10%.
2. The detail level of the launch vehicle adaptor FEM is increased.
3. The equivalent elasticity properties of CFRP skin at the central cylinder lower parts in x and y directions are increased by 10%.
4. The equivalent elasticity of CFRP skin at the central cylinder tank interface is increased by 10% in x and y directions.
5. Interfaces between tanks and the central cylinder are simplified as shell elements with CFRP sandwich panel properties. However, there are aluminum inserts instead of honeycomb in the sandwich panels. Aluminum elastic modulus properties are used at interfaces instead of honeycomb properties in order to increase the stiffness of tank interfaces.
6. The stiffness matrix of tanks is increased by %10.
7. The equivalent elasticity of CFRP skin of reflector interface with the satellite is increased %10 in x and y directions.
8. Fastener stiffness in the satellite FEM is increased by %10, which are modeled with CBUSH elements.
9. The density of virtual fluid decreased 10% in order to decrease the air effect.
10. Reflector rib elasticity in x and y directions are increased 10%

For each iteration, frequency response analysis is performed, and results are compared. Results and improvement percentages are given in Table 6.3.

Table 6.3. FEM Iterations and Frequency Results

Definition	Frequency #1		Frequency #2		Frequency #3		Frequency #4	
	[Hz]	[%]	[Hz]	[%]	[Hz]	[%]	[Hz]	[%]
Baseline	16.95	-	48.26	-	54.97	-	77.33	-
1-Central Cylinder Launch Vehicle Adaptor Elasticity Increase	17.25	1.76%	48.54	0.58%	55.17	0.36%	77.51	0.23%
2-Increased Detail Level of Launch Vehicle Adaptor	17.32	2.17%	48.58	0.65%	55.20	0.42%	77.56	0.29%
3-Central Cylinder Lower Part Elasticity Increase	17.24	1.70%	48.46	0.42%	55.21	0.44%	77.36	0.04%
4-Central Cylinder Tank Interface Elasticity Increase	16.99	0.20%	48.39	0.27%	55.04	0.13%	77.33	0.00%
5-Central Cylinder Tank Interface Out-of-plane Stiffness Increase	16.99	0.20%	48.71	0.94%	57.40	4.41%	77.60	0.35%
6-Increase Tanks Stiffness	16.96	0.07%	48.79	1.11%	55.72	1.36%	77.35	0.02%
7-Reflector Interface Elasticity Increase	16.99	0.20%	48.42	0.32%	54.98	0.02%	77.58	0.32%
8-Increase Fastener Stiffness	16.95	0.00%	48.33	0.15%	54.99	0.04%	77.33	0.00%
9-Air Effect Decrease	16.99	0.20%	48.32	0.13%	54.99	0.04%	81.03	4.78%
10-Reflector Rib Stiffness increase	16.95	0.00%	48.27	0.01%	54.98	0.02%	77.42	0.11%

Most effective iterations for 16.95Hz are related to modification on the bottom part of the central cylinder, which is in line with the error localization. Increasing the equivalent stiffness of the launch vehicle adaptor (iteration #1) affects the x-direction bending frequency of the satellite by 1.76%. Increasing the detail level of the model (iteration #2) increases that frequency by 2.17%. A detailed comparison of iteration #1 and #2 is shown in Figure 6.14.

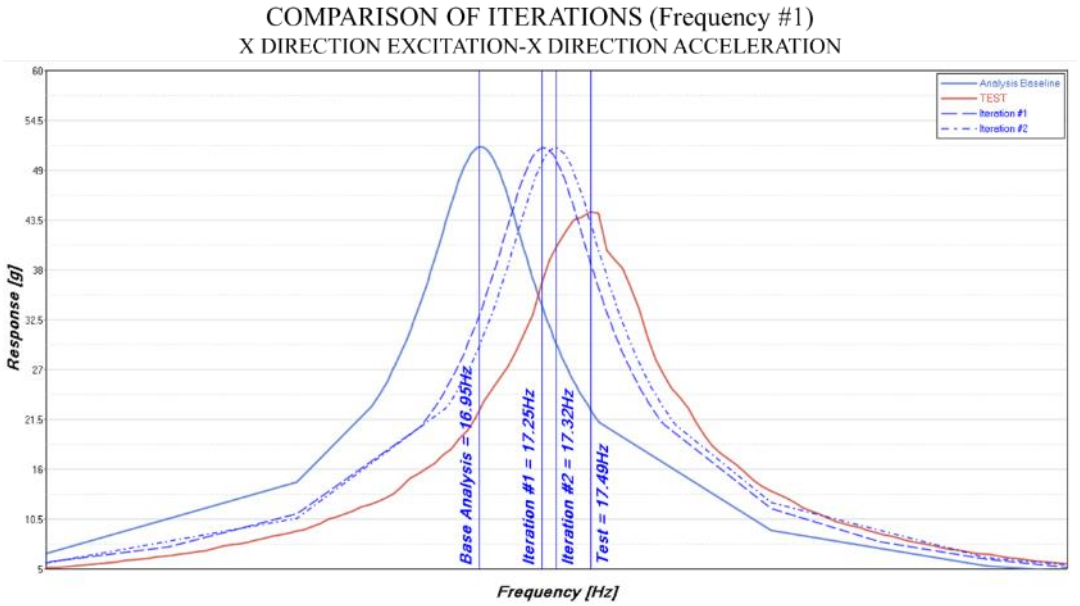

Figure 6.14. The Detailed Comparison of Iteration #1 and #2 for Frequency #1

The frequencies related to tank mode shapes,56.19Hz and 63.19Hz, in the test are mostly influenced by modification around tank interfaces and the tank's stiffness. Central cylinder out of plane stiffness (iteration #5) and tank stiffness modification (iteration #6) significantly increase second interested frequency 0.94% and 1.11%. For the third interested frequency, improvements are 4.41% and 1.36%. A detailed comparison of iteration #3, #5, and #6 is shown in Figure 6.15.

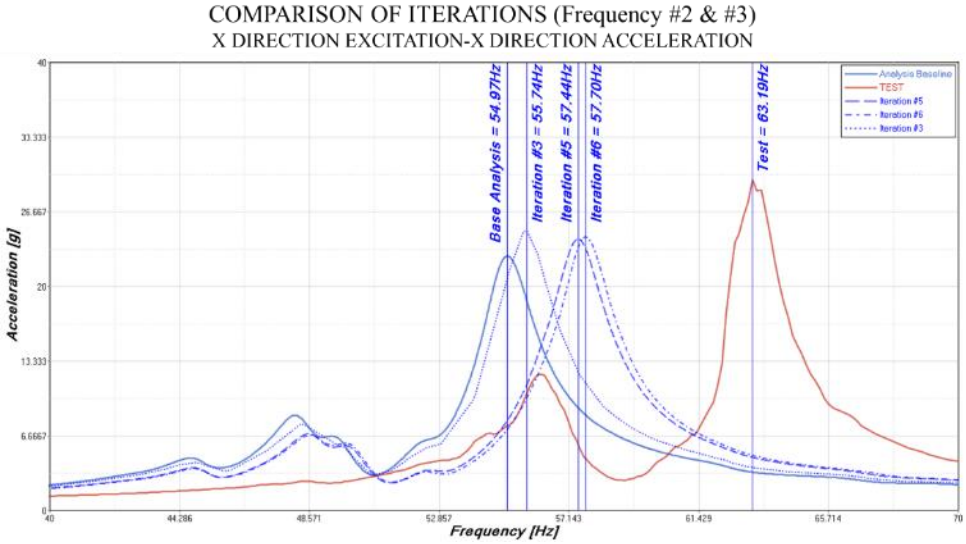

Figure 6.15. The Detailed Comparison of Iteration #3, #5 and #6 for Frequency #2 and #3

For reflector bending mode, which is 88.86Hz in the test, stiffness increases at the reflector interface (iteration #7) shift frequency by 0.32%. The most effective modification for reflector mode is the decrease of the air effect (iteration #9). The decreasing density of the fluid 10% is shifting the frequency by 4.78%. A detailed comparison of iteration #7 and #9 is shown in Figure 6.17.

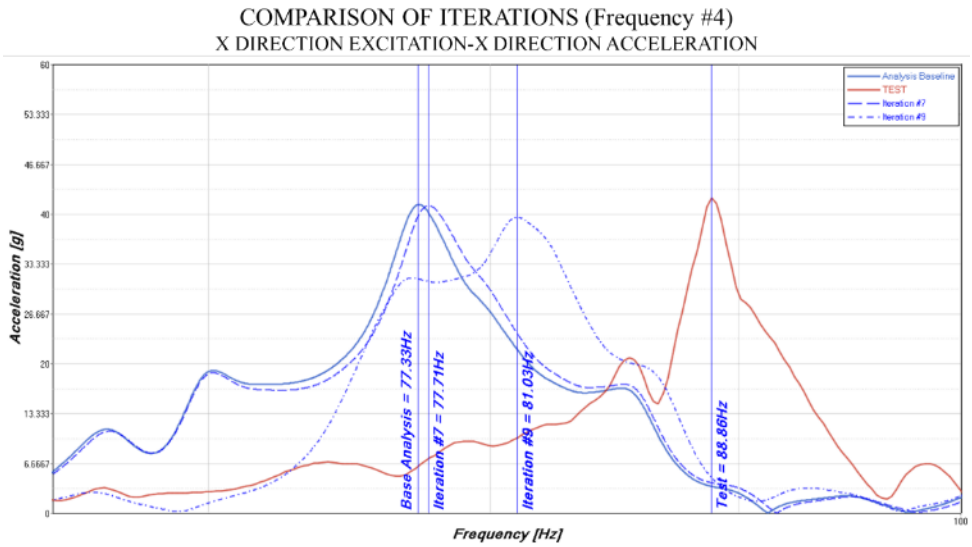

Figure 6.16. The Detailed Comparison of Iteration #7 and #9 for Frequency #4

In addition, MAC matrices for each iteration are calculated. As a result, it is observed that there are no significant improvements for the first and fourth frequencies. The main reason is that these frequencies already have good similarity and have MAC values of higher than 0.9. For the second frequency, tank stiffness increase and the central cylinder interface stiffness increase improve the MAC values significantly which is 5.7% and 4.43%. In Table 6.4, diagonal values of MAC matrices are given for comparison.

Table 6.4. FEM Iterations and MAC Results

Definition	**MAC (1,1)**		**MAC (2,2)**		**MAC (3,3)**		**MAC (4,4)**	
Baseline	0.960	-	0.790	-	0.901	-	0.920	-
1-Central Cylinder Launch Vehicle Adaptor Elasticity Increase	0.960	0.00%	0.820	3.80%	0.916	1.66%	0.924	0.43%
2-Increased Detail Level of Launch Vehicle Adaptor	0.960	0.00%	0.825	4.43%	0.918	1.89%	0.925	0.54%
3-Central Cylinder Lower Part Elasticity Increase	0.960	0.00%	0.815	3.16%	0.913	1.33%	0.921	0.11%
4-Central Cylinder Tank Interface Elasticity Increase	0.960	0.00%	0.795	0.63%	0.901	0.00%	0.920	0.00%
5-Central Cylinder Tank Interface Out-of-plane Stiffness Increase	0.960	0.00%	0.835	5.70%	0.901	0.00%	0.920	0.00%
6-Increase Tanks Stiffness	0.961	0.10%	0.825	4.43%	0.905	0.44%	0.921	0.11%
7-Reflector Interface Elasticity Increase	0.960	0.00%	0.793	0.38%	0.904	0.33%	0.926	0.65%
8-Increase Fastener Stiffness	0.960	0.00%	0.791	0.13%	0.901	0.00%	0.920	0.00%
9-Air Effect Decrease	0.960	0.00%	0.792	0.25%	0.921	2.22%	0.920	0.00%
10-Reflector Rib Stiffness increase	0.960	0.00%	0.795	0.63%	0.901	0.00%	0.920	0.00%

The sensitivity analysis shows that parameters related to the launch vehicle adaptor, which is iteration #1 and iteration #2, increase first bending frequency by 1.76% and 2.17%, while in other frequencies, these improvements are fairly limited. A similar situation is observed in other parameters as well. For instance, tank stiffness increases by 10% improve second and third frequencies by 1.11% and 1.36%. On the other hand, the effect on the first and fourth frequencies are 0.07% and 0.02%, respectively. For the reflector bending mode, which is calculated as 77.33Hz and measured as 88.86, decreasing air effect by 10% increases frequency by 4.78%, and the maximum increase in other frequencies is 0.20%. Increasing all parameters at the

same time causes an over-estimate in the x-direction bending frequency of the satellite by 1.25 %, which is shown in Table 6.5.

Table 6.5. Frequency Comparison of Results

Mode Description	**Baseline [Hz]**	**Percentage wrt Test [%]**	**All Iteration [Hz]**	**Percentage wrt Test [%]**	**Test [Hz]**
X Direction First Bending of the Satellite	16.95	-3.19%	17.71	1.25%	17.49
Asymmetric Bending Mode of the Tanks	48.26	-16.43%	50.68	-10.87%	56.19
X Direction Bending Mode of the Tanks	54.97	-14.90%	59.53	-6.15%	63.19
Bending Mode of the Reflector	77.33	-14.91%	81.15	-9.50%	88.86

As a result, to achieve the best improvements in four frequencies, iteration #1 and iteration #2 are eliminated, mainly affecting the satellite's first bending frequency. Iterations that are mainly increasing remaining frequencies are considered. Tanks stiffness increase is limited up to 30% since this modification is also affecting the first bending mode of the satellite. For the fourth frequency, which is the reflector's bending mode, the main contributor is the air effect, and it is decreased by 40%. Following modifications are implemented as a final iteration on the FEM to increase similarity:

1. The equivalent elasticity properties of CFRP skin at the central cylinder lower parts in x and y directions are increased by 10%. (Iteration #3)
2. The equivalent elasticity of CFRP skin at the central cylinder tank interface is increased by 10% in x and y directions. (Iteration #4)
3. Aluminum elastic modulus properties are used at interfaces instead of honeycomb properties in order to increase the stiffness of tank interfaces. (Iteration #5)
4. The stiffness matrix of tanks is increased by %30. (Iteration #6)

5. The equivalent elasticity of CFRP skin of reflector interface with the satellite in increased %10 in x and y directions. (Iteration #7)
6. The density of virtual fluid decreased by 40% in order to decrease the air effect. (Iteration #9)

The FEM is improved with six modifications, and frequency response analysis is performed again. For the final iteration, the comparison of the test and analysis is shown in Figure 6.17, Figure 6.18, and Figure 6.19

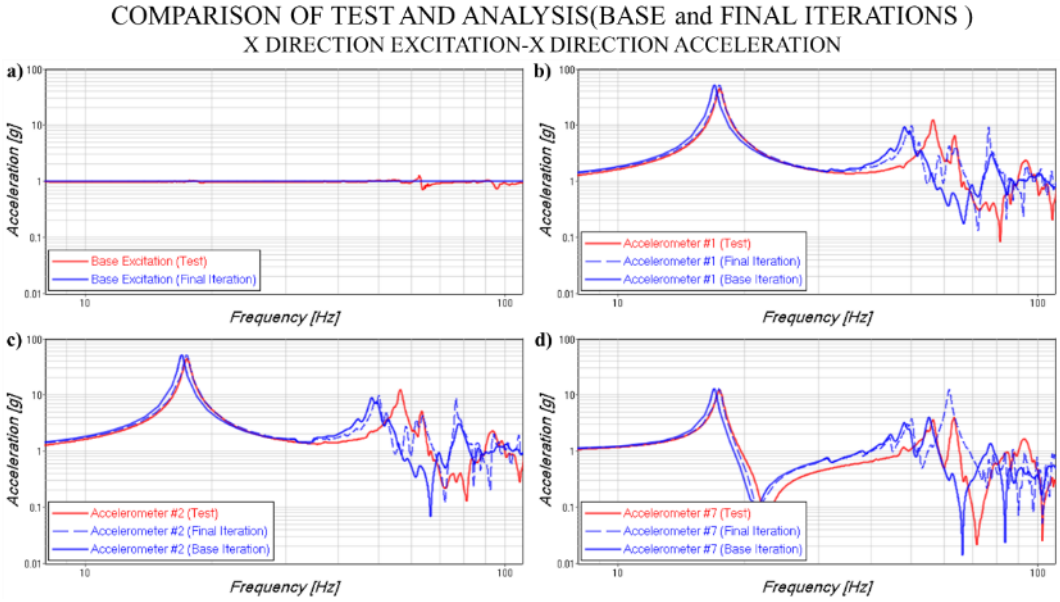

Figure 6.17. Test and Analysis (Base and Final Iterations) Transfer Function Comparison of (a) Base Excitation, Accelerometer (b) #1, (c) #2 and (d) #7

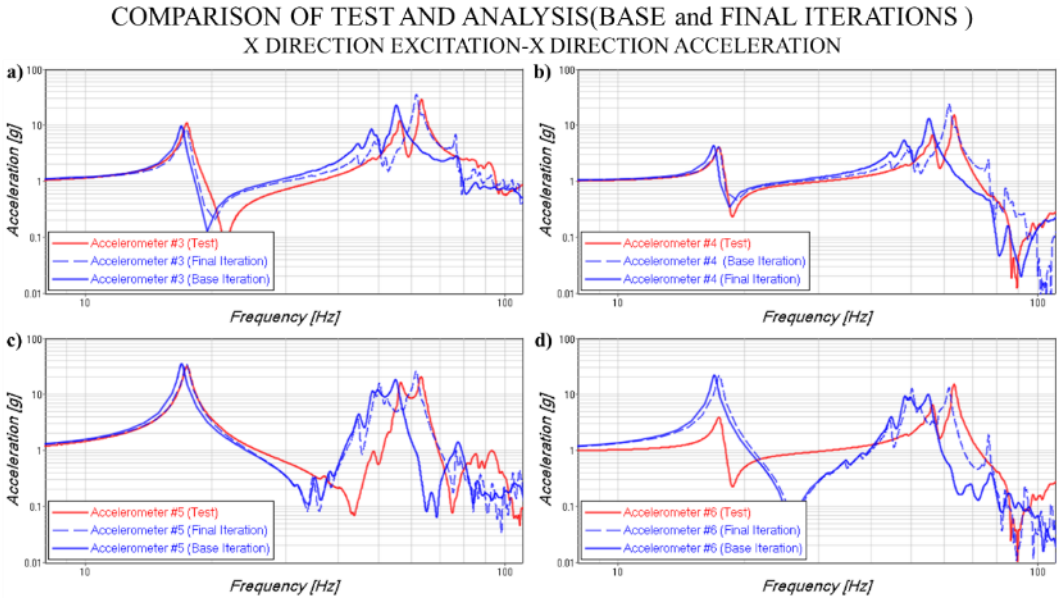

Figure 6.18. Test and Analysis (Base and Final Iterations) Transfer Function Comparison of Accelerometer (a) #3, (b) #4, (c) #5 and (d) #6

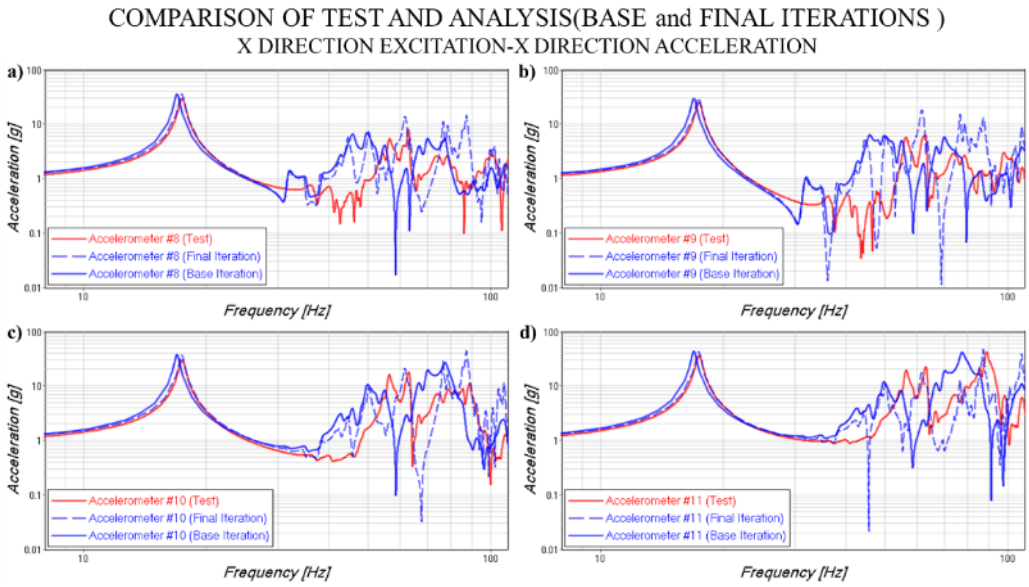

Figure 6.19. Test and Analysis (Base and Final Iterations) Transfer Function Comparison of Accelerometer (a) #8, (b) #9, (c) #10 and (d) #11

A detailed comparison of the x-direction mode of the satellite is shown in Figure 6.20.

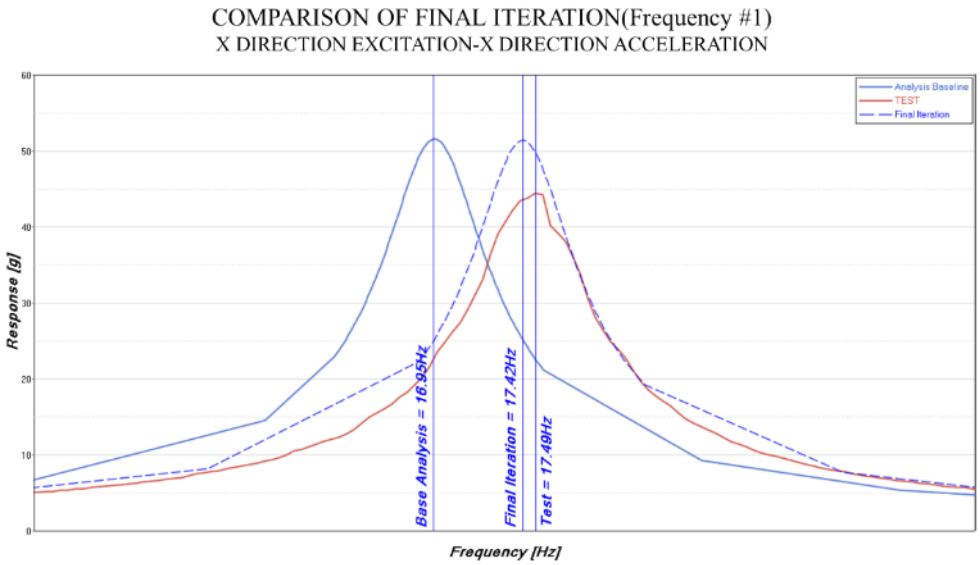

Figure 6.20. Detailed Comparison of Test, Base, and Final Iterations for Frequency #1

Detailed comparison of the asymmetric bending and the x-direction bending mode of the tanks are demonstrated in Figure 6.21.

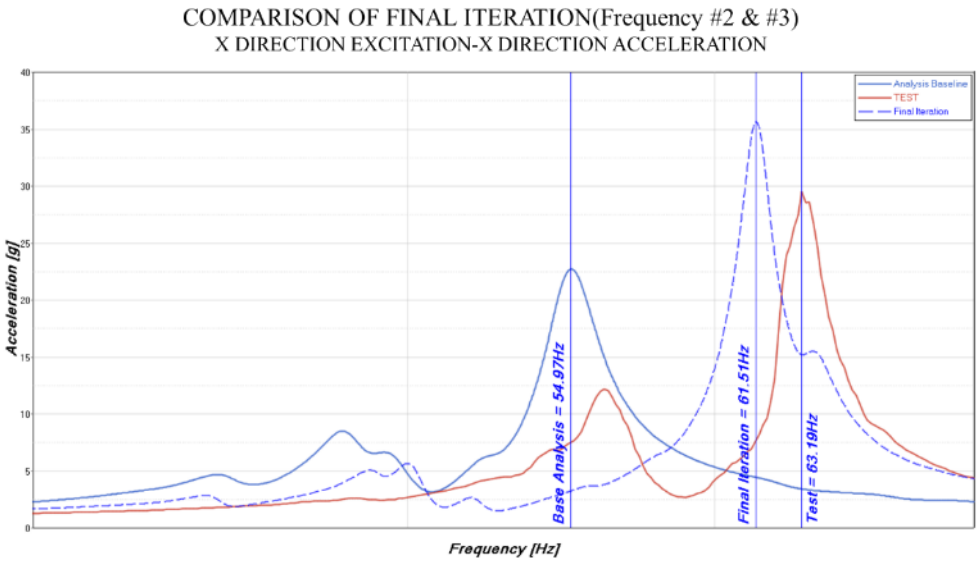

Figure 6.21. Detailed Comparison of Test, Base, and Final Iterations for Frequency #2 and #3

A detailed comparison of the bending mode of the reflector is shown in Figure 6.22.

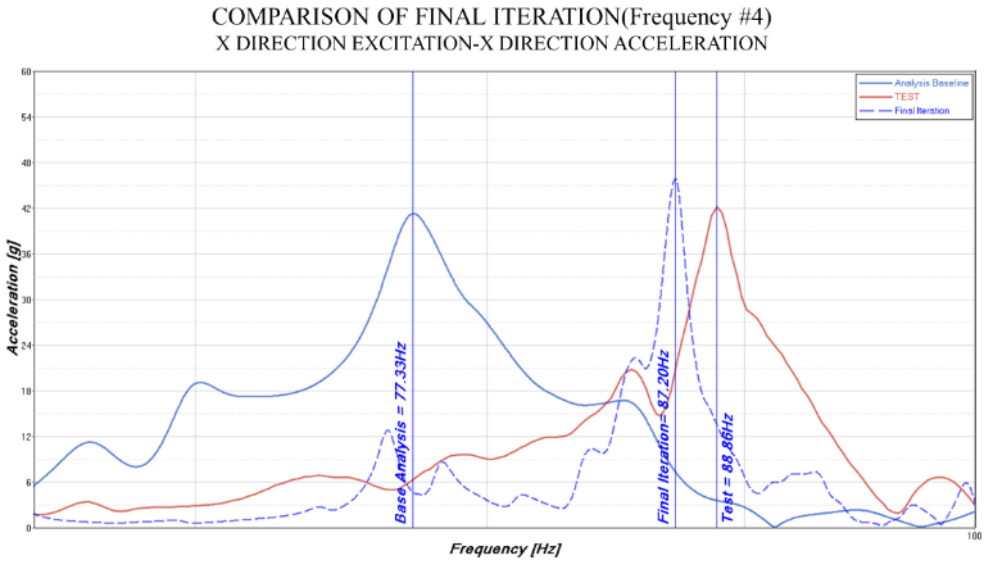

Figure 6.22. Detailed Comparison of Test, Base, and Final Iterations for Frequency #4

In addition to frequency response analysis of the final iteration, MAC calculation is also performed. The result of MAC matrices is shown in Table 6.6 and Figure 6.23.

Table 6.6. The Modal Assurance Criteria Between Test and Final Analysis Iteration Results

Frequency [Hz]		**Test**			
		17.49	56.19	63.19	88.86
Analysis	17.42	0.961	0.295	0.009	0.014
	50.15	0.197	0.880	0.002	0.177
	61.51	0.065	0.045	0.915	0.120
	87.20	0.148	0.253	0.005	0.928

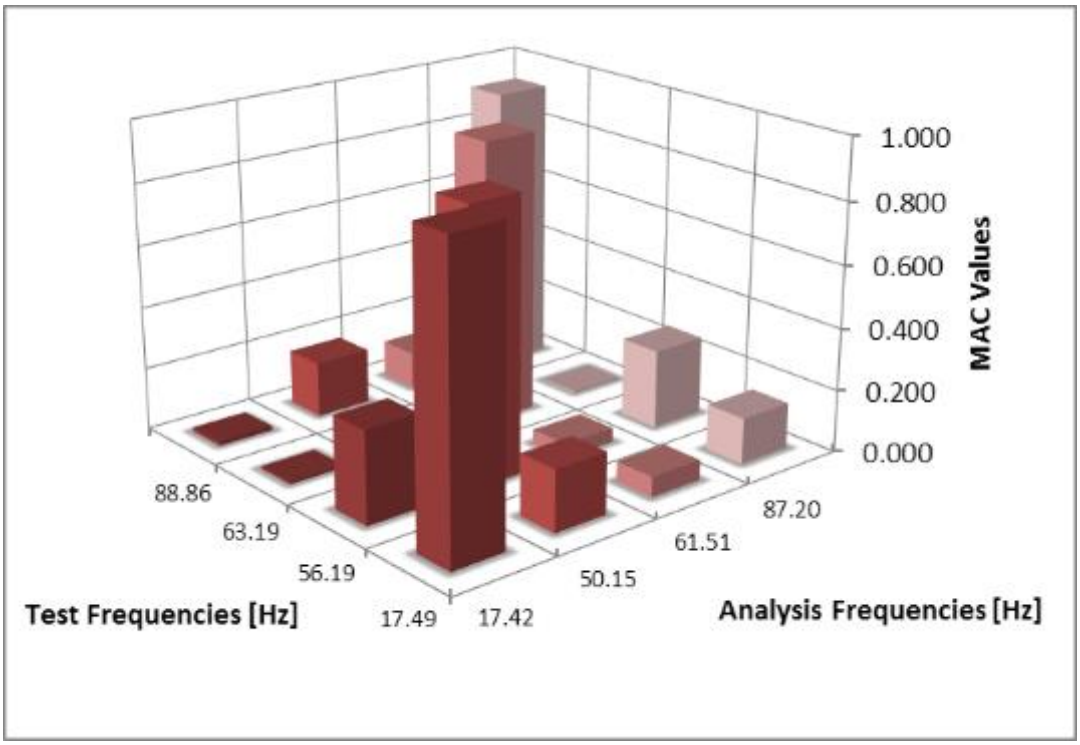

Figure 6.23. The Modal Assurance Criteria Between Test and Final Analysis Iteration Results

With the final iteration, the x-direction bending mode of the satellite is increased from 16.95Hz to 17.42Hz, and the difference with respect to test results is improved by 3.19% to 0.40%. For the second frequency, the frequency shifts from 48.26Hz to 50.15Hz, and results improved from 16.43% to 12.04%. One of the most significant improvements is observed at the tanks' bending mode, which is increased from 54.97Hz to 61.51Hz. The difference between the analysis and test result diminish from 14.9% to 2.73%. The last frequency, which is the reflector's bending mode, is the most improved frequency. The frequency increase from 77.33Hz to 87.20Hz, and the difference drops from 14.91% to 1.90%. The comparison of frequencies and improvements is given in Table 6.7.

Table 6.7. Frequency Comparison of Improved Results

Mode Description	Baseline [Hz]	Percentage wrt Test [%]	Final Iteration [Hz]	Percentage wrt Test [%]	Test [Hz]
X-direction First Bending of the Satellite	16.95	-3.19%	17.42	-0.40%	17.49
Asymmetric Bending of the Tanks	48.26	-16.43%	50.15	-12.04%	56.19
X-direction Bending of the Tanks	54.97	-14.90%	61.51	-2.73%	63.19
Bending Mode of the Reflector	77.33	-14.91%	87.20	-1.90%	88.86

Since the first, second, and third interested frequencies of the analysis have MAC values close to 1, improvements on the FEM affect them less. For the first frequency, improvement is 0.1%, while at the third and fourth frequency, MAC improvements are 1.55% and 0.87% with respect to the base iteration, respectively. However, for the second frequency, which is the asymmetric bending mode of the frequency, 11.39% of significant improvement is observed. The comparison of diagonal values of the MAC is given in Table 6.8.

Table 6.8. Comparison of Improved Results of MAC Values

Mode Description	Baseline	Final Iteration	Improvement [%]
X-direction First Bending of the Satellite	0.960	0.961	0.10%
Asymmetric Bending Mode of the Tanks	0.790	0.880	11.39%
X-direction Bending of the Tanks	0.901	0.915	1.55%
Bending Mode of the Reflector	0.920	0.928	0.87%

6.6 Conclusion

In this chapter, transfer functions obtained by the x-direction sine vibration test and frequency response analysis are compared for each accelerometer location. With assurance criteria checks, mode pairings and similarities are evaluated, including eleven accelerometers for four frequencies that have the highest effective mass in the x-direction.

With the help of error localization, regions sensitive to modifications are determined, and ten iterations are performed to identify effects on frequencies and MAC matrices. The combination of iterations that give the best improvements is considered as a final iteration.

Finally, the error percentage of the x-direction first bending frequency of the satellite is decreased from 3.19% to 0.4%. The asymmetric bending mode of tanks is decreased from 16.43% to 12.04%. The x-direction bending mode of the tanks decreases from 14.90% to 2.73%. Lastly, the bending frequency of the reflector improved to 1.9% from 14.91%. In addition, the MAC values of the frequencies are improved at the final iteration. The most improved value belongs to the second frequency, which is measured as 56.19Hz in the sine vibration test, increases from 0.79 to 0.88 with an 11.39% improvement.

Significant improvements are obtained with respect to the test results in both frequencies and MAC matrices.

CHAPTER 7

CONCLUSION

7.1 General Conclusions

In this thesis, a communication satellite's finite element model has been indigenously developed, verified and the numerically obtained frequency response results have been compared with the sine vibration test. The thesis was completed by following a procedure for updating the developed Finite Element Model.

First, the FEM of the communication satellite, the mechanical properties of the FEM, and the validation checks were presented. The FEM was generated in HYPERMESH commercial software. The eigenvalue analysis and frequency response analysis were performed in MSC-NASTRAN commercial software.

Uni-directional sine vibration tests were also conducted, and the relevant frequency responses were presented.

The calculation of the modal effective mass was a useful tool for defining the prominent modes and estimating the structure's response. The critical frequencies were chosen by using effective mass. The highest effective mass in the x-direction was 45.1% at the satellite's fundamental bending mode, which was calculated as 16.95Hz, and all the accelerometers responded with very high values at this frequency. The other two modes with the most effective masses of 6.5% and 10.1% respectively in the x-direction were tanks' modes. They were calculated as 48.26Hz and 54.97Hz, and accelerometers on the tanks had the highest responses. The last frequency, which also had a reasonably high effective mass, that was 3.2% effective mass in the x-direction and was calculated as 77.33Hz, belonged to reflectors' bending mode. Especially the accelerometers on the reflector resulted in a high response in that frequency.

Another critical process was mode pairing and similarity analysis, which was performed via the modal assurance criteria. The previously analyzed four frequencies, which were selected by using the effective mass calculations in the x-direction, were also used for the mode pairing studies. Diagonal MAC values of first (calculated as16.95Hz and measured as 17.49Hz), third (calculated as 54.97Hz and measured as 63.19Hz), and fourth (calculated as77.33Hz and measured as 88.86Hz) frequencies resulted to be higher than 0.9, which showed good similarity. For the second frequency calculated as 48.26Hz and measured as 56.19Hz, the MAC value was 0.79 with a reasonable similarity.

The possible regions of the errors in the FEM were determined by using the error localization calculations in which their numerical and experimental response values differ. The sensitive regions for possible modifications were identified, and the sensitivity analyses were performed by changing one parameter at each time in the FEM re-calculations. The improvements in the results were observed. In the iterations, the trial and error approach was considered in order to improve the FEM of the satellite. The object was to minimize the frequency difference between the sine vibration test results and the computational analysis results by using the correlation requirements specified in the European Space Standardization mechanical handbook.

In the sensitivity analysis, it was assumed that parameters affecting the stiffness values of elements might contain some variation from theoretically assigned values, but the dimensions and masses of the components were not varied. Ten sensitivity analyses were performed by modifying the values of equivalent elasticity, stiffness, and air effects of the components in the FEM. The frequency and the MAC matrices improvements were also observed. It was seen that every iteration increased frequency in different amounts. For instance, tank stiffness increases by 10% improved second and third frequencies by 1.11% and 1.36%; on the other hand, the effect on first and fourth frequencies were 0.07% and 0.02%, respectively. By choosing the most effective combination of the modifications which yielded significant improvements in the four frequencies under consideration, the numerical

frequency response analysis was repeated, and the final comparison with test and numerical data were presented.

In this study, only the resonance frequencies values and MAC values were considered. The response amplitude determinations and the improvements were not attempted.

In conclusion, the numerically obtained frequencies approached the experimental ones significantly. The most improved frequency was the reflector's bending mode, whose frequency was improved from 77.33Hz to 87.20Hz, and the difference with respect to the sine test result improved from 14.91% to 1.90%. For the other frequencies, substantial improvements were also obtained, and the detailed results were given in the thesis. In addition to frequency improvements, significant improvement of the second frequency MAC value was also achieved. The analysis and sine test results' similarity increased from 0.79 to 0.88 at the second frequency. By using the methodologies specified in the thesis, the FEM modal improvement was completed with the increasing similarity between the x-direction sine test and the numerical analysis results.

7.2 Recommendations for the Future Work

By considering the results of this study, the following studies can be recommended as future studies:

- In this study, only the x-direction sine vibration test is studied. The y and z-direction experimental results can also be investigated. The relevant expansions and enhancements in the Finite Element Model also can be implemented.
- Eleven 3-axis accelerometers are used in the x-direction sine test. The utilization of a larger number can provide more accurate and reliable results.

- The effect of various other parameters on the frequencies can be investigated in sensitive analysis such as Poisson's ratio, shear modulus, density, the equivalent thickness.
- The damping improvement can be included in the numerical model in order to get more realistic response levels with the actual responses.
- In addition to modal assurance criteria, various other criteria such as the base force assurance criteria and effective mass similarity can also be investigated.
- Formal multi-object optimization methods can be used in the FEM to improve resonance frequency and MAC values.
- Some stochastic methods such as Bayesian update can be studied. With increasing CPU power, detailed sensitivity analysis can be performed by using Monte Carlo algorithms.

REFERENCES

[1] NASA,“Sputnik1.”, https://nssdc.gsfc.nasa.gov/nmc/spacecraft/display.action?id=1957-001B (accessed Dec. 01, 2020).

[2] G. Di Mauro, M. Lawn, and R. Bevilacqua, “Survey on guidance navigation and control requirements for spacecraft formation-flying missions,” *J. Guid. Control. Dyn.*, vol. 41, no. 3, pp. 581–602, 2018.

[3] NASA, “Laser Communications Relay Demonstration (LCRD) Overview.” https://www.nasa.gov/mission_pages/tdm/lcrd/overview.html (accessed Dec. 01, 2020).

[4] ESA,“Rosetta ESA’s comet-chaser.”,https://www.esa.int/Science_Exploration/Space_Science/Rosetta (accessed Dec. 01, 2020).

[5] NASA, “NASA Earth Science.” https://science.nasa.gov/earth-science (accessed Dec. 01, 2020).

[6] ESA, “Sentinel-4 and -5.” http://www.esa.int/Applications/Observing_the_Earth/Copernicus/Sentinel-4_and_-5 (accessed Dec. 01, 2020).

[7] NASA, “Catalog of Earth Satellite Orbits.” https://earthobservatory.nasa.gov/features/OrbitsCatalog .

[8] TUSAS, “GÖKTÜRK-1.” https://www.tusas.com/en/product/gokturk-1 , (accessed Dec. 01, 2020).

[9] ESA Earth Observation Portal, “Galileo navigation program: FOC (Full Operational Capability).” https://directory.eoportal.org/web/eoportal/satellite-missions/g/galileo-foc#launch (accessed Dec. 01, 2020).

[10] TUSAS, “TÜRKSAT 6A.” https://www.tusas.com/urun/turksat-6a, (accessed Dec. 01, 2020).

[11] T. Yasaka and J. Onoda, “Spacecraft Structures,” *Encycl. Phys. Sci. Technol.*, pp. 449–461, 2003

[12] ArianeSpace, “Soyuz User’s Manual,” no. Issue 2 Revision 0, 2012, [Online]. Available:http://www.arianespace.com/wp-content/uploads/2015/09/Soyuz-Users-Manual-March-2012.pdf .

[13] ECSS Secretariat, Space engineering - Spacecraft mechanical loads analysis handbook, no. February. 2013.

[14] Arianespace, “Ariane 6 Users Manual,” no. 1, p. 152, 2016.

[15] NASA, “Syncom 3.” https://nssdc.gsfc.nasa.gov/nmc/spacecraft/display.action?id=1964-047A (accessed Dec. 01, 2020).

[16] T. P. Sarafin, Spacecraft Structure and Mechanism. 1995.

[17] ESA, “SmallGEO (Small Geostationary Satellite Platform) Initiative / HAG1 Mission.” https://earth.esa.int/web/eoportal/satellite-missions/s/smallgeo (accessed Dec. 01, 2020).

[18] J. M. Houghton, Spacecraft Structures. 2011.

[19] J. H. Lim, “A correlation study of satellite finite element model for coupled load analysis using transmissibility with modified correlation measures,” *Aerosp. Sci. Technol.*, vol. 33, no. 1, pp. 82–91, 2014.

[20] G. Wang, “Dynamic Parameter Sensitivities”, *AIAA Journal* , vol. 32, no. 11, 1994.

[21] R. J., “The modal assurance criterion - Twenty years of use and abuse,” *Sound Vib.*, vol. 37, no. 8, pp. 14–21, 2003.

[22] K. K. Sairajan and G. S. Aglietti, “Study of Correlation Criteria for Base Excitation of Spacecraft Structures*,” J. Spacecr. Rockets,* vol. 51, no. 1, pp. 106–116, 2013.

[23] Michael Link and Oscar Floressantiago, “Updating and localizing structural errors based on minimization of equation errors,” *ESA*, vol. 2, no. September, 1991.

[24] Calvi and M. Klein, “Uncertainty-based loads analysis for spacecraft: Finite element model validation and dynamic responses,” *Comput. Fluid Solid Mech.* 2003, vol. 83, pp. 2226–2228, 2003.

[25] J. E. Mottershead, M. I. Friswell, and J. E. Mottershead, Finite Element Model Updating in Structural Dynamics, vol. 38. 1995.

[26] G. S. Aglietti, S. J. I. Walker, and A. Kiley, "On the use of SEREP for satellite FEM validation*," Eng. Comput. (Swansea, Wales)*, vol. 29, no. 6, pp. 580–595, 2012.

[27] B. Goller, M. Broggi, A. Calvi, and G. I. Schuëller, "A stochastic model updating technique for complex aerospace structures", *Finite Elem. Anal. Des.*, vol. 47, no. 7, pp. 739–752, 2011.

[28] A. Technologies, "APCO Technologies Products." https://www.apco-technologies.eu/apco-content/uploads/2018/04/Catalogue-PdV-LR.pdf ,(accessed Dec. 24, 2020).

[29] PLASCORE,"Honeycomb Data Sheet." https://www.plascore.com/download/datasheets/honeycomb_data_sheets/PLA_PAMG-XR1-5056_10-02-20.pdf (accessed Dec. 29, 2020).

[30] TORAYCMA, "M55J Technical Data Sheet." https://www.toraycma.com/page.php?id=661 (accessed Dec. 29, 2020).

[31] MSC NASTRAN, User's Guide. 2018.

[32] NASA, "FINITE ELEMENT MODEL VALIDITY CHECK." https://femci.gsfc.nasa.gov/validitychecks/vc2.html (accessed Dec. 29, 2020).

[33] PCB, "Guidelines for Mounting Test Accelerometers.".

[34] N. Roy and A. Girard, "Impact of residual modes in structural dynamics," vol. 581, p. 52, Jan. 2005.

[35] B. Goller, M. Broggi, A. Calvi, and G. I. Schuëller, "Efficient Model Updating of the GOCE Satellite Based on Experimental Modal Data," *Comput. Methods Appl. Sci.*, vol. 26, no. May, pp. 215–235, 2013.

[36] C. C. Doupe, E. D. Swenson, and L. E. George, "Finite Element Model Tuning with 3D Mode Shapes," no. May, 2009.